Nationaal Lucht- en Ruimtevaartlaboratorium

National Aerospace Laboratory NLR

NLR-TP-2002-224

Archaeological silver embrittlement: a metallurgical inquiry

R.J.H. Wanhill

Nationaal Lucht- en Ruimtevaartlaboratorium

National Aerospace Laboratory NLR

NLR-TP-2002-224

Archaeological silver embrittlement: a metallurgical inquiry

R.J.H. Wanhill

This report is intended to be a state-of-the-art contribution to the archaeo-metallurgical literature on silver embrittlement.

Contents

4 Tables
26 Figures   } Main text

4 Tables
22 Figures   } Appendices

(105 pages in total)

This page is intentionally left blank.

ARCHAEOLOGICAL SILVER EMBRITTLEMENT:
A METALLURGICAL INQUIRY

R.J.H. Wanhill

National Aerospace Laboratory NLR, Anthony Fokkerweg 2,
1059 CM Amsterdam, The Netherlands

ABSTRACT

Some archaeological silver artifacts and coins are found to be brittle. The brittleness is due to long-term corrosion and microstructural changes. Recognition and determination of corrosion-induced and microstructurally-induced embrittlement, and also their synergy, are important for restoration and conservation of ancient and historic silver. This report is concerned mainly with defining and explaining the types, probable mechanisms and severity of embrittlement, based on current metallurgical knowledge and concepts. It also includes surveys of the diagnostic techniques for determining embrittlement and the possible remedial measures to be taken.

Corrosion may be general, forming a brittle surface layer. But it can also penetrate the metal along grain boundaries, segregation bands, interdendritic regions (in cast objects), and slip lines and deformation twin boundaries in objects containing remanent cold-work. The probable and possible mechanisms of corrosion-induced embrittlement include galvanic attack owing to long-term low temperature segregation of copper to grain boundaries (discontinuous or cellular precipitation), galvanic attack owing to the presence of the remains of high temperature segregation of copper, and preferential stress- and strain-assisted corrosion along slip lines and deformation twin boundaries.

Microstructurally-induced embrittlement is characterized by grain boundary fracture, which is most likely due to impurity elements segregating to grain boundaries and reducing their cohesive strength. Empirical evidence, empirical and theoretical concepts of segregation-induced embrittlement, and consideration of the impurity elements in archaeological silver result in identifying lead as the most likely perpetrator, with bismuth, arsenic, thallium, antimony and tin as increasingly less likely additional candidates.

The severity of both kinds of embrittlement is increased by the synergistic action of corrosion-induced and microstructurally-induced embrittlement and a larger grain size. The effect of grain size is explained and semi-quantitatively assessed using micromechanical models of corrosion-induced, microstructurally-induced and synergistic embrittlement. These models consider the

interactions between microcracks, lattice dislocations and grain boundaries, and are shown to make a general prediction of the grain size effect.

The last main sections of the report give the surveys of diagnostic techniques and remedial measures. The diagnostic techniques can be well specified. They include visual inspection, X-ray radiography, optical and SEM metallography (the latter combined with EDX or WDX chemical analysis), microhardness testing and SEM fractography. The most definitive technique, with the broadest diagnostic scope, is SEM metallography. The remedial measures that could or should be taken during restoration and conservation − particularly restoration − are less certain. Suggested remedies are intended to be used as a guide, whereby each case has to be considered on its own merits.

The report ends with a number of conclusions and suggestions for further research.

KEYWORDS: ARCHAEOLOGICAL SILVER, EMBRITTLEMENT, CRACKS, GRAIN BOUNDARIES, SEGREGATION, CORROSION, GRAIN SIZE, MICROSTRUCTURE, METALLOGRAPHY, FRACTOGRAPHY, RESTORATION, CONSERVATION

INTRODUCTION

Silver is normally malleable, ductile and easily fabricated. However, some archaeological silver artifacts and coins can be brittle, as a long-term consequence of corrosion and microstructural changes (Thompson and Chatterjee 1954; Werner 1965; Organ 1977; Kallfass *et al*. 1985; Ravich 1993; Wanhill *et al*. 1998; Wanhill 2000a, 2001). Here it is opportune to distinguish broadly between the types of embrittlement:

(1) Corrosion-induced embrittlement is a consequence of selective corrosion that penetrates the metal and eventually fragments it (Werner 1965; Organ 1977; Ravich 1993; Wanhill *et al*. 1998). This occurs whether or not the object is acted upon by external loads or forces, though they may hasten the process, as will internal stresses and strains (Wanhill *et al*. 1998; Lichter *et al*. 2001).

(2) Microstructurally-induced embrittlement causes apparently pristine metal to crack and fracture under the action of external loads or forces (Wanhill *et al*. 1998).

Despite these distinctions, it is important to note that corrosion-induced and microstructurally-induced embrittlement can act synergistically, and that microstructural features are involved in both types of embrittlement (Wanhill *et al.* 1998; Wanhill 2000a, 2001).

The present report is concerned mainly with defining and explaining these types of embrittlement, their probable mechanisms, and the severity of embrittlement, based on current metallurgical knowledge and concepts. However, surveys are included of the diagnostic techniques for determining embrittlement and the possible remedial measures that could or should be taken during restoration and conservation.

CORROSION-INDUCED EMBRITTLEMENT

Evidence and description of the types of corrosion

Figure 1 illustrates the types of corrosion observed for archaeological silver having a high silver content. The examples are eclectic: a Roman cup (Werner 1965), a late Roman plate (Bennett 1994), a Sican tumi (Scott 1996) and an Egyptian vase (Wanhill *et al.* 1998).

General corrosion in high silver content alloys[H] is slow conversion of the metal surface to silver chloride (Gowland 1918; Organ 1977; Scott 1996). The silver chloride forms a brittle, finely granular layer but does not affect the remaining metal's integrity. However, unfavourable conditions may result in an object being completely converted to silver chloride, sometimes retaining its shape, sometimes not (Gowland 1918; Organ 1977).

The other types of corrosion penetrate the metal along selective paths. Cracking along these corrosion paths reduces an object's resistance to fragmentation (Werner 1965; Ravich 1993; Wanhill *et al.* 1998). Intergranular corrosion is the most commonly reported type. This can occur in mechanically worked and annealed objects, which constitute the majority. Interdendritic corrosion can occur in castings with essentially as-cast microstructures, i.e. little changed by any subsequent mechanical working or annealing, see Scott (1996). However, cast archaeological silver objects are uncommon, notwithstanding Scott's metallograph in figure 1.

Corrosion along slip lines and deformation twin boundaries can occur in an object that has not been annealed after (final) mechanical working, which includes striking a coin (Thompson and

---

[H]   Base silver containing major amounts of copper undergoes general corrosion whereby the copper
      diffuses out of the alloy and becomes fixed on the surface as green copper carbonates (Organ 1977).

Chatterjee 1954) and decorating by chasing and stamping (Wanhill *et al*. 1998). Inside the metal these types of attack can lead to additional corrosion along segregation bands. These bands are the remains, modified by mechanical working and annealing heat-treatments, of solute element segregation (coring) and interdendritic segregation that occurred during solidification of an ingot or cupelled button.

Cracking along the corrosion paths in the metal usually results in irregular fracture surfaces having a finely granular appearance like that of the general corrosion in the upper SEM fractograph in figure 1. However, highly localised corrosion along slip lines and deformation twin boundaries results in crystallographic, faceted fractures, for example the lower SEM fractograph in figure 1.

Mechanisms of corrosion-induced embrittlement

Intergranular corrosion

Intergranular corrosion has been attributed, at least partly, to segregation of the solute element copper to grain boundaries (Werner 1965; Ravich 1993). This segregation is of a special type called discontinuous (or cellular) precipitation[H], and it appears to be associated with − and sometimes the cause of − a meandering appearance of the grain boundaries (Smith 1965; Schweizer and Meyers 1978a, 1979). Figure 2 shows some examples.

Discontinuous precipitation of copper in silver-copper alloys occurs in the solid state at temperatures as low as 200 °C (Predel and Ruge 1968; Scharfenberger *et al*. 1972; Gust *et al*. 1978) and might occur very slowly even at ambient temperatures (Schweizer and Meyers 1978b, 1979). This is discussed in more detail in Appendix A.

The actual mechanism of intergranular corrosion is localised galvanic attack, whereby in the presence of a moisture-containing environment the more noble metal (in this case the copper-depleted silver matrix) acts as a cathode and the copper-enriched grain boundary regions dissolve anodically.

[H] It is important to note that copper precipitation at grain boundaries should be discounted as a cause of *microstructurally*-induced embrittlement. This possible causal connection was suggested, somewhat less specifically, by Smith (1965) and Werner (1965). My assertion that copper is not responsible for microstructurally-induced embrittlement is based on mechanical property and other empirical evidence (Norbury 1928; Thompson and Chatterjee 1954; Wanhill *et al*. 1998) and empirical and theoretical concepts of microstructurally-induced embrittlement (Wanhill 2001). These topics are considered in the sub-section of this report concerning the mechanism of microstructurally-induced embrittlement.

Interdendritic and segregation band corrosion

These types of segregation-induced corrosion are also due to solute element (copper) segregation, which in these cases occurs at high temperatures during solidification of the metal. Their origin lies in the process of solidification by dendrite formation, whereby gradients in solute content occur in the dendrites themselves and between the dendrites and the final solidifying liquid. This is illustrated schematically in figure 3. An actual example was already given in figure 1 (Scott 1996), which shows the solidified interdendritic metal and its preferential corrosion from the outer surface.

Even so, cast archaeological silver objects are uncommon, as mentioned before. Most objects were made from cast metal by mechanical working (usually cold-work) and annealing. Figure 4 is a schematic of the microstructural changes owing to this fabrication method. The final microstructure would − or might − be expected to have a uniform composition, particularly if there had been repeated cycles of working and annealing. However, the segregation can be very persistent in silver alloys. An example is given in figure 5. This is a SEM metallographic cross-section of the wall of an Egyptian silver vase (Wanhill *et al*. 1998). The segregation is visible as numerous bands that result from many cycles of working and annealing.

The mechanism of interdendritic and segregation band corrosion is most likely the same as for intergranular corrosion, i.e. localised galvanic attack of the less noble copper-enriched regions.

Slip line and deformation twin boundary corrosion

Corrosion along slip lines and deformation twin boundaries will be discussed first in a general way. Slip, which occurs in bands, and deformation twinning involve locally high strains whereby some atoms are in non-equilibrium positions and have higher energies. In slip bands these are the atoms surrounding dislocation cores, and in deformation twins they are the atoms in noncoherent regions of the twin/matrix interfaces. When slip bands and deformation twin boundaries are surface-connected, these higher energy regions are exposed to the environment and are consequently susceptible to preferential corrosion (e.g. Procter 1994, 1:37)

More specifically, for silver there are additional factors that could promote corrosion along slip lines and deformation twin boundaries. These are silver's low stacking fault energy[H] (Hertzberg 1983, 80, 129) which results in planar slip and hence greater concentrations of dislocations in slip bands; the narrowness of the deformation twins, e.g. the SEM metallograph in figure 1, and hence the higher local strains associated with them (Hertzberg 1983, 111); and for archaeological silver the possibility of long-term segregation of solute and impurity elements to the highly strained regions, thereby aiding preferential corrosion (Procter 1994, 1:39).

Recently three models have been proposed that link corrosion along slip lines to transgranular stress corrosion cracking (SCC) in alloys with the same crystal structure as silver (Flanagan *et al.* 1991, 1993; Lichter *et al.* 1996; Magnin 1996, 114; Magnin *et al.* 1996; Lichter *et al.* 2001). SCC is an important topic in its own right, though not necessarily relevant to corrosion-induced embrittlement of archaeological silver. The models and associated concepts and observations concerning archaeological silver are discussed in Appendix B, where it is concluded that the strain-enhanced dissolution model of Lichter *et al.* (2001) provides an explanation of crystallographic fracture in archaeological silver along slip planes and occasional non-slip planes.

MICROSTRUCTURALLY-INDUCED EMBRITTLEMENT

Evidence and description of embrittlement

It has long been known that certain elements can embrittle silver, notably lead and tin (Ercker 1574) and antimony (Gowland 1918). The first detailed investigation appears to be due to Thompson and Chatterjee (1954). They studied the embrittlement of silver by age-hardening (age-embrittlement), prompted by the brittleness of archaeological silver coins that must have been ductile when struck.

Thompson and Chatterjee analysed fifteen brittle silver coins, finding copper and lead in appreciable quantities, but no other element except as a trace. The copper contents were up to several weight % and the lead contents varied from 0.25-1.6 wt. %. From these analyses they considered that embrittlement could be due to age-hardening owing to precipitation of lead from

---

[H] In metals having crystal structures with close-packed atomic arrangements, including silver, the slip plane dislocations can dissociate to form two partial dislocations bounding a stacking fault, which is a local "error" in the atomic arrangement. The lower the stacking fault energy, the wider the stacking fault, and the more difficult it is to recombine the partial dislocations to allow them to glide onto other slip planes (so-called wavy slip behaviour). Consequently, a low stacking fault energy favours dislocation movement being restricted to the original slip plane (so-called planar slip behaviour).

supersaturated solid solution in the silver matrix of Ag-Pb or Ag-Cu-Pb alloys. They provided evidence for this possibility as follows:

(1) By determining the silver-rich low temperature region of the Ag-Pb phase diagram, figure 6. This required weeks and months of ageing supersaturated solid solutions of lead in silver, and showed that a lead-rich phase (β) precipitates out of solution even at very low lead contents, less than 0.1 wt. %, and down to ambient temperatures.

(2) By mechanically testing age-hardened Ag-Pb, Ag-Cu-Pb and Ag-Cu alloys, figure 7, and showing that prolonged ageing led to brittle fracture of the lead-containing alloys.

However, lead-rich precipitates may not be necessary. Wanhill *et al*. (1998) examined a severely embrittled Egyptian silver vase, figure 8a. Microstructurally-induced embrittlement was entirely intergranular with "clean" grain boundary facets and no sign of precipitates. This is illustrated in figure 8b, with the caveat that features on the grain boundary facets are due to localised corrosion *after* fracture[H]. The intergranular cracks were characteristically narrow and sharp except where grains became bodily displaced, which is itself a characteristic of severe embrittlement. One such displacement is shown in figure 8b. This fractograph also shows no evidence of plastic deformation of the grain boundaries.

In view of the vase metal analysis (in wt. %: 97.1 Ag-0.9 Cu-0.8 Au-0.7 Pb-0.3 Sb-0.2 Sn) and a theory of adsorption-induced embrittlement (Seah 1980a), Wanhill *et al*. concluded that embrittlement could have been due to atomic segregation of lead to grain boundaries and a consequent reduction in their cohesive strength (Wanhill *et al*. 1998; Wanhill 2000a). This hypothesis leads directly to the next sub-section of this report.

<u>Mechanism of microstructurally-induced embrittlement</u>

There have been three suggestions as to the cause of microstructurally-induced embrittlement in archaeological silver. These are copper precipitation at grain boundaries (Smith 1965; Werner 1965; Schweizer and Meyers 1978a), lead precipitation at grain boundaries (Thompson and Chatterjee 1954; Werner 1965), and atomic segregation of lead to grain boundaries (Wanhill *et al*. 1998).

[H] Presumably long-term environmental exposure caused many grain boundary facets to become locally corroded where slip lines, deformation twin boundaries and segregation bands intersected the intergranular fracture surfaces. See also the discussion of synergistic embrittlement in this report.

Empirical evidence on the effects of copper

The suggestion that copper precipitation at grain boundaries could cause microstructurally-induced embrittlement of archaeological silver is challenged by two lines of evidence. Perhaps the best evidence, obtained for other purposes, is provided by Norbury (1928). Figure 9 shows mechanical property data and a representative metallograph from Norbury's study of solutionised, quenched and aged standard silver (Ag-7.5 wt. % Cu). Ageing resulted in discontinuous precipitation of copper at the grain boundaries and significant changes in tensile strength and elongation. Nevertheless, the *minimum* tensile elongation was about 34 %, which still indicates high ductility and certainly not embrittlement. Note that Thompson's and Chatterjee's results, figure 7, agree with Norbury's in that a lead-free silver-copper alloy was unembrittled by ageing.

The second line of evidence comes from ageing experiments by Ageew *et al*. (1930) and the severely embrittled Egyptian vase investigated by Wanhill *et al*. (1998). Figure 10 shows the most relevant ageing data: solutionised and quenched silver-copper alloys were aged for more than 600 hours at 200 °C, resulting in an age-hardening response from the alloys containing 4.25-7.5 wt. % copper, but no change in hardness for an Ag-2.3 wt. % Cu alloy. The Egyptian vase contained only about 0.9 wt. % copper. This is most probably too little to elicit an ageing response, even at temperatures exceeding 200 °C; and anyway the vase had cold-work retained in the microstructure (Wanhill *et al*. 1998), which excludes heating much above ambient temperatures.

Empirical and theoretical metallurgical concepts

The starting point for this extensive sub-section is the observation that microstructurally-induced embrittlement and precipitation or segregation of *impurity* elements to grain boundaries are characteristic of elements having very low primary solid solubilities in the parent metal matrix (Seah 1980b; Shewmon 1998). The topics to be considered are (1) primary solid solubility, (2) equilibrium grain boundary segregation, (3) grain boundaries and (4) alloy phase diagrams, non-equilibrium cooling and mechanical behaviour, followed by (5) a summary.

(1) Primary solid solubility is governed by atomic size differences between the solute and solvent and by the tendency to form intermediate phases and intermetallic compounds. These observations can be expressed, in order of importance, by the size-factor rule; the electrochemical differences and hence chemical affinities of the alloying components; and the electron concentration change upon alloying (Hume-Rothery and Raynor 1954; Pettifor 1984, 1988; Massalski 1996).

The size-factor rule states that when the atomic diameters of solute and solvent differ by more than 14-15 %, the size-factor is unfavourable and the primary solid solubility will generally be restricted to a few atomic per cent. It is, however, a negative rule: favourable size-factors do not necessarily mean high solid solubilities. Figure 11 illustrates the rule for solid solutions in silver. Rubidium, potassium and sodium have very unfavourable size-factors and, as table 1 shows, zero solid solubility. They are followed by lead, bismuth and thallium, with solid solubilities less than 8 at. %.

The next criterion, electrochemical difference and chemical affinity, is simply that the greater the electrochemical difference between solute and solvent, the greater is their affinity and tendency to form intermediate phases and intermetallic compounds. In turn, this means primary solid solubility will be restricted (Hume-Rothery and Raynor 1954; Massalski 1996). The electrochemical difference is quantifiable by differences in electronegativity of the alloying components (Pauling 1945, 1947; Darken and Gurry 1953; Gordy and Thomas 1956).

Much effort has been put into combining the size-factor rule and electronegativity differences on Darken-Gurry (D-G) maps, e.g. Darken and Gurry (1953), Waber *et al*. (1963), Gschneider (1980). D-G maps are supposed to enable predictions whether solid solubility is low or moderate-to-high. Figure 12 shows a D-G map for solid solutions in silver, using data from table 1. Solute elements outside the ellipse should have low solid solubilities, while elements within the ellipse are predicted to have solid solubilities greater than 5-10 at. %. However, again using table 1, we see that this latter prediction is incorrect with respect to tellurium. Also, lithium, palladium, arsenic and antimony are incorrectly predicted to have low solid solubility. These and other inadequacies of D-G maps have been explained by Gschneider (1980) in a general way, i.e. not specifically considering silver as the solvent. To overcome these inadequacies Gschneider presented several new rules, which he realised would make D-G maps largely unnecessary.

More recently, Pettifor (1984, 1988) derived a series of the elements that goes beyond electronegativity by also acknowledging the chemical similarity of elements from the same Group of the Periodic Table. Each element is given an empirical ordering number, and examples are given in table 1. Pettifor demonstrated the usefulness of this deceptively simple empirical approach by showing it enabled systematic separation of the crystal structures of many binary intermetallic compounds.

The third factor to consider is the electron concentration, which is the ratio of valence electrons to the number of atoms. Empirical studies of binary gold, silver and copper alloys, in particular with B-subGroup elements, have shown that when the effects of size-factor and electrochemical difference are "relatively small", the primary solid solubility limits occur at fairly constant values of electron concentration (Hume-Rothery and Raynor 1954). In a famous theory, Jones (1937) provided an explanation of this phenomenon and derived a theoretical critical electron concentration of 1.41.

Figure 13 illustrates the electron concentration effect for binary silver alloys, whereby the solutes have favourable size-factors but the combination of electronegativity and chemical differences, expressed by Pettifor's empirical ordering sequence, increases in going from cadmium to antimony. Most of the alloys have primary solid solubility limits at electron concentrations between 1.35-1.42, agreeing well with Jones' theory. (However, this theory is known to have some problems (Cottrell 1988; Massalski 1996).)

(2) <u>Equilibrium grain boundary segregation</u> involves the solid state redistribution of solute elements and their adsorption at grain boundaries. Solutes of low solubility generally segregate strongly and vice versa (Seah 1980b). Another important characteristic is that at the commonly observed levels of segregation many elements co-segregate rather than compete for grain boundary adsorption sites (Hondros and Seah 1977; Seah 1980b).

This type of segregation can greatly reduce the cohesive strength of grain boundaries, leading to grain boundary fracture and embrittlement (Seah 1980a, 1980b; Shewmon 1998), and Seah (1980a) has developed a theory of embrittlement owing to adsorption-induced grain boundary decohesion. Figure 14 shows the theory's predictions for segregant elements in silver. This figure should be interpreted as follows: elements with sublimation enthalpies lower than those of the matrix will, *if segregated*, cause embrittlement of the matrix grain boundaries, and the embrittling effect will be greater the lower the sublimation enthalpy of the segregant element. (The sublimation enthalpy is a measure of the heat required to evaporate atoms from the solid surface of an element.)

Figure 15 correlates alloying element primary solid solubility limits in silver with their sublimation enthalpies. The elements are arranged according to Pettifor's (1988) empirical ordering numbers and unfavourable size-factors are indicated. The colour-shaded regions in this figure indicate the matrix and alloying element combinations that would seem most likely to result in segregation-induced grain boundary fracture under equilibrium conditions: silver containing sodium, potassium, rubidium, lead, bismuth, tellurium or

selenium. There are other possibilities, namely silver containing thallium, germanium, antimony or arsenic.

However, the key question, unanswerable by figures 14 and 15, is whether the indicated alloying elements actually segregate to grain boundaries to cause embrittlement. Another important question is whether they might cause embrittlement in another way. To try to answer these questions, and also to explain the observed embrittlement of silver discussed earlier, it is necessary to consider the grain boundary characteristics of archaeological silver, the binary silver alloy phase diagrams, the effects of non-equilibrium cooling on the phase changes, and the likely mechanical behaviour of the alloys.

(3) <u>Grain boundaries</u> strongly influence the properties of metals and alloys, and there is much evidence that grain boundaries have different properties depending on their character, i.e. their type and structure (e.g. McLean 1957; Chadwick and Smith 1976; Baluffi 1980; Watanabe 1984, 1993, 1994; Watanabe *et al*. 1980, 1989; Lim and Watanabe 1990).

From the literature and their own research Watanabe (1984, 1993, 1994) and Watanabe *et al*. (1980, 1989) suggested dividing grain boundaries into three character-determined categories: low-angle boundaries with misorientation angles less than 15°; high-angle coincidence boundaries with low Σ coincidence[G]; and high-angle random boundaries. The basic distinguishing property is that low-angle and low Σ coincidence boundaries are low-energy boundaries, while random boundaries are high-energy boundaries. This difference is important for many other properties, including impurity element segregation, which occurs preferentially to high-angle random grain boundaries (Watanabe *et al*. 1980). This is illustrated schematically in figure 16, which also shows – consistent with observations (Seah 1980b) – that segregation tends to be greater for impurity elements having less primary solid solubility.

This distinction between grain boundary types and structures is informative for microstructurally-induced embrittlement of archaeological silver artifacts. These were usually made using combinations of mechanical working and annealing heat-treatments. The resulting microstructures most probably contain a majority of high-angle random grain boundaries, see by analogy Watanabe (1984) and Watanabe *et al*. (1989). In turn, this suggests that archaeological silver artifacts contain many grain boundaries that would be very susceptible to impurity element segregation *if it occurred*.

[H] A coincidence boundary has the geometrical property of representing a lattice plane common to contiguous grains. A boundary with *low* Σ coincidence means the contiguous grains have orientations resulting in a *high* density of coincident lattice sites on the boundary, which therefore is a *low*-energy boundary.

Furthermore, despite the presence of other types of grain boundary, the likely preponderance of high-angle random grain boundaries in archaeological silver artifacts means it is reasonable, and indeed consistent with empirical observations (Werner 1965), to apply a simple length scale criterion – based on the average grain size or diameter – to crack initiation. This is considered in the section of this report on the effect of grain size.

(4) <u>Alloy phase diagrams, non-equilibrium cooling and mechanical behaviour</u>. Table 2 lists the equilibrium phase diagram characteristics and ambient temperature phases for dilute silver binary alloys whose alloying elements have low primary solid solubilities.

Phase changes for the alloys in sub-table 2.1 should be independent of cooling rate, within normal metallurgical variations. This basic independence of cooling rate means that in the as-cast condition there will always be intercrystalline or intergranular phases. These are usually brittle intermetallic compounds and cause poor mechanical behaviour. Evidence for this is provided by Roberts-Austen's experiments on binary gold alloys (Roberts-Austen 1888; Wanhill 2000b).

Phase changes for the alloys in sub-tables 2.2 and 2.3 will depend on cooling rate. This will be illustrated with the aid of figure 17, which shows schematic binary alloy equilibrium phase diagrams involving eutectic or peritectic reactions. Consider two dilute alloys whose bulk compositions approach the primary solid solubility limits, α_3, and are represented by the vertical lines meeting the abscissae at X. Non-equilibrium cooling has two major effects on the phase changes:

(a) If cooling is fast enough the solidification compositions follow the curves α_1–$\alpha_3{}'$ rather than α_1–α_3. This means the solid solubilities are reduced, final solidification is at temperatures T_3 instead of T_2, the last liquids to solidify have compositions L_3 instead of L_2, and the alloys do not finally solidify only as α. Instead the eutectic or peritectic reactions occur at T_3: the remaining liquids either solidify as eutectic $\alpha+\beta$ between the primary α crystals or grains, or else react – the peritectic reaction – with some of the primary α crystals or grains to form β between them.

(b) Suppression of solid state reactions and the retention of metastable phases down to ambient temperatures. This is possible because the diffusion of atoms is much slower in solids than in liquids. From figure 17 we see that under equilibrium conditions the two alloys undergo solid state partial decomposition ($\alpha \rightarrow \alpha+\beta$) at temperatures below T_4. However, faster cooling will cause supersaturated α to be retained, at least temporarily, down to ambient temperatures.

These effects may be interpreted to some extent for the alloys in sub-tables 2.2 and 2.3. Firstly, non-equilibrium cooling could cause alloys with bulk compositions below $PSSL_{max}$ or $PSSL_{eut}$ to finally solidify as though their bulk compositions were above these limits, leading to poor mechanical properties. *Indirect* evidence for this is the behaviour of gold containing thallium. In this system the solid solubility of thallium becomes zero well above the eutectic temperature, resulting in eutectic Au+Tl between the primary crystals or grains however dilute the alloy (Baker *et al.* 1992; Wanhill 2000b). Roberts-Austen (1888) noted the "crystalline structure" of the fracture surface of an as-cast Au-0.2 wt. % ($\approx$ 0.2 at. %) Tl bar whose ductility was low.

Secondly, the solid state decomposition reactions listed in the last two columns of sub-tables 2.2 and 2.3 could be partially or wholly prevented by non-equilibrium cooling. Subsequent ageing at low or even ambient temperatures could then result, in some cases, in alloying element segregation and precipitation, and mechanical behaviour deterioration and embrittlement. The archetype is provided by the Ag-Pb alloy experiments of Thompson and Chatterjee (1954), discussed earlier in this section of the report and illustrated by figures 6 and 7. Other – candidate – systems are silver containing arsenic, bismuth and thallium. On the other hand, the Ag-Sb and Ag-Sn systems are less likely to belong to this category, even though antimony and tin can embrittle silver (Ercker 1574; Gowland 1918). The reason is that the solid solubilities of antimony and tin in silver are still significant at ambient temperatures, see sub-table 2.2. Finally, the Ag-Ge system would appear to be excluded, since germanium has a higher sublimation enthalpy than silver, see table 1 and figures 14 and 15.

(5) <u>Summary</u>. The foregoing empirical and theoretical metallurgical concepts enable specifying which elements, in amounts less than about 5 at. %, could embrittle or impair the mechanical behaviour of silver. There are two categories, alloys most probably embrittled as-cast, and alloys that could be embrittled by low temperature ageing that results in alloying element segregation and precipitation. These categories are given below, whereby asterisks indicate known embrittlement or poor mechanical behaviour of dilute alloys (Thompson and Chatterjee 1954; Raub 1995):

(a) As-cast :   Ag-Bi, Ag-Na, Ag-Pb, Ag-Rb, Ag-Se, Ag-Te*.

(b) Aged   :   Ag-As, Ag-Bi, Ag-Pb*, Ag-Tl.

For both categories the presence of more than one of the specified elements could be cumulatively detrimental. This is probable for aged alloys in which impurity elements have segregated to grain boundaries since, as remarked earlier, many elements co-segregate rather than compete for grain boundary adsorption sites.

For archaeological silver only the second category – aged alloys – is likely to be relevant. Most artifacts were made by subjecting buttons or ingots with as-cast microstructures to mechanical working and intervening annealing heat-treatments. As-cast embrittlement could not have been tolerated: the silver would have been reprocessed until malleable and ductile. By the same token, however, the microstructures of most artifacts will contain many high-angle random grain boundaries, which should be very susceptible to impurity element segregation owing to low temperature ageing.

Composition of archaeological silver

Native silver alloys may or may not have been used for Old World archaeological artifacts (Lucas 1928; Gale and Stos-Gale 1981a; Philip and Rehren 1996). However, the general scarcity of native silver compared to silver-containing minerals, mostly lead ores, and the early development of lead cupellation resulted in pyrometallurgy becoming the main source of silver (Gowland 1918; Gale and Stos-Gale 1981a, 1981b; Tylecote 1986; Raub 1995).

Cupellation is very effective in producing silver above 95 wt. % purity (Tylecote 1986, 1987), though it usually contains minor-to-trace amounts of gold, copper, lead and bismuth, and traces of antimony, arsenic, tellurium, zinc and nickel (McKerrell and Stevenson 1972; Gale and Stos-Gale 1981a; Raub 1995). Gold, copper, lead and bismuth contents are generally below 1 wt. % for each element: higher copper and lead contents in finished artifacts and coins, and also tin or zinc above 0.1 wt. %, suggest or indicate deliberate alloying, see McKerrell and Stevenson (1972) and Gale and Stos-Gale (1981a).

Figure 18 quantifies actually or potentially embrittling elements found in archaeological silver artifacts and coins lying within two ranges of high silver content. Though there are wide variations, lead is the main impurity, averaging 0.5-1 wt. %. Bismuth, antimony and tin are generally below 0.5 wt. %.

Most probable mechanism

The evidence and description of microstructurally-induced embrittlement, the non-embrittling effects of copper during the ageing of silver-copper alloys, and empirical and theoretical metallurgical concepts of embrittlement point to a mechanism involving long-term low temperature segregation of an impurity element, or co-segregation of impurity elements, to grain boundaries. The candidate impurity elements are arsenic, bismuth, lead, thallium and – less probably – antimony and tin.

Lead is the most likely perpetrator. This is inferred from the long-term ageing experiments and brittle coin analyses by Thompson and Chatterjee (1954); the Egyptian vase investigated by Wanhill *et al.* (1998), which contained lead, antimony and tin, but no detectable arsenic or bismuth; and the impurity element contents of many artifacts and coins, figure 18, where it is seen that lead is the main impurity. However, embrittlement by other impurity elements, notably bismuth, see figures 15 and 18, is possible, especially in co-segregating action with lead.

SYNERGISTIC EMBRITTLEMENT

As stated in the introduction to this report, corrosion-induced and microstructurally-induced embrittlement can act synergistically (Wanhill *et al.* 1998; Wanhill 2000a, 2001). Figure 19 gives examples of the appearances of synergistic embrittlement. Corrosion along slip lines, deformation twin boundaries and segregation bands can result in cracks under the action of external loads or forces (e.g. crushing pressures during interment) and internal residual stresses due to retained cold-work. These cracks can then initiate fracture along microstructurally embrittled grain boundaries – which may fracture anyway, though less easily – under the action of external loads or forces. In turn, grain boundary fractures expose more slip lines, deformation twins and segregation bands to the environment and therefore increase the opportunities for corrosion.

The recognition of synergistic embrittlement is presently limited to the Egyptian silver vase investigated by Wanhill *et al.* (1998). However, figure 20 shows another probable example, an Indian silver coin examined by Thompson and Chatterjee (1954). Be that as it may, the effect of synergistic embrittlement is to render an object frangible, or even friable if it is also large-grained, see the section of this report on the effect of grain size.

It is worth noting here that the lower fractograph in figure 19 illustrates a point made earlier during the description of microstructurally-induced embrittlement: namely that besides crack formation, e.g. in the left-hand segregation band in the fractograph, the contribution of selective corrosion to synergistic embrittlement includes local corrosion of "clean" grain boundary facets produced by microstructural embrittlement.

Observe also that the annealing twin boundaries in the upper right fractograph of figure 19 are uncorroded. Apparently, the local environmental conditions were not severe enough to cause selective corrosion at these twin/matrix interfaces, which by nature are coherent and without highly strained regions.

NOTES ON THE OCCURRENCE OF EMBRITTLEMENT

The remarks immediately preceding this section, concerning uncorroded annealing twin boundaries, serve as an introduction to the following noteworthy points:

(1) Opinions differ on the extent of the problem of archaeological silver embrittlement. Schweizer and Meyers (1979) and Kallfass *et al.* (1985) state that ancient silver objects are often found to be in an extremely brittle condition. However, Northover (1999) has investigated some 300 silver vessels and over 2000 silver alloy coins and found only a small proportion to be badly embrittled. On neutral ground, Thompson and Chatterjee (1954) and Werner (1965) state that it is well-known that certain silver objects have become very brittle.

(2) Another important point, in view of the most probable embrittlement mechanisms, is the primary significance of the copper and lead contents. Archaeological silver frequently contains more than 1-3 wt. % copper and 0.1 wt. % lead (Gale and Stos-Gale 1981a; Bennett 1994): see figure 18 and Appendix D also. Exceedance of these fairly low values should make possible corrosion-induced embrittlement owing to the discontinuous precipitation of copper (which can occur, albeit at elevated temperatures, for copper contents above 2 wt. %, see figure 10 and Ageew *et al.* 1930) and microstructurally-induced embrittlement due to lead, see figure 6 and Thompson and Chatterjee (1954).
Thus embrittlement should be due to an adverse combination of factors besides the copper and lead contents. These factors include the object's manufactured condition and burial time, the average temperature, moisture content and chemical composition of the burial

environment, especially the salt, nitrate and nitrite contents (Gowland 1918), and probably the overall pH^G of the burial environment as well.

(3) With respect to an object's manufactured condition, the retention of plastic deformation (cold-work and residual internal stresses) in the microstructure should facilitate and accelerate discontinuous precipitation of copper (Hornbogen 1972; Pawlowski 1979a, 1979b) and microstructurally-induced embrittlement by lead (Thompson and Chatterjee 1954). However, whether enhanced discontinuous precipitation of copper necessarily increases the occurrence of corrosion-induced embrittlement is questionable: Northover (1999) observed that "intergranular cracking/corrosion is most prevalent at low concentrations of copper, i.e. in circumstances where discontinuous precipitation of copper is likely to be minimal, if present at all."

THE EFFECT OF GRAIN SIZE

Grain boundary character

As discussed in the extensive sub-section on empirical and theoretical metallurgical concepts, microstructurally-induced embrittlement should mostly affect high-angle random grain boundaries, which very likely predominate in the microstructures of archaeological silver artifacts. This has two important implications:

(1) Archaeological silver objects will contain many grain boundaries susceptible to microstructurally-induced embrittlement, assuming that impurity element segregation has occurred.

(2) A preponderance of high-angle random grain boundaries makes it reasonable, and indeed compatible with empirical observations (Werner 1965), to consider embrittlement in terms of length scale criteria based on the average grain size or diameter.

---

^{H} The pH notation expresses hydrogen ion activities in aqueous solutions and also (wet) soils. The pH of a neutral solution is 7. Acid solutions have pH less than 7; alkaline solutions have pH greater than 7. The same is true for soils.

Grain size and embrittlement

Archaeological silver may have large grain sizes, more than 0.1 mm, e.g. Werner (1965), Wanhill *et al*. (1998), and Werner's metallograph in figure 1. Large grains are due to the annealing heat-treatments that were usually involved in artifact manufacture. The heat-treatments were more or less uncontrolled, by modern standards, and the metalsmiths would likely over-anneal to ensure malleability and ductility during further mechanical working and finishing.

Werner (1965) stated that larger grain sizes are a primary cause of silver embrittlement. This is incorrect – or at least imprecise – since large grain size silver is usually ductile (Wanhill *et al*. 1998), as attested also by the successful manufacture of large-grained archaeological silver artifacts, and by mechanical testing of silver single crystals (Andrade and Henderson 1951; Rosi 1954). In particular, Rosi (1954) observed ductile behaviour in large cylindrical single crystals 9.5 mm in diameter and 127 mm long.

However, Werner's observations do show that grain size must be an important, albeit secondary, factor for silver embrittlement. Four reasons can be given. These are discussed in the following sub-sections.

Intergranular corrosion

A large grain size facilitates penetration of intergranular corrosion into an object. This is clearly demonstrated by Werner's metallograph in figure 1. The artifact concerned is a severely embrittled Roman cup (Werner 1965) with grain sizes up to 0.4 mm, which is nearly the full thickness of the cup wall.

Impurity element segregation

Microstructurally-induced embrittlement caused by impurity element segregation to grain boundaries is likely to be exacerbated by a larger grain size. This will be explained using the schematics in figure 21, which show two possible dependences of the degree of embrittlement, represented by the local fracture stress, σ_f, on impurity element concentration at grain boundaries.

Figure 21a shows a "threshold" concept of embrittlement, for which the local fracture stress abruptly drops to a minimum value at a critical impurity concentration C_{cr}. This concept predicts no effect of grain size on embrittlement once C_{cr} is reached. Figure 21b shows a more realistic representation of embrittlement (Thompson and Knott 1993), whereby the local fracture stress decreases gradually to a minimum at a critical impurity concentration C_{cr}^*. For this behaviour larger grain sizes can increase embrittlement: larger grains mean less grain boundary area to be embrittled by the impurity elements in an object, and hence increased concentrations of impurities at the grain boundaries and increased embrittlement. (This assumes, however, that C_{cr}^* is not easily reached and that thermodynamic equilibrium has not been attained.)

Microcrack initiation and micromechanical crack models

Embrittlement is manifested by cracking under the action of external loads or forces and internal residual stresses, if present. Cracking begins with *microcracks* smaller than or equal to the grain size. At this size or length scale the average grain size or diameter, d, symbolising a preponderance of high-angle random grain boundaries, is likely to strongly influence crack initiation.

Figure 22 depicts micromechanical crack models applicable to archaeological silver embrittlement. These models are described in detail, but mainly non-mathematically, in Appendix E. Here the models are summarised in the following sub-paragraphs.

- Figure 22a: This is the classic dislocation pile-up model of microcrack initiation, applicable to corrosion-induced and microstructurally-induced embrittlement, whereby corrosion or impurity element segregation reduce the grain boundary fracture energy. The criterion for initiation of a grain boundary microcrack is obtained from Smith and Barnby (1967):

$$\tau_{app} - \tau_i \geq \sqrt{\frac{2\pi\mu\gamma_f}{(1-\nu)\,d}} \bullet \frac{1}{\sqrt{F(\theta)}} \tag{1}$$

  where τ_{app} = applied shear stress; τ_i = lattice friction stress; μ = slip plane shear modulus; γ_f = grain boundary fracture energy; ν = Poisson's ratio; d = grain diameter; $F(\theta)$ = an angular function; S = dislocation source; $\perp$, = edge dislocations of opposite sign.

- Figures 22b-22d: These models are applicable to corrosion-induced and synergistic embrittlement, whereby microcracks develop due to corrosion along slip planes and facilitate initiation of microcracks at grain boundaries weakened by corrosion or impurity element segregation. The criteria for initiation of grain boundary microcracks are:

Fig. 22b
2a < d

$$\tau_{app} \geq \sqrt{\frac{2\pi\mu\gamma_f}{(1-\nu)\,d}} \bullet \frac{1}{\left(1 - \frac{2\tau_i}{\pi\tau_{app}} \bullet \cos^{-1}\left(\frac{a}{d/2}\right)\right)} \bullet \frac{1}{\sqrt{F(\theta)}} \qquad (2)$$

Fig. 22c
2a = d

$$\tau_{app} \geq \sqrt{\frac{2\pi\mu\gamma_f}{(1-\nu)\,d}} \bullet \frac{1}{\sqrt{F(\theta)}} \qquad (3)$$

Fig. 22d
2a = d
multiple slip plane cracks

$$\tau_{app} \geq \sqrt{\frac{2\pi\mu\gamma_f}{(1-\nu)\,d}} \bullet \frac{1}{\left(\sqrt{\frac{3h}{\pi d}} \bullet \left(\frac{d}{h} + 0.2865\right)\right)} \bullet \frac{1}{\sqrt{F(\theta)}} \qquad (4)$$

where h is the distance between multiple slip plane cracks, see for example figure 19. Equations (2) - (4) are derived from equation (1) and the analyses of Tanaka *et al*. (1986) for equation (2) and Tada *et al*. (1973) for equation (4). N.B. For mathematical simplicity these models assume the material to be elastically isotropic and homogeneous. On the scale of individual grains this is incorrect for most metals, including silver (Smithells 1967), but this does not invalidate a generic assessment.

The models make the general prediction that the applied shear stress, τ_{app}, required for initiation of a grain boundary microcrack *decreases* with *increasing* grain size, d, and *decreasing* grain boundary fracture energy, γ_f.

In fact, $\tau_{app} \propto \sqrt{1/d}$, which is the same as the well-known Hall-Petch fracture stress relationship for bulk metals (Hall 1951, Petch 1953). This effect of grain size on the stress required for grain boundary microcrack initiation is very significant. To illustrate this, figure 23 plots ratios of applied shear stress, $\tau_{app_2}/\tau_{app_1}$, versus ratios of average grain diameter, d_2/d_1, whereby it is assumed that small and large grain sizes in archaeological silver are represented by $d_1 = 5\text{-}10\ \mu m$ and $d_2 = 100\text{-}200\ \mu m$, respectively. Figure 23 shows that the applied shear stress required for grain boundary microcrack initiation in the large-grained silver would be only 1/3-1/6 that for the fine-grained silver.

With respect to the grain boundary fracture energy, γ_f, a larger grain size can have two effects that decrease γ_f and hence τ_{app}, thereby promoting grain boundary microcracking. These effects were already discussed in the previous two sub-sections, namely that a larger grain size can facilitate intergranular corrosion and exacerbate microstructurally-induced embrittlement owing to impurity element segregation to grain boundaries.

Microcracks to macrocracks: frangibility and friability

As discussed above, microcrack initiation along grain boundaries weakened by corrosion-induced, microstructurally-induced and synergistic embrittlement will be easier if the grain size is large. Furthermore, a very likely predominance of high-angle random grain boundaries means that archaeological silver objects should contain many grain boundaries susceptible to impurity element segregation and hence microstructurally-induced embrittlement, *if it has occurred*.

The combination of large grain size and a predominance of high-angle random grain boundaries in a microstructurally embrittled object signifies many potential initiation sites for microcracks, and therefore an increased possibility for microcracks to link up and become macrocracks. In other words, a large-grained microstructurally embrittled object is likely to be frangible, even if there is no damage from corrosion.

Be that as it may, it is known that severely corroded large-grained objects are frangible (Werner 1965). And the combination of a large grain size with synergistic embrittlement is even worse: corrosion can initiate microcracks and increase the possibilities for microcrack initiation at microstructurally embrittled grain boundaries, as discussed with reference to figure 19 in the section on synergistic embrittlement, and the object then becomes friable (Wanhill *et al*. 1998).

DIAGNOSTIC TECHNIQUES FOR ARCHAEOLOGICAL SILVER EMBRITTLEMENT

Table 3 provides a survey of the diagnostic techniques for determining the types of embrittlement in archaeological silver. The survey is based on Wanhill (2000a, 2001) and Wanhill *et al*. (1998).

<u>**Visual inspection**</u>

This is more or less obvious, but nonetheless essential. Only visual inspection gives an overall impression of an object's condition. This should be photographically documented, with colour photography as an important option for corroded objects, e.g. Organ (1977).

X-ray radiography

X-ray radiographs can reveal both internal and external "hidden" damage. For example, externally-connected cracks can be obscured by surface topography (shadowing, light-fall), corrosion and any previous restoration. Figure 24 is an X-ray radiograph of the severely embrittled Egyptian vase discussed earlier in this report. The X-rays reveal hairline cracks in the vase and also its incompleteness: if we compare figure 24 with figure 8a it is evident the vase is much restored.

Besides revealing cracks, figure 24 shows important crack patterns. The "eggshell" crack pattern at the upper centre of the X-ray image is diagnostic for very brittle fracture. These cracks occurred most probably under the action of crushing forces. Equally important and very interesting, as will be discussed in the next sub-section, are the arcuate cracks labelled $\boxed{A}$. These cracks follow external chased decorating grooves, identifiable from figure 8a.

Metallography, EDX or WDX, and microhardness testing

Metallography is generally the most important diagnostic technique, especially when combined with chemical analysis by using SEM+EDX or SEM+WDX combinations. EDX is more widely available than WDX, which, however is more accurate and better able to determine the presence of trace amounts of impurity elements, i.e. less than about 0.1 wt. %.

In addition to figures 1, 2, 5, 9, 20 and A.3, the usefulness of metallography is demonstrable from figure 25, which shows a metallograph and schematic for one of the external chased decorating grooves on the above-mentioned Egyptian silver vase. The SEM metallograph used backscattered electron imaging, which revealed a local deformation pattern. The schematic interprets the deformation pattern from the slip-line field theory of indentation (Johnson and Mellor 1962, 333-334). This theory predicts that when $t_i/w = 4.4$ a tension zone forms at the surface opposite the groove, as well as the always-present compression zone directly under the groove. The actual value of t_i/w is 4.2, close enough to justify the interpretation. The tension zone, retained as cold-work in the finished vase, promoted corrosion and intergranular fracture at and near the *internal surface*, i.e. it caused "hidden" damage. The corollary to this interpretation is of general significance: all thin-walled objects with chased decorations should be examined for damage at and near internal surfaces.

With respect to chemical composition, fully quantitative EDX or WDX analyses using elemental standards should provide two kinds of information. Firstly, the analyses should distinguish whether the silver was obtained from lead cupellation, native silver or aurian silver.

However, determination of provenance is more difficult: see, for example, Gale and Stos-Gale (1981a). Secondly, the lead, bismuth, antimony, tin, arsenic, thallium and copper contents are important for diagnosing the types of silver embrittlement, as follows:

(1) Lead is the most likely perpetrator of microstructurally-induced embrittlement of archaeological silver. Long-term segregation or precipitation of lead at grain boundaries can occur at bulk contents less than 0.1 wt. %, see figure 6. Other impurity elements might be involved, notably bismuth, but possibly – and increasingly less likely – arsenic, thallium, antimony and tin.

(2) Corrosion-induced embrittlement is partly or mainly due to copper segregation. At low temperatures, possibly even at ambient temperatures, see Appendix A, copper can segregate to grain boundaries, resulting in discontinuous precipitation and intergranular corrosion. At high temperatures copper segregates during alloy solidification. This type of segregation results in ambient temperature corrosion that is either interdendritic, in essentially as-solidified microstructures, or along relatively copper-rich segregation bands. These bands are the remains of solute element segregation (coring) and interdendritic segregation that have been modified and reduced by mechanical working and annealing.

Furthermore, metallography is an integral part of microhardness testing, which is also a useful diagnostic technique, see table 3. As an illustration, figure 26 demonstrates how microhardness indents can distinguish between corrosion and microstructurally-induced embrittlement. Figure 26a shows a hardness-tested internally corroded area, which underwent craze-cracking mainly *inside* the indented region and had a very low hardness. Figure 26b shows a microstructurally embrittled area that underwent grain boundary cracking mainly *outside* the indented area. The hardness was also much higher, as can be seen from the indent sizes in the metallographs.

Fractography

Fractography is an essential adjunct to metallography, see figures 1, 8, 19, B.1 and B.2, notably – in the present context – for distinguishing between the types of embrittlement in archaeological silver. Detailed fractography requires considerable interpretive skill, for example see Appendix B.

REMEDIAL MEASURES FOR ARCHAEOLOGICAL SILVER EMBRITTLEMENT

Introduction: technical capabilities and ethical considerations

Modern restorations and conservation are concerned, or should be concerned, with both technical capabilities and ethical considerations. Essentially this means that an object's integrity should be respected and restoration and conservation techniques should be *reversible*. However, reversibility is a controversial topic (Oddy and Carroll 1999) and is not always practicable: for archaeological silver see e.g. Organ (1977) and Oddy and Holmes (1992).

Possible remedial measures

Bearing the above remarks in mind, table 4 suggests how the basic condition and type of embrittlement of archaeological silver could result in technically possible and potentially sanctionable remedies.

Nominally intact objects almost certainly would not be heat-treated. Coins are possible exceptions, as indicated in the right-hand column of table 4. The main reason is their small size, which makes them easier to heat-treat. Coins are also likely to be less rare, so that the risks involved in heat-treatment may be perceived as less: see Note C in table 4.

At the other extreme, if it is decided to restore severely embrittled and fragmented objects, then heat-treatment may be essential (Organ 1977; Ravich 1993). The main objection to heat-treatments is that they change the microstructure, and therefore information about an object's manufactured condition and subsequent history can be partially or completely lost. Even worse is the possibility that some future investigator could be confused or misled by the changed microstructure. Also important is that heat-treatments entail a risk of further damage, see Notes C and F in table 4. All these considerations suggest most strongly that heat-treatments should be allowed only if preceded by assessing the object's frangibility or friability (i.e. whether it is safe to handle without the benefit of heat-treatment), a thorough and meticulously recorded diagnostic investigation, and if judged feasible and done by experienced technical staff: see, for example, Oddy and Holmes (1992).

Table 4 also includes a more acceptable remedial measure that is applicable to any embrittled object. This remedy is cleaning, outgassing to dry crack surfaces and any entrapped corrosion products, and application of a protective coating, all to stop further corrosion and embrittlement (Wanhill *et al*. 1998). Some conservators may regard a protective coating, usually to prevent tarnishing, as undesirable (Born 1986). However, even though corrosion-induced and

synergistic embrittlement must be very slow processes, they will most probably continue if atmospheric moisture still has access to the cracks and corrosion damage. Thus in this context a protective coating is truly needed after cleaning and drying.

The choice of cleaning methods and protective coatings requires much forethought and care (see e.g. Organ 1977; Niemeyer 1997; van Reekum and Moll 2000). Recent coating developments (Wood 2000) suggest that "Parylene" coatings should be favoured. These coatings can be "tailored" for specific applications, they are very thin and uniform, and for cracked and corroded objects they have the advantage of being applied by vapour condensation under greatly reduced pressure. This means their application can be *directly* preceded by considerable outgassing and drying of cracks and entrapped corrosion products in the objects.

The need to remove and exclude moisture is also why it may be sanctionable to disassemble old restorations and reassemble with modern non-hygroscopic adhesives and fillers, followed by outgassing and a protective coating. In fact, this is a good procedure, if feasible, whether or not the silver is embrittled by corrosion, since it ensures that not only cracks and entrapped corrosion products are dried, but also any externally-connected crevices between the metal and adhesives and fillers.

Finally, it must be emphasized that although table 4 is quite detailed, and table 3 as well, they should be considered only as guides to investigating and treating embrittled archaeological silver. Whether or not remedial measures should be employed, and which measures, is always an issue of pros and cons: see, for example, Organ (1977), Oddy and Holmes (1992) and Niemeyer (1997). Each case must therefore be considered on its own merits and in the light of current technical capabilities and ethical considerations.

CONCLUSIONS AND SUGGESTIONS FOR FURTHER RESEARCH

Current knowledge enables identifying and providing reasonable explanations of the types of embrittlement of archaeological silver and specifying diagnostic techniques for determining them. However, remedial measures for restoration and conservation are less certain. Suggested remedies should in the first instance be considered as guides, whereby each case is considered on its own merits.

Six detailed conclusions follow:

(1)   Corrosion-induced embrittlement of archaeological silver is due to several forms of selective corrosion: intergranular or interdendritic; along segregation bands; and along slip lines and deformation twin boundaries in objects containing remanent cold-work, resulting in crystallographic fractures.

(2)   All these forms of selective corrosion are due to local galvanic attack, whereby copper segregation has the primary role in intergranular, interdendritic and segregation band corrosion. Corrosion along slip lines and the resulting crystallographic fractures along slip planes are explicable from the strain-enhanced dissolution model proposed by Lichter *et al.* (2001) for copper alloys and austenitic stainless steels. This model also explains occasional crystallographic fracture in archaeological silver on non-slip planes.

(3)   Microstructurally-induced embrittlement of archaeological silver is characterized by grain boundary fracture. The cracks are narrow and sharp, except where grains have become bodily displaced, and there is no evidence of plastic deformation at and near the grain boundaries. The embrittlement is most probably a consequence of long-term low temperature ageing, whereby segregation of an impurity element, or elements, occurs to grain boundaries. The candidate embrittling impurities are lead, bismuth, arsenic, thallium, antimony and tin, in that order. Lead is the most likely perpetrator, but this has yet to be established directly for archaeological silver.

(4)   Corrosion-induced and microstructurally-induced embrittlement of archaeological silver can act synergistically. The effect is to render an object frangible, or even friable if it is also large-grained: see conclusion (6) also.

(5)   In view of the most probable embrittlement mechanisms, the copper and lead contents of archaeological silver are of primary significance. However, since archaeological silver frequently contains more than 1-3 wt. % copper and 0.1 wt. % lead, embrittlement should be due to an adverse combination of factors besides the copper and lead contents. These factors include the object's manufactured condition and burial time, and the average temperature, moisture content, chemical composition and pH of the burial environment.

(6) Grain size is an important secondary factor for archaeological silver embrittlement. Larger grains increase embrittlement in several ways:

- by facilitating penetration of intergranular corrosion
- by enabling increased grain boundary concentrations of the impurities causing microstructurally-induced embrittlement
- by facilitating grain boundary microcrack initiation, which may be involved in corrosion-induced, microstructurally-induced and synergistic embrittlement
- by providing many potential initiation sites for microcracks and easy fracture paths for microcracks to become macrocracks.

Micromechanical fracture models of corrosion-induced, microstructurally-induced and synergistic embrittlement that incorporate the grain size provide insight into the severity of embrittlement.

Finally, some suggestions for further research will be given here. The present report relies much on SEM metallography and fractography of *one* object, an Egyptian silver vase. This situation should be improved by detailed investigations of other embrittled archaeological silver objects, whereby one must recognise that optical metallography is insufficient and fractography requires considerable interpretive skill. The most suitable objects could be coins. These are less likely to be unique or very rare, particularly if part of a hoard, and they are likely to contain remanent cold-work, which favours observing several forms of embrittlement.

Besides this database broadening there are two important and unresolved mechanistic aspects. These are the definitive identification of the microstructurally-embrittling elements in archaeological silver, and the question whether discontinuous precipitation of copper can occur at ambient temperatures.

Age-embrittlement experiments on silver containing selected impurity elements could be combined with modern diagnostic techniques. These would narrow the interpretive window for microstructurally-induced embrittlement of archaeological silver. However, ageing experiments to detect discontinuous precipitation of copper in silver at ambient or near-ambient temperatures are unfeasible, see Appendix A. In this case interpretive confidence can be improved by SEM examination of a number of embrittled archaeological silver objects for evidence of a direct association between intergranular corrosion and discontinuous precipitation of copper.

ACKNOWLEDGEMENTS

REFERENCES

Ageew, N., Hansen, M., and Sachs, G., 1930, Entmischung und Eigenschaftänderungen übersättigter Silber-Kupferlegierungen, Zeitschrift für Physik, 66, 350-376.

Andrade, E.N. da C., and Henderson, C., 1951, The mechanical behaviour of single crystals of certain face-centered cubic metals, Philosophical Transactions of the Royal Society, A244, 177-203.

Bailey, A.R., 1961, A Text-Book of Metallurgy, Second Edition, MacMillan and Company Ltd, London, U.K.

Baker, H., and Okamoto H. (eds.), 1992, ASM Handbook, Volume 3, Alloy Phase Diagrams, Section 2, ASM International, Materials Park, Ohio, U.S.A.

Baluffi, R.W. (ed.), 1980, Grain Boundary Structure and Kinetics, American Society for Metals (ASM), Metals Park, Ohio, U.S.A.

Barrett, C.S., Kaiser, H.F., and Mehl, R.F., 1935, Studies upon the Widmanstätten structure, VII – The copper-silver system, Transactions of the American Institute of Mining and Metallurgical Engineers, 117, 39-60.

Barrett, C.S., 1952, Structure of Metals, Second Edition, McGraw-Hill Book Company, Inc., New York, New York, U.S.A.

Beckermann, C., and Wang, C.Y., 1994, Incorporating interfacial phenomena in solidification models, Journal of Metals, 46 no. 1, 42-47.

Bennett, A., 1994, Technical examination and conservation, Chapter 2 in The Sevso Treasure Part One, Journal of Roman Archaeology, Supplementary Series Number Twelve.

Bilby, B.A., Cottrell, A.H., and Swinden, K.H., 1963, The spread of plastic yield from a notch, Proceedings of the Royal Society of London A, 272A, 304-314.

Born, H., 1986, Material und Herstellungstechnik der Silberschale des Merenptah, Jahrbuch Preussischer Kulturbesitz, 23, 143-153.

Caley, E.R., 1964, Analysis of Ancient Metals, 36-79, Pergamon Press, Oxford, U.K.

Chadwick, G.A., and Smith, D.A. (eds.), 1976, Grain Boundary Structure and Properties, Academic Press, London, U.K.

Cohen, M., 1937, Aging phenomena in a silver-rich copper alloy, Transactions of the American Institute of Mining and Metallurgical Engineers, 124, 138-157.

Cope, L.H., 1972, The metallurgical analysis of Roman Imperial silver and *aes* coinage, in Methods of Chemical and Metallurgical Investigation of Ancient Coinage (Editors E.T. Hall and D.M. Metcalf), 3-47, Royal Numismatic Society, London, U.K.

Cottrell, A.H., 1952, The formation of immobile dislocations during slip, Philosophical Magazine, 42, 645-647.

Cottrell, A.H., 1953, Dislocations and Plastic Flow in Crystals, First Edition, Oxford University Press, London, U.K.

Cottrell, A.H., 1988, Introduction to the Modern Theory of Metals, 124-126, The Institute of Metals, London, U.K.

Cottrell, A.H., 1989, Strengths of grain boundaries in pure metals, Materials Science and Technology, 5, 1165-1167.

Coxe, C.D., McDonald, A.S., and Sistare, G.H., Jr., 1979, Properties of silver and silver alloys, in Metals Handbook Ninth Edition, Volume 2 Properties and Selection: Nonferrous Alloys and Pure Metals (Editors W.H. Cubberley *et al*.), 671-678, American Society for Metals (ASM), Metals Park, Ohio, U.S.A.

Darken, L.S., and Gurry, R.W., 1953, Physical Chemistry of Metals, 79-90, McGraw-Hill Book Company, New York, New York, U.S.A.

Das, E.S.P., and Marcinkowski, M.J., 1971, Dislocation behaviour at grain boundaries under heterogeneous shear, Materials Science and Engineering, 8, 189-197.

Das, E.S.P., and Marcinkowski, M.J., 1972, Accommodation of the stress field at a grain boundary under heterogeneous shear by initiation of microcracks, Journal of Applied Physics, 43, 4425-4434.

Ercker, L., 1574, Beschreibung allerfürnemisten mineralischen Ertzt und Berckwerksarten: see translation of Second Edition of 1580 by A.G. Sisco and C.S. Smith, 1951, Lazarus Ercker's Treatise on Ores and Assaying, 80-81, 191-198, University of Chicago Press, Chicago, Illinois, U.S.A.

Flanagan, W.F., Bastias, P., and Lichter, B.D., 1991, A theory of transgranular stress-corrosion cracking, Acta Metallurgica et Materialia, 39, 695-705.

Flanagan, W.F., Zhong, L., and Lichter, B.D., 1993, A mechanism for transgranular stress-corrosion cracking, Metallurgical Transactions A, 24A, 553-559.

Fraenkel, W., 1926, Zur Kenntnis der Vorgänge bei der Entmischung übersättigter Mischkristalle, Zeitschrift für Anorganische und Allgemeine Chemie, 154, 386-394.

Frank, F.C., and Read, W.T., Jr., 1950, Multiplication processes for slow moving dislocations, Physical Review, 79, 722-723.

Gale, N.H., and Stos-Gale, Z.A., 1981a, Ancient Egyptian silver, Journal of Egyptian Archaeology, 67, 103-115.

Gale, N.H., and Stos-Gale, Z.A., 1981b, Lead and silver in the ancient Aegean, Scientific American, 244 (6), 142-152.

Gayler, M.L.V., and Carrington, W.E., 1947, Metallographic study of the precipitation of copper from a silver-rich silver-copper alloy, Journal of the Institute of Metals, 73, 625-639.

Gordus, A.A., 1972, Neutron activation analysis of coins and coin-streaks, in Methods of Chemical and Metallurgical Investigation of Ancient Coinage (Editors E.T. Hall and D.M. Metcalf), 127-148, Royal Numismatic Society, London, U.K.

Gordy, W, and Thomas, W.J.O., 1956, Electronegativities of the elements, Journal of Chemical Physics, 24, 439-444.

Gowland, W., 1918, Silver in Roman and earlier times: I. Pre-historic and proto-historic times, Archaeologia, 69, 121-160.

Gschneider, K.A., Jr., 1980, L.S. (Larry) Darken's contributions to the theory of alloy formation and where we are today, in Theory of Alloy Phase Formation (Editor L.H. Bennett), 1-34, The Metallurgical Society of AIME, Warrendale, Pennsylvania, U.S.A.

Gust, W., Predel, B., and Diekstall, K., 1978, Zur diskontinuierlichen Ausscheidung in Silber -6,2 At. % - Kupfer-Dreikristallen, Zeitschrift für Metallkunde, 69, 75-80.

Hall, E.O., 1951, The deformation and ageing of mild steel: III discussion of results, Proceedings of the Physical Society of London, B64, 747-753.

Hecker, S.S., Rohr, D.L., and Stein, D.F., 1978, Brittle fracture in iridium, Metallurgical Transactions A, 9A, 481-488.

Hertzberg, R.W., 1983, Deformation and Fracture Mechanics of Engineering Materials, Second Edition, John Wiley and Sons, New York, U.S.A.

Hondros, E.D., and Seah, M.P., 1977, Segregation to interfaces, International Metallurgical Reviews, 22, 262-301.

Hornbogen, E., 1972, Systematics of the cellular precipitation reactions, Metallurgical Transactions, 3, 2717-2727.

Hultgren, R., Desai, P.D., Hawkins, D.T., Gleiser, M., Kelley, K.K., and Wagman, D.D., 1973, Selected Values of the Thermodynamic Properties of the Elements, American Society for Metals (ASM), Metals Park, Ohio, U.S.A.

Hume-Rothery, W., and Raynor, G.V., 1954, The Structure of Metals and Alloys, Third Edition, 100-108, 126-132, 194-210, The Institute of Metals, London, U.K.

Johnson, W., and Mellor, P.B., 1962, Plasticity for Mechanical Engineers, D. van Nostrand Company Ltd., London, U.K.

Jones, H., 1937, The phase boundaries in binary alloys, part 2: the theory of the α, β phase boundaries, Proceedings of the Physical Society of London, 49, 250-257.

Jones, F.W., Leech, P., and Sykes, C., 1942, Precipitation in single crystals of silver-rich and copper-rich alloys of the silver-copper system, Proceedings of the Royal Society of London, Series A, 181, 154-168.

Kallfass, M., Paul, J., and Jehn, H., 1985, Investigations on the embrittlement of an antique Roman silver bowl, Praktische Metallographie, 22, 317-323.

King, H.W., 1965, Structure of the pure metals, Chapter 2 in Physical Metallurgy (Editor R.W. Cahn), North-Holland Publishing Company, Amsterdam, The Netherlands.

Kuhlmann-Wilsdorf, D., 2001, Q: Dislocations structures – how far from equilibrium? A: Very close indeed, Materials Science and Engineering, A315, 211-216.

La Niece, S., 1983, Niello: an historical and technical survey, Antiquaries Journal, 63, 279-297.

Leo, W., 1967, Elektronenmikroskopische Untersuchungen zur Ausscheidung in aushärtbaren Silber-Kupfer-Legierungen, Zeitschrift für Metallkunde, 58, 456-461.

Li, J.C.M., 1961, High-angle tilt boundary – a dislocation core model, Journal of Applied Physics, 32, 525-541.

Lichter, B.D., Flanagan, W.F., Kim, J.-S., Elkenbracht, J.C., and van Hunen, M., 1996, Mechanistic studies of stress corrosion cracking: application of the corrosion-assisted cleavage model to results using oriented single crystals, Corrosion, 52, 453-463.

Lichter, B.D., Lu, H., and Flanagan, W.F., 2001, Strain-enhanced dissolution: a model for transgranular stress-corrosion cracking, in Proceedings of the 2nd International Conference on Environment Sensitive Cracking and Corrosion Damage (Editors M. Matsumura, H. Nagano, K. Nakasa and Y. Isomoto), 271-278, Nishiki Printing Ltd., Hiroshima, Japan.

Lim, L.C., and Watanabe, T., 1990, Fracture toughness and brittle-ductile transition controlled by grain boundary character distribution (GBCD) in polycrystals, Acta Metallurgica et Materialia, 38, 2507-2516.

Lomer, W.M., 1951, A dislocation reaction in the face-centred cubic lattice, Philosophical Magazine, 42, 1327-1331.

Lucas, A., 1928, Silver in ancient times, Journal of Egyptian Archaeology, 14, 313-319.

MacDowall, D.W., 1972, The Pre-Mohammedan coinage of Greater India: a preliminary list of some analyses, in Methods of Chemical and Metallurgical Investigation of Ancient Coinage (Editors E.T. Hall and D.M. Metcalf), 371-381, Royal Numismatic Society, London, U.K.

Magnin, T., 1996, Advances in Corrosion-Deformation Interactions, Trans Tech Publications, Zurich-Uetikon, Switzerland.

Magnin, T., Chambreuil, A., and Bayle, B., 1996, The corrosion-enhanced plasticity model for stress corrosion cracking in ductile fcc alloys, Acta Materialia, 44, 1457-1470.

Massalski, T.B. 1996, Chapter 3 in Physical Metallurgy, Fourth Edition, Volume I (Editors R.W. Cahn and P. Haasen), Elsevier Science B.V., Amsterdam, The Netherlands.

Massalski, T.B., Murray, J.L., Bennett, L.H., Baker, H., and Kacprzak, L. (eds.), 1986, Binary Alloy Phase Diagrams, Volume 1, 35, 43, 44, 59, 60, 303-305, American Society for Metals (ASM), Metals Park, Ohio, U.S.A.

McKerrell, H., and Stevenson, R.B.K., 1972, Some analyses of Anglo-Saxon and associated Oriental silver coinage, in Methods of Chemical and Metallurgical Investigation of Ancient Coinage (Editors E.T. Hall and D.M. Metcalf), 195-209, Royal Numismatic Society, London, U.K.

McLean, D., 1957, Grain Boundaries in Metals, Oxford University Press, London, U.K.

Metcalf, D.M., 1972, Analyses of the metal contents of Medieval coins, in Methods of Chemical and Metallurgical Investigation of Ancient Coinage (Editors E.T. Hall and D.M. Metcalf), 383-434, Royal Numismatic Society, London, U.K.

Müller, O. and Gentner, W., 1979, On the composition and silver sources of Aeginetan coins form the Asyut hoard, in Proceedings of the 18th International Symposium on Archaeometry and Archaeological Prospection, Rheinland-Verlag, GmbH, 176-193, Cologne, Germany

Murr, L.E., 1975, Interfacial Phenomena in Metals and Alloys, 309-310, Addison-Wesley Publishing Company, Inc., Advanced Book Program, Reading, Massachusetts, U.S.A.

Niemeyer, B., 1997, Early 20th-century restorations and modern conservation treatments on archaeological silver objects, in Metal 95, Proceedings of the International Conference on Metals Conservation (Editors I.D. MacLeod, S.L. Pennec and L. Robbiola), 190-195, James & James (Science Publishers) Ltd, London, U.K.

Norbury, A.L., 1928, The effect of quenching and tempering on the mechanical properties of standard silver, Journal of the Institute of Metals, 39, 145-172.

Northover, J.P., 1999, Personal Communication, Department of Materials, Oxford University, Oxford, U.K.

Oddy, W.A., and Holmes, R., 1992, The Hockwold treasure, in The Art of the Conservator (Editor W.A. Oddy), 137-150, British Museum Press, London, U.K.

Oddy, W.A., and Carroll, S. (eds.), 1999, Reversibility – Does it Exist?, Occasional Paper 135, The British Museum, London, U.K.

Ohr, S.M., 1985, An electron microscope study of crack tip deformation and its impact on the dislocation theory of fracture, Materials Science and Engineering, 72, 1-35.

Organ, R.M., 1977, The current status of the treatment of corroded metal artifacts, in Corrosion and Metal Artifacts, NBS Special Publication 479, National Bureau of Standards / U.S. Department of Commerce, 107-142, Washington, D.C., U.S.A.

Pauling, L., 1945, The Nature of the Chemical Bond, Second Edition, 58-75, Cornell University Press, Ithaca, New York, U.S.A.

Pauling, L., 1947, Atomic radii and interatomic distances in metals, Journal of the American Chemical Society, 69, 542-553.

Pawlowski, A., 1979a, Discontinuous precipitation in deformed FCC solid solution, Scripta METALLURGICA, 13, 785-790.

Pawlowski, A., 1979b, Changes of free energy in the process of discontinuous precipitation in deformed FCC solid solution, Scripta METALLURGICA, 13, 791-794.

Perea, A., and Rovira, S., 1995, The gold from Arrabalde, in Prehistoric Gold in Europe: Mines, Metallurgy and Manufacture (Editors G. Morteani and J.P. Northover), 471-490, Kluwer Academic Publishers, Dordrecht, The Netherlands.

Petch, N.J., 1953, The cleavage strength of polycrystals, Journal of the Iron and Steel Institute, 174, 25-28.

Pettifor, D.G., 1984, A chemical scale for crystal-structure maps, Solid State Communications, 51, 31-34.

Pettifor, D.G., 1988, Structure maps for pseudobinary and ternary phases, Materials Science and Technology, 4, 675-691.

Philip, G., and Rehren, T., 1996, Fourth millenium BC silver from Tell esh-Shuna, Jordan: archaeometallurgical investigation and some thoughts on ceramic skeuomorphs, Oxford Journal of Archaeology, 15, 129-150.

Pourbaix, M., 1963, Section 14.2 in Atlas D'Équilibres Électrochimiques, Gauthier-Villars & Cie, Paris, France.

Predel, B., and Ruge, H., 1968, Untersuchung der Kinetik der diskontinuierlichen Entmischung übersättigter Silber-Mischkristalle, Zeitschrift für Metallkunde, 59, 777-781.

Procter, R.P.M., 1994, Chapter 1.3 in Corrosion, Volume 1, Metal/Environment Reactions, Third Edition (Editors L.L. Shreir, R.A. Jarman and G.T. Burstein), Butterworth-Heinemann Ltd, Oxford, U.K.

Raub, Ch.J., 1995, The metallurgy of gold and silver in prehistoric times, in Prehistoric Gold in Europe: Mines, Metallurgy and Manufacture (Editors G. Morteani and J.P. Northover), 243-259, Kluwer Academic Publishers, Dordrecht, The Netherlands.

Ravich, I.G., 1993, Annealing of brittle archaeological silver: microstructural and technological study, in 10th Triennial Meeting of the International Council of Museums Committee for Conservation, Preprints of the Seminar: August 22/27, 1993, II, 792-795, Washington, D.C., U.S.A.

Reekum, J. van, and Moll, E., 2000, Het lakken van zilverwerk: van gebruiksvoorwerp naar museumobject, in Zeven IJzersterke Verhalen over Metalen (Editors H.A. Ankersmit and J.A. Mosk), 74-79, Instituut Collectie Nederland, Amsterdam, The Netherlands.

Rice, J.R., 1992, Dislocation nucleation from a crack tip: an analysis based on the Peierls concept, Journal of Mechanics and Physics of Solids, 40, 239-271.

Rice, J.R., and Thomson, R., 1974, Ductile versus brittle behaviour of crystals, Philosophical Magazine, 29, 73-97.

Roberts-Austen, W.C., 1888, On certain mechanical properties of metals considered in relation to the Periodic Law, Philosophical Transactions of the Royal Society of London, A179, 339-350.

Rose, R.G., 1957, The precipitation of copper from a silver-5.5 % copper solid solution at 220 °C, Acta Metallurgica, 5, 404-405.

Rosi, F.D., 1954, Stress-strain characteristics and slip-band formation in metal crystals: effect of crystal orientation, Journal of Metals, 6, 1009-1020.

Scharfenberger, W., Schmitt, G., and Borchers, H., 1972, Über die Kinetik der diskontinuierlichen Ausscheidung der Silberlegierung mit 7,5 Gew.-%Cu, Zeitschrift für Metallkunde, 63, 553-560.

Schweizer, F., and Meyers, P., 1978a, Structural changes in ancient silver alloys: the discontinuous precipitation of copper, Paper 78/23/5 in ICOM Committee for Conservation 5th Triennial Meeting, 1978, Zagreb, Yugoslavia.

Schweizer, F., and Meyers, P., 1978b, Authenticity of ancient silver objects: a new approach, MASCA Journal, 1, 9-10.

Schweizer, F., and Meyers, P., 1979, A new approach to the authenticity of ancient silver objects: the discontinuous precipitation of copper from a silver-copper alloy, in Proceedings of the 18th International Symposium on Archaeometry and Archaeological Prospection, Rheinland-Verlag GmbH, 287-298, Cologne, Germany.

Scott, D.A., 1996, Technical study of a ceremonial Sican tumi figurine, Archaeometry, 38, 305-311.

Scully, J.C., 1971, Fractographic aspects of stress corrosion cracking, in The Theory of Stress Corrosion Cracking in Alloys (Editor J.C. Scully), 127-166, North Atlantic Treaty Organization Scientific Affairs Division, Brussels, Belgium.

Seah, M.P., 1980a, Adsorption-induced interface decohesion, Acta Metallurgica, 28, 955-962.

Seah, M.P., 1980b, Chemistry of solid - solid interfaces – A review of its characterization, theory, and relevance to materials science, Journal of Vacuum Science and Technology, 17, 16-24.

Shewmon, P.G., 1998, Grain boundary cracking, Metallurgical and Materials Transactions A, 29A, 1535-1544.

Smallman, R.E., 1963, Modern Physical Metallurgy, Second Edition, 170, Butterworths, London, U.K.

Smith, C.S., 1965, The interpretation of microstructures of metallic artifacts, in Application of Science in Examination of Works of Art (Editor W.J. Young), 20-52, Boston Museum of Fine Arts, Boston, Massachusetts, U.S.A.

Smith, E., and Barnby, J.T., 1967, Crack nucleation in crystalline solids, Metal Science Journal, 1, 56-64.

Smithells, C.J., 1967, Metals Reference Book, Volume 3, Fourth Edition, 708, 709, Butterworths, London, U.K.

Stroh, A.N., 1954, The formation of cracks as a result of plastic flow, Proceedings of the Royal Society of London, Series A, 223, 404-414.

Stroh, A.N., 1957, A theory of the fracture of metals, Advances in Physics, 6, 418-465.

Tada, H., Paris, P.C., and Irwin, G.R., 1973, The Stress Analysis of Cracks Handbook, 14.5, Del Research Corporation, St. Louis, Missouri, U.S.A.

Taira, S., Tanaka, K., and Nakai, Y., 1978, A model of crack tip slip band blocked by grain boundary, Mechanics Research Communications, 5, 375-381.

Tanaka, K., Akiniwa, Y., Nakai, Y., and Wei, R.P., 1986, Modelling of small fatigue crack growth interacting with grain boundary, Engineering Fracture Mechanics, 24, 803-819.

Tanaka, K., and Akiniwa, Y., 1999, Mechanics of small fatigue crack propagation, in Small Fatigue Cracks: Mechanics, Mechanisms and Applications (Editors K.S. Ravichandran, R.O. Ritchie and Y. Murakami), 59-71, Elsevier Science Ltd., Oxford, U.K.

Teatum, E.T., Gschneider, K.A., Jr., and Waber, J.T., 1968, Compilation of calculated data useful in predicting metallurgical behavior of the elements in binary alloy systems, Los Alamos Scientific Laboratory Report LA-4003, Clearing House for Federal Scientific and Technical Information, Springfield, Virginia, U.S.A.

Thompson, A.W., and Knott, J.F., 1993, Micromechanisms of brittle fracture, Metallurgical Transactions A, 24A, 523-534.

Thompson, F.C., and Chatterjee, A.K., 1954, The age-embrittlement of silver coins, Studies in Conservation, 1, 115-126.

Tylecote, R.F., 1986, The Prehistory of Metallurgy in the British Isles, 3-4, 54-61, The Institute of Metals, London, U.K.

Tylecote, R.F., 1987, The Early History of Metallurgy in Europe, 69-80, 138-140, 280-290, Longman Inc., New York, New York, U.S.A.

Tylecote, R.F., 1992, A History of Metallurgy, Second Edition, 71, The Institute of Materials, London, U.K.

Waber, J.T., Gschneider, K.A., Jr., Larson, A.C., and Prince, M.Y., 1963, Prediction of solid solubility in metallic alloys, Transactions of the Metallurgical Society of AIME, 227, 717-723.

Wanhill, R.J.H., 2000a, Brittle archaeological silver. Identification, restoration and conservation, Materialen, 16, 30-35: also NLR Technical Publication NLR TP 97647 L, National Aerospace Laboratory NLR, Amsterdam, The Netherlands.

Wanhill, R.J.H., 2000b, Microstructural embrittlement of gold and silver, NLR Technical Publication NLR-TP-2000-358, National Aerospace Laboratory NLR, Amsterdam, The Netherlands.

Wanhill, R.J.H., 2001, Microstructurally-induced embrittlement of archaeological silver, NLR Technical Publication NLR-TP-2001-032, National Aerospace Laboratory NLR, Amsterdam, The Netherlands.

Wanhill, R.J.H., Steijaert, J.P.H.M., Leenheer, R., and Koens, J.F.W., 1998, Damage assessment and preservation of an Egyptian silver vase (300-200 BC), Archaeometry, 40, 123-137: also NLR Technical Publication NLR TP 95372 L, National Aerospace Laboratory NLR, Amsterdam, The Netherlands.

Watanabe, T., 1984, An approach to grain boundary design for strong and ductile polycrystals, Res Mechanica, 11, 47-84.

Watanabe, T., 1993, Grain boundary design and control for high temperature materials, Materials Science and Engineering, A166, 11-28.

Watanabe, T., 1994, The impact of grain boundary character distribution on fracture in polycrystals, Materials Science and Engineering, A176, 39-49.

Watanabe, T., Fujii, H., Oikawa, H., and Arai, K.I., 1989, Grain boundaries in rapidly solidified and annealed Fe-6.5 mass % Si polycrystalline ribbons with high ductility, Acta Metallurgica, 37, 941-952.

Watanabe, T., Kitamura, S., and Karashima, S., 1980, Grain boundary hardening and segregation in alpha iron-tin alloy, Acta Metallurgica, 28, 455-463.

Werner, A.E., 1965, Two problems in the conservation of antiquities: corroded lead and brittle silver, in Application of Science in Examination of Works of Art (Editor W.J. Young), 96-104, Boston Museum of Fine Arts, Boston, Massachusetts, U.S.A.

Wood, R., 2000, To protect and preserve, Materials World, 8, 30-32.

Table 1   Selected metallic and semi-metallic element properties

ELEMENT	ATOMIC NUMBER	EMPIRICAL ORDERING NUMBER	ATOMIC DIAMETER (nm)	PAULING ATOMIC DIAMETER, C.N.12 (nm)	ALLOYING ELEMENT PRIMARY SOLID SOLUBILITY LIMIT IN SILVER wt.%	at.%	ELECTRO-NEGATIVITY $(eV)^{1/2}$	NUMBER OF VALENCE ELECTRONS	SUBLIMATION ENTHALPY (J/m^2)
Li	3	12	0.3456	0.3098	9.1	60.9	0.95	1	3.37
Na	11	11	0.4226	0.3792	0	0	0.95	1	1.53
Al	13	80	0.3164	0.2858	6.1	20.6	1.52	3	8.34
K	19	10	0.5236	0.4698	0	0	0.83	1	0.84
Mn	25	60	0.2856	0.2522;0.2612	31	47	2.24;1.92	7;5	8.83
Cu	29	72	0.2826	0.2552	8.8	14.1	1.82	1	10.7
Zn	30	76	0.3076	0.2758	29.0	40.3	1.66	2	3.50
Ga	31	81	0.3344	0.2816	12.0	17.4	1.80	3	6.19
Ge	32	84	0.3510	0.2732	6.7	9.6	1.90	4	7.70
As	33	89	0.3452	0.2780	5.5	7.7	2.08	5	6.46
Se	34	93	0.3726	0.280	0	0	2.46	6	3.79
Rb	37	9	0.5600	0.4960	0	0	0.83	1	0.67
Rh	45	65	0.2974	0.2684	0	0	2.20	9	15.9
Pd	46	69	0.3042	0.2746	100	100	2.21	10	10.4
Ag	47	71	0.3196	0.2884	100	100	1.68	1	7.09
Cd	48	75	0.3452	0.3086	43.2	42.2	1.58	2	2.40
In	49	79	0.3682	0.3320	22.1	21.1	1.82	3	4.58
Sn	50	83	0.3724	0.3084;0.3240	12.5	11.5	1.83;1.65	4;2	5.55
Sb	51	88	0.3864	0.3180	8.1	7.2	1.98	5	4.52
Te	52	92	0.4010	0.320	0	0	1.92	6	3.12
Au	79	70	0.3188	0.2878	100	100	1.90	1	9.25
Tl	81	78	0.3784	0.3424	13.8	7.8	1.86	3	3.24
Pb	82	82	0.3898	0.3492	5.2	2.8	1.93	4	3.29
Bi	83	87	0.4072	0.340	4.9	2.6	1.86	5	3.23

(1) Empirical ordering number acknowledges chemical similarity of elements from the same Group of the Periodic Table (Pettifor 1988).
(2) Atomic diameters from King (1965) and Pauling (1947). The latter depend on the number of nearest neighbour atoms (coordination number, C.N.) for each atom in solid solution in the matrix. C.N.=12 for atoms in solid solution in silver.
(3) Primary solid solubility limits from Baker et al. (1992) and Massalski et al. (1986).
(4) Electronegativities and number of valence electrons from Teatum et al. (1968).
(5) Sublimation enthalpies (per unit area) according to Seah (1980a) using Hultgren et al. (1973).

Table 2 Silver binary alloys with alloying element low primary solid solubility: PSSL = Primary Solid Solubility Limit; max = maximum; eut = eutectic temperature; amb = ambient temperatures. Data (phase diagrams) from Baker et al. (1992), see Appendix C, and Thompson and Chatterjee (1954)

2.1 Zero or very low PSSL

BINARY ALLOY SYSTEMS	DILUTE ALLOY PHASE DIAGRAM CHARACTERISTICS	EQUILIBRIUM PHASES AT AMBIENT TEMPERATURES	
		PRIMARY CRYSTALS/GRAINS	BETWEEN PRIMARY CRYSTALS/GRAINS
Ag-K	phase diagram not available (Massalski et al. 1986)	Ag	
Ag-Na	Ag-Ag$_2$Na peritectic, 322°C ?; Ag-Na eutectic, > 99.9 at.% Na, 97.7°C	Ag	Na or possibly Ag$_2$Na
Ag-Rb	phase diagram not available (Massalski et al. 1986)	Ag	
Ag-Se	monotectic, 890°C; Ag-Ag$_2$Se eutectic, 12.1 at.% Se, 840°C	Ag	eutectic Ag+Ag$_2$Se
Ag-Te	Ag-Ag$_2$Te eutectic, 11.5 at.% Te, 869°C	Ag	eutectic Ag+Ag$_2$Te

2.2 PSSL$_{max}$ at eutectic or peritectic temperatures

BINARY ALLOY SYSTEMS	DILUTE ALLOY PHASE DIAGRAM CHARACTERISTICS	ALLOYING ELEMENT		EQUILIBRIUM PHASES AT AMBIENT TEMPERATURES		
		PSSL$_{max}$ (at.%)	PSSL$_{amb}$ (at.%)	PRIMARY CRYSTALS/GRAINS		BETWEEN PRIMARY CRYSTALS/GRAINS
				ALLOYS BELOW PSSL$_{amb}$	ALLOYS ABOVE PSSL$_{amb}$	ALLOYS ABOVE PSSL$_{max}$
Ag-As	α-ζ peritectic (up to 10.1 at.% As), 582°C; eutectoid, 446°C	7.7	~2?	α	α→α+As	eutectoid α+As
Ag-Ge	α-Ge eutectic, 24.2 at.% Ge, 651°C	9.6	~0	α	α→Ag+Ge	Ag+Ge from eutectic α+Ge
Ag-Sb	α-ζ peritectic (up to 8.8 at.% Sb), 702.5°C	7.2	~4	α	α→α+ζ	ζ (intermediate phase)
Ag-Sn	α-ζ peritectic (up to 12.9 at.% Sn), 724°C	11.5	~9	α	α→α+ζ	ζ (intermediate phase)

2.3 PSSL$_{max}$ > PSSL$_{eut}$

BINARY ALLOY SYSTEMS	DILUTE ALLOY PHASE DIAGRAM CHARACTERISTICS	ALLOYING ELEMENT			EQUILIBRIUM PHASES AT AMBIENT TEMPERATURES		
		PSSL$_{max}$ (at.%)	PSSL$_{eut}$ (at.%)	PSSL$_{amb}$ (at.%)	PRIMARY CRYSTALS/GRAINS		BETWEEN PRIMARY CRYSTALS/GRAINS
					ALLOYS BELOW PSSL$_{amb}$	ALLOYS ABOVE PSSL$_{amb}$	ALLOYS ABOVE PSSL$_{eut}$
Ag-Bi	α-Bi eutectic, 95.3 at.% Bi, 262.5°C	2.6	0.83	~0	α	α→Ag+Bi	Ag+Bi from eutectic α+Bi
Ag-Pb	α-Pb eutectic, 95.5 at.% Pb, 304°C	2.8	0.79	<0.05	α	α→α+Pb	α+Pb from eutectic α+Pb
Ag-Tl	α-Tl eutectic, 97.4 at.% Tl, 291°C	7.8	5.1	?	α	α→α+Tl	α+Tl from eutectic α+Tl

Table 3   Diagnostic techniques for archaeological silver embrittlement

VISUAL INSPECTION (×1-×10) (UNAIDED EYE AND HAND LENS)	X-RAY RADIOGRAPHY (×1) (LIMITED ENLARGEMENT)	OPTICAL (×10-×1000) AND SEM (×10-×30,000) METALLOGRAPHY, EDX OR WDX, AND MICROHARDNESS TESTING (HV)	SEM FRACTOGRAPHY (×10-×30,000)
Purpose: Object Basic Condition	Purpose: "Hidden" Damage	Purpose: Manufactured Condition, Chemical Analysis, Internal Damage and Embrittlement	Purpose: Embrittlement Types

• nominally intact
 	
• restored
  • macrocrack patterns
  • missing pieces
 	
• fragmented
  • macrocrack patterns
  • missing pieces
	• nominally intact, restored, or fragmented
	  • hairline cracks
	  • macrocracks
	  • cracks following indented decorations
	
	• restored
	• missing pieces
		• manufactured condition
		  • mechanically worked } grain size, segregation bands, slip lines
		  • mechanically worked and annealed } deformation and annealing twins
		  • as-cast (dendritic) } coring, eutectic distribution
		  • cast and annealed
		
		• chemical analysis (SEM + EDX or WDX)
		  • source: lead cupellation, native silver or aurian silver
		  • lead , bismuth, antimony, tin, arsenic and thallium contents: linked to microstructurally-induced embrittlement
		  • copper content
		    - high purity (low copper) may be linked to retained cold-work
		    - intentional additions of copper for strength
		    - long-term discontinuous precipitation along grain boundaries
		
		• corrosion-induced embrittlement
		  • surficial
		  • wide intergranular cracks: linked to discontinuous precipitation of copper
		  • interdendritic
		  • corrosion along segregation bands, slip lines, deformation twin boundaries and in slip-line fields below indented decorations: severe corrosion leads to cracks
		
		• microstructurally-induced embrittlement
		  • narrow intergranular cracks
		  • bodily displaced grains
		
		• microhardness testing (HV)
		  • annealed } HV values also depend on chemistry, especially copper content
		  • retained cold-work
		  • corrosion } HV values and possible nucleation of new cracks
		  • microstructural embrittlement
			• corrosion-induced embrittlement
			  • surficial corrosion
			  • corroded fracture surfaces with fine granular appearance like surficial corrosion
			  • transgranular fracture (crystallographic) along slip bands and deformation twin boundaries, possibly also along annealing twin boundaries
			
			• microstructural embrittlement
			  • mainly clean grain boundary facets: can show local corrosion where slip lines, deformation twins and segregation bands intersect the fracture surfaces
			  • narrow intergranular cracks
			  • bodily displaced grains

SEM = Scanning Electron Microscopy; EDX = Energy Dispersive X-ray fluorescence; WDX = Wavelength Dispersive X-ray fluorescence

Table 4 Possible remedial measures for embrittled archaeological silver

OBJECT BASIC CONDITION		TYPE OF EMBRITTLEMENT	TECHNICALLY POSSIBLE REMEDIES	POTENTIALLY SANCTIONABLE REMEDIES
Nominally Intact	undeformed	• corrosion-induced; synergistic	• A	• A
		• microstructurally-induced	• B	• none
	deformed	• corrosion-induced; synergistic	• A • C	• A • B: coins
		• microstructurally-induced	• B	• C: coins
Restored	old restoration	• corrosion-induced	• A • disassembly + reassembly + A • disassembly + C + reassembly	• A • none
		• microstructurally-induced	• disassembly + B + reassembly	• A
		• synergistic	• A	• disassembly + reassembly + A
	modern restoration	• corrosion-induced; synergistic	• A	• A
		• microstructurally-induced	• disassembly + B + reassembly	• none
Fragmented		• corrosion-induced; synergistic	• C + assembly • assembly + A	• C + assembly • assembly + A
		• microstructurally-induced	• B + assembly	• B + assembly

NOTES

A   Restore original surface finish, if necessary. Clean and rinse successively in demineralised water and ethanol. Outgas *in vacuo* ($<10^{-4}$ Pa) and place in desiccator to await coating. Apply a colourless transparent organic coating, e.g. an acrylic resin, aliphatic polyurethane or cellulose nitrate "Frigilene" (Wanhill *et al.* 1998; van Reekum and Moll 2000). Probably the best option would be a "Parylene" coating, deposited by vapour condensation under a reduced pressure of 15 Pa (Wood 2000).

B   Heat in an inert environment (e.g. argon or nitrogen) for 0.5-1 hour at 500 °C, cool in a forced air draught. This is based on data and suggestions of Thompson and Chatterjee (1954) for silver containing copper as well as lead. The heat-treatment's efficacy may be checked by microhardness testing (no new cracks).

C   Heat in an inert environment or under charcoal for 5-10 minutes at 700 °C, cool in a forced air draught. This is based on Ravich (1993). Prior heating in flowing hydrogen for 0.5 hour at 300-400 °C could be beneficial (Werner 1965), presumably because some of the intergranular corrosion products – notably silver chloride – are converted back to metal.
The heat-treatment temperature of 700 °C is probably close to the minimum, see Ravich (1993). Higher temperatures may have to be considered. This is very problematical: successful experiments have been done at temperatures up to 900 °C (Werner 1965; Ravich 1993), but silver containing several wt. % copper may undergo incipient melting above 800 °C (Norbury 1928).

D.   Coins   :   These are relatively small and therefore easier to heat-treat, even by hand.

E.   Old restorations   :   Disassembly and reassembly may be feasible and required. Reassemble with modern non-hygroscopic adhesives and fillers (Niemeyer 1997).

F.   Composite objects   :   B and C assume artifacts do not have soldered joints or niello inlay or gilding. Soft solders (lead-tin) begin melting above 183 °C (Bailey 1961, 513) and will also dissolve the silver if overheated (Niemeyer 1997). Hard solders (silver-copper) begin melting above 779 °C (Smithells 1967, 379). Roman silver sulphide niello should not be heated much above 600 °C, and later silver-copper and silver-copper-lead sulphide niellos melt at about 680 °C and 440 °C respectively (La Niece 1983, Bennett 1994). Gilding is easily ruined by (over)heating: gold layers are so thin, ~10 μm, they soon diffuse into the silver substrate.

D388-01N

General (surficial) corrosion
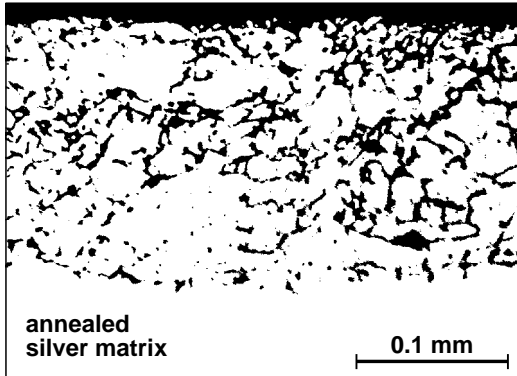
Metallograph (Bennett 1994)
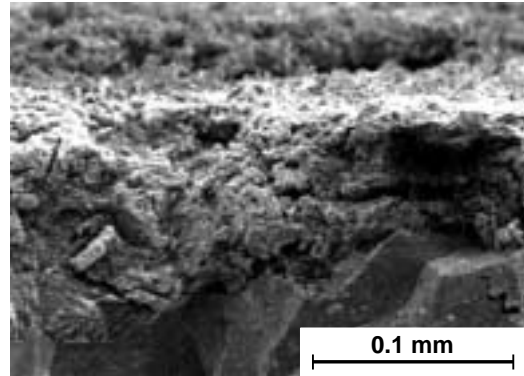
SEM fractograph (Wanhill *et al.* 1995)

Intergranular or interdendritic corrosion
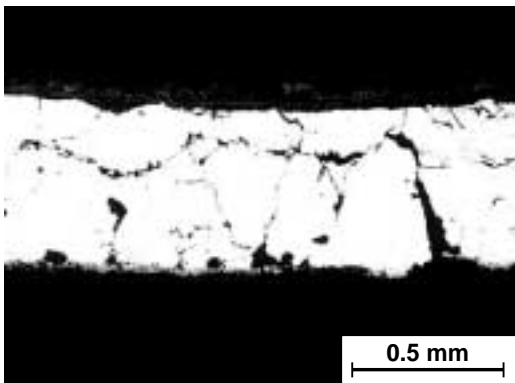
Intergranular: metallograph (Werner 1965)
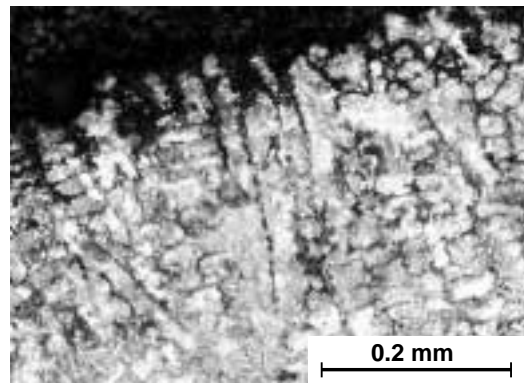
Interdendritic: metallograph (Scott 1996)

Slip line, deformation twin boundary and segregation band corrosion
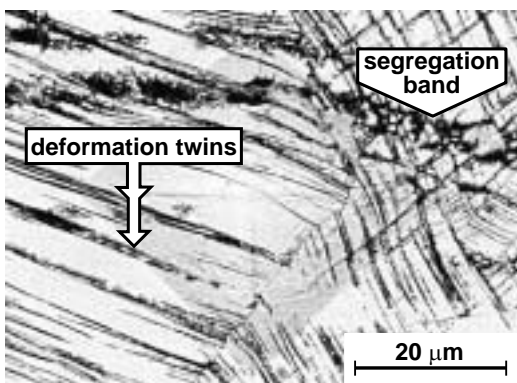
Corrosion along slip lines, deformation twins and
segregation bands: SEM metallograph
(Wanhill *et al.* 1998)
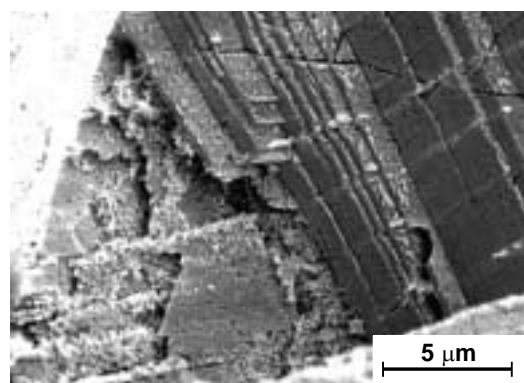
Crystallographic fracture owing to corrosion along slip
lines and deformation twins: SEM fractograph
(Wanhill *et al.* 1998)

Fig. 1   *Types of corrosion of high silver content archaeological silver: SEM = Scanning Electron
Microscopy*

D388-01N
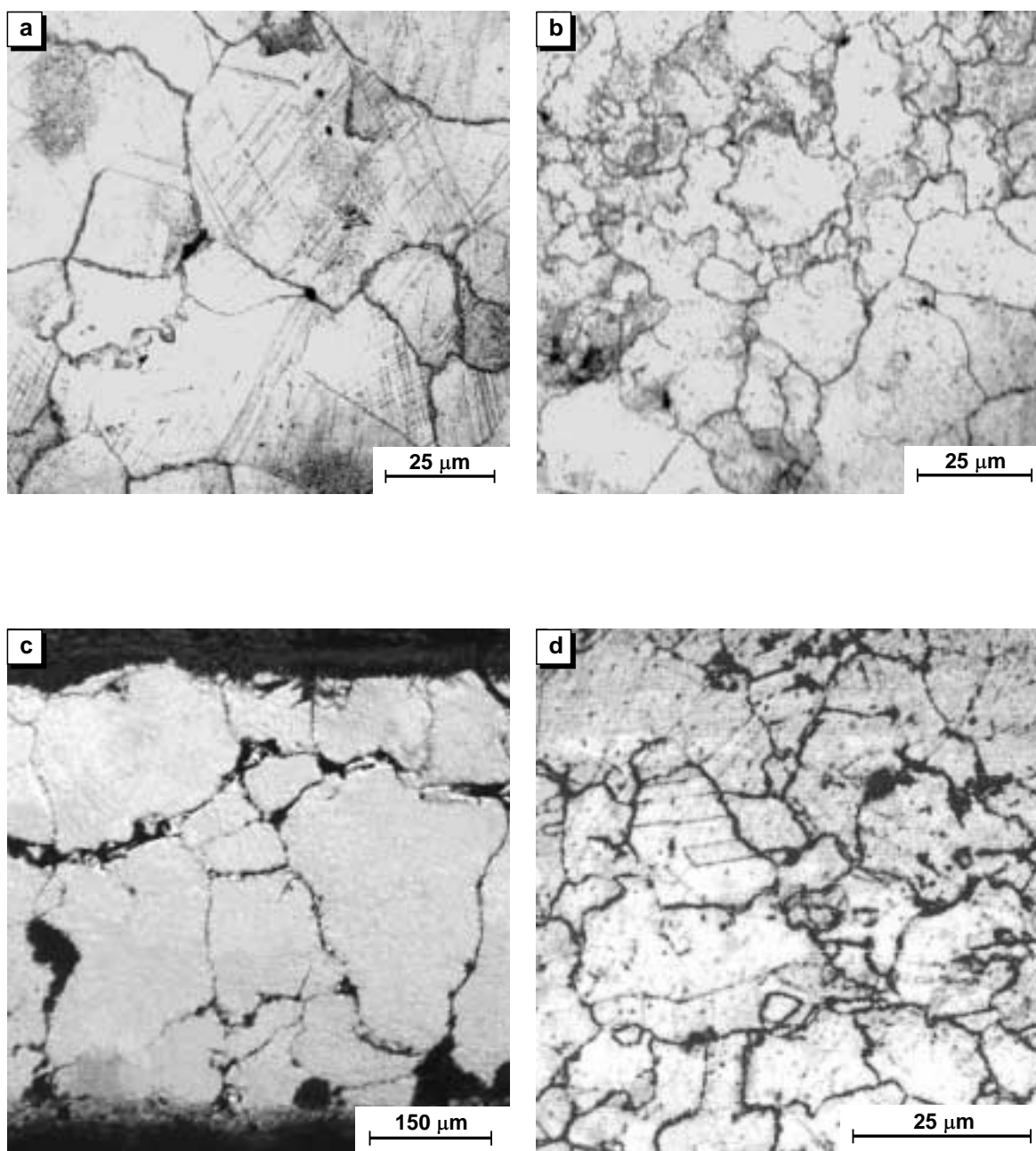
Fig. 2   Meandering grain boundaries (M), grain boundary precipitation (P) and intergranular
          corrosion (C) in archaeological silver:
          (a)   Gundestrup cauldron sheet, 100 BC: M + P; remanent cold-work visible as slip lines
          (b)   Byzantine paten, c. 12th century AD: M + P(?)
          (c)   Roman cup, c. 50 BC – 50 AD: M (slight) + P + C (Werner 1965)
          (d)   Hellenistic silver dish: M (Schweizer and Meyers 1979)

          The metallographs in (a) and (b) are courtesy of J.P. Northover, Oxford University,
          Oxford, U.K.

D388-01N

mushy

solid

liquid

increasing solute
content of liquid
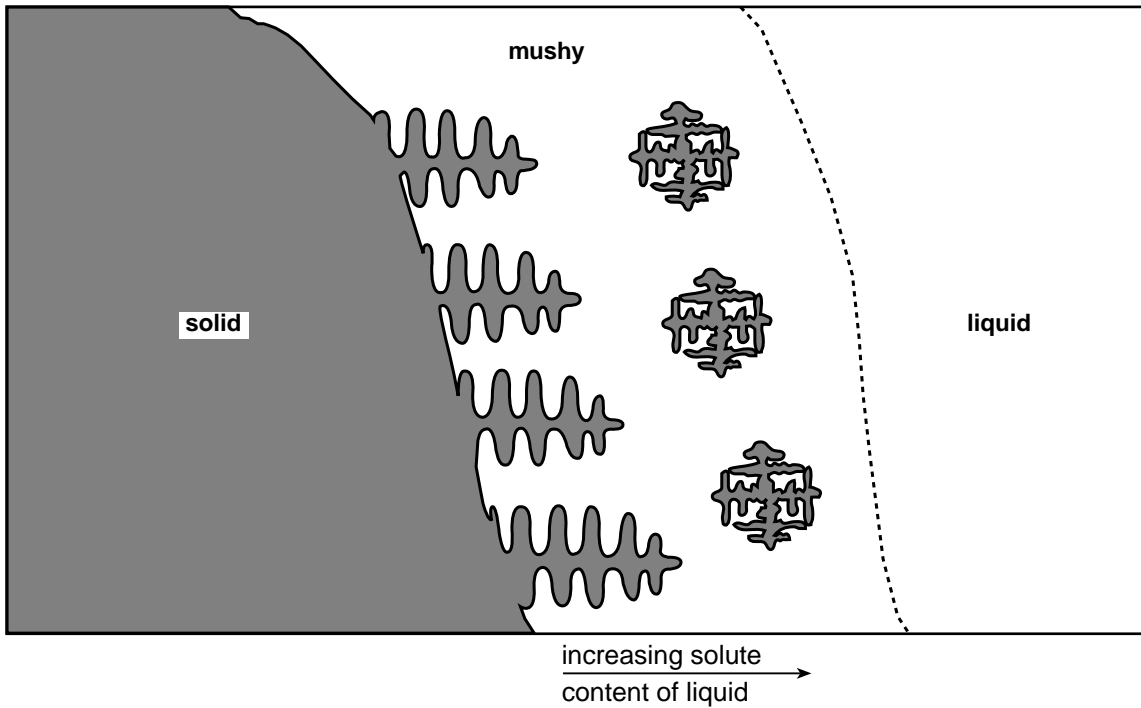
a   Schematic of alloy solidification by dendrite formation, proceeding from left to right in the diagram.
After Beckermann and Wang (1994)
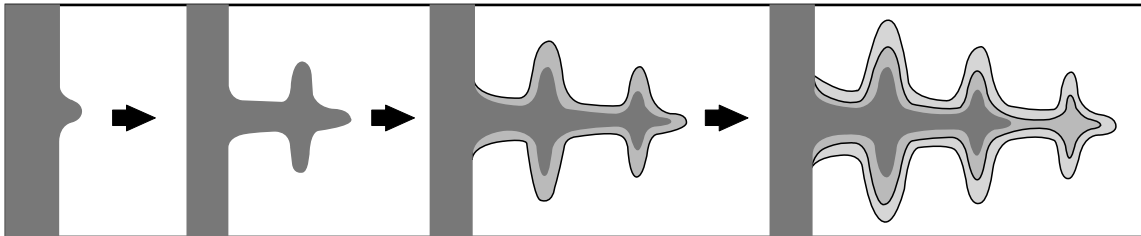
b   Schematic of dendritic segregation (coring) during dendrite formation

Notes

(1)   Alloys generally solidify over a *range* of temperature
(2)   For high silver content alloys the first part to solidify is richer in silver, and the melt becomes
enriched in the solute elements, including copper
(3)   Progressive cooling *under non-equilibrium conditions* (the usual rapid cooling of cast metal)
results in
     - dendrites varying in composition between their centres and surfaces (coring)
     - the finally solidifying interdendritic liquid being rich in solute elements

Fig. 3   *Schematics for explaining dendritic segregation (coring) and interdendritic segregation*

D388-01N

as-cast

Ambient temperature mechanical working

cold-worked

Annealing

Multiple cycles if necessary for
sufficient forming and shaping

recrystallized

Prolonged annealing

grain growth
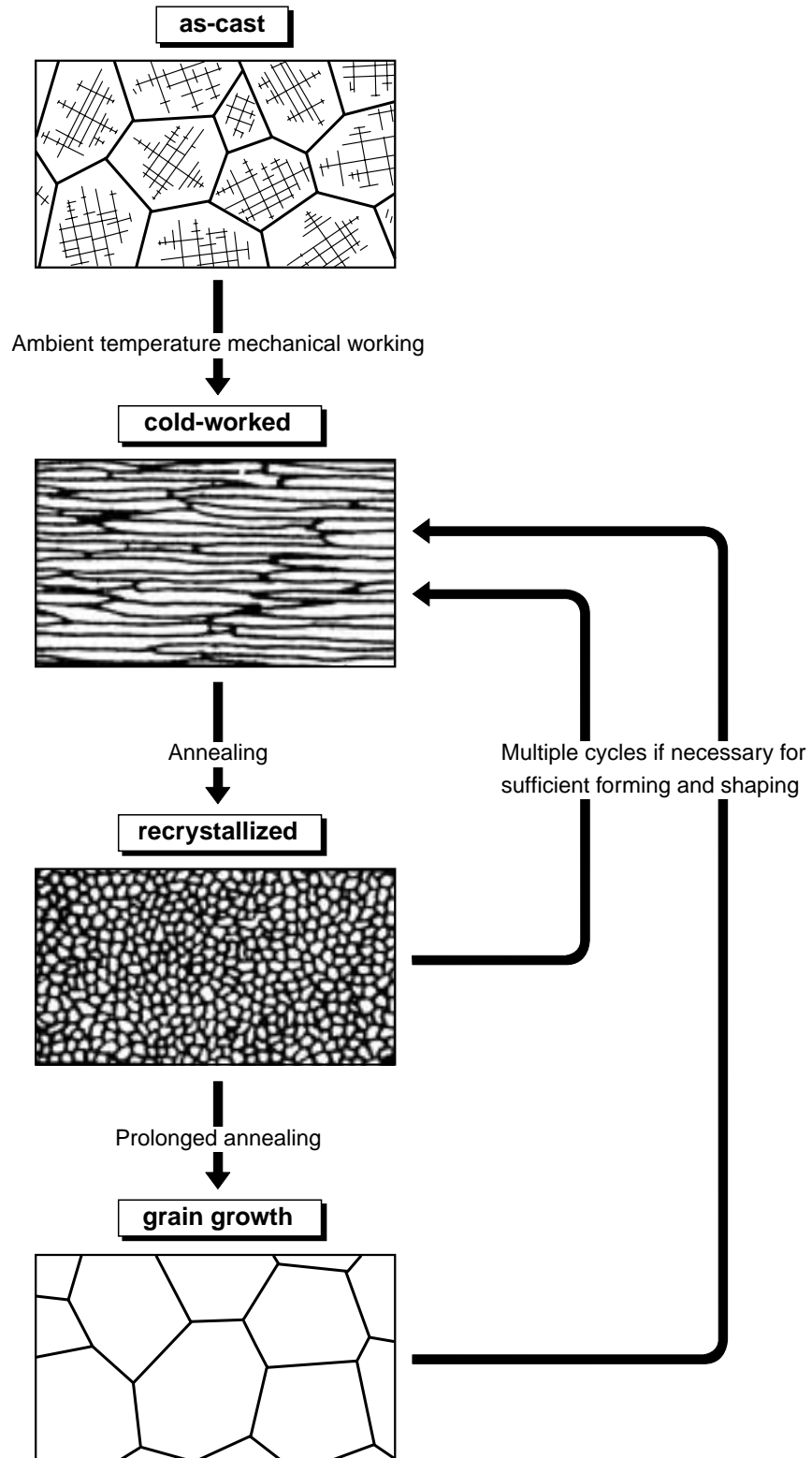
Fig. 4   Schematic relationships between as-cast, cold-worked and annealed
microstructures for a single-phase alloy. These are relevant to the
fabrication of archaeological silver objects which, however, are not
always annealed after cold-work, e.g. struck coins

D388-01N
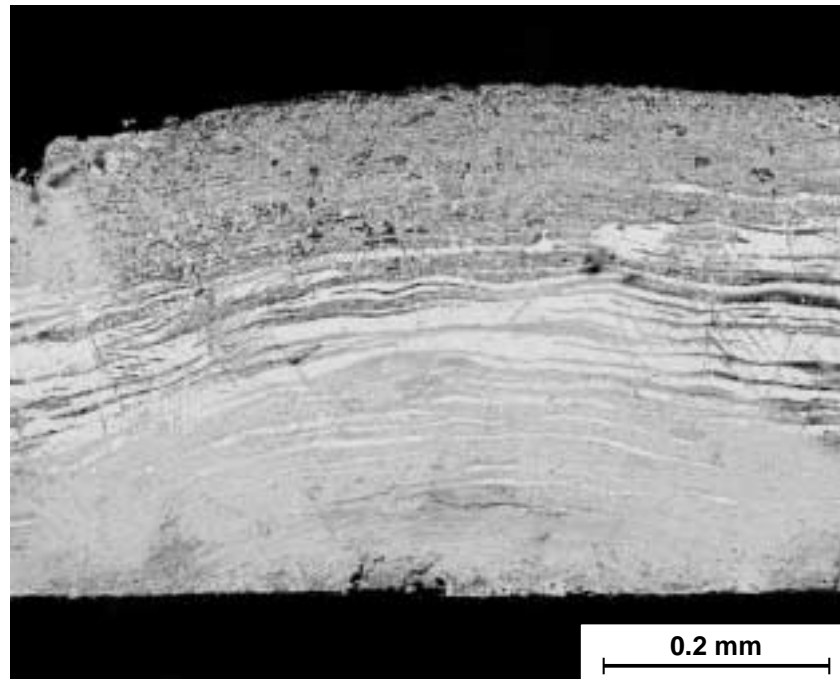
*Fig. 5   Segregation bands visible via SEM backscattered electron
imaging of a metallographic cross-section of the wall of an
Egyptian silver vase (Wanhill et al. 1998)*
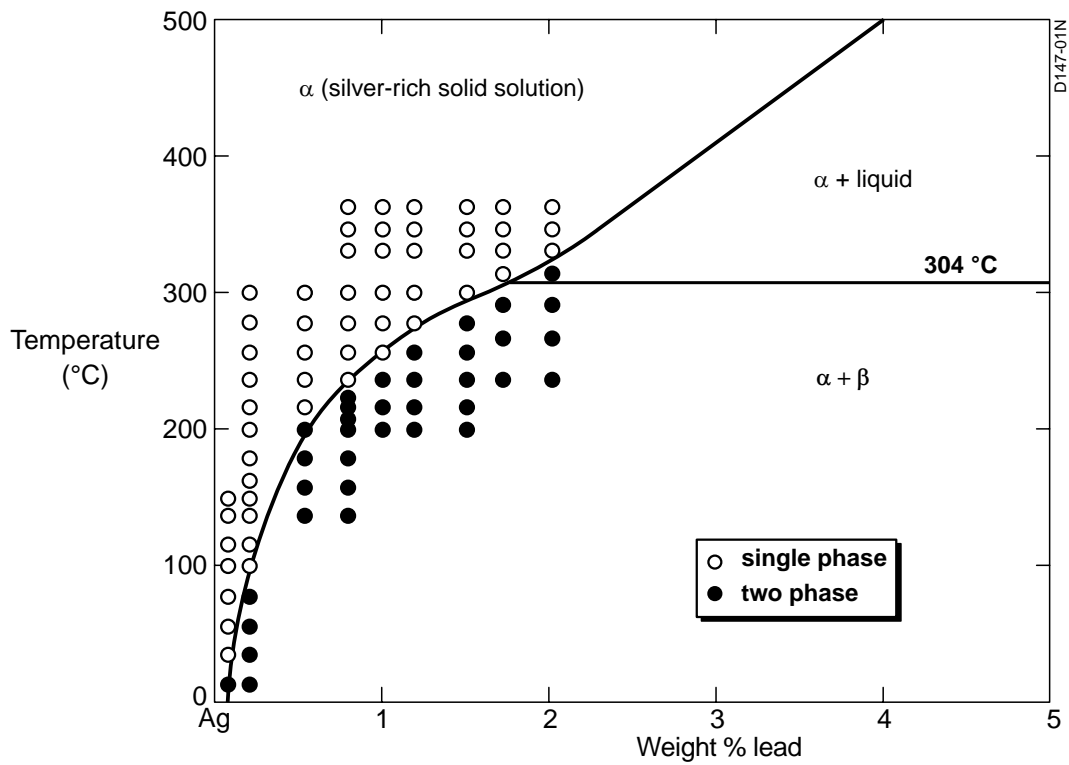
*Fig. 6   Silver-rich low temperature region of the Ag-Pb equilibrium phase diagram,
determined by ageing supersaturated solid solutions at the indicated temperatures
(Thompson and Chatterjee 1954)*

D388-01N
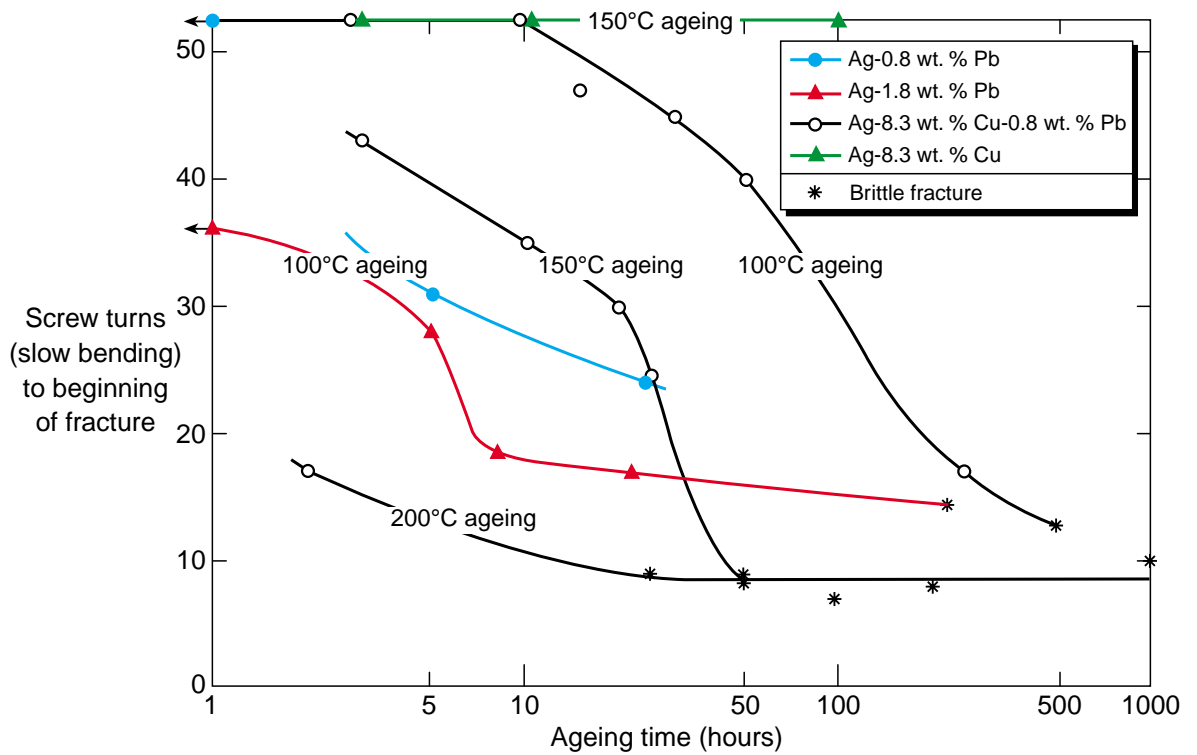
Fig. 7 Age-embrittlement of cast, solution treated and aged Ag-Pb and Ag-Cu-Pb alloys.
Also ageing of Ag-8.3 wt. % Cu. Data from Thompson and Chatterjee (1954)
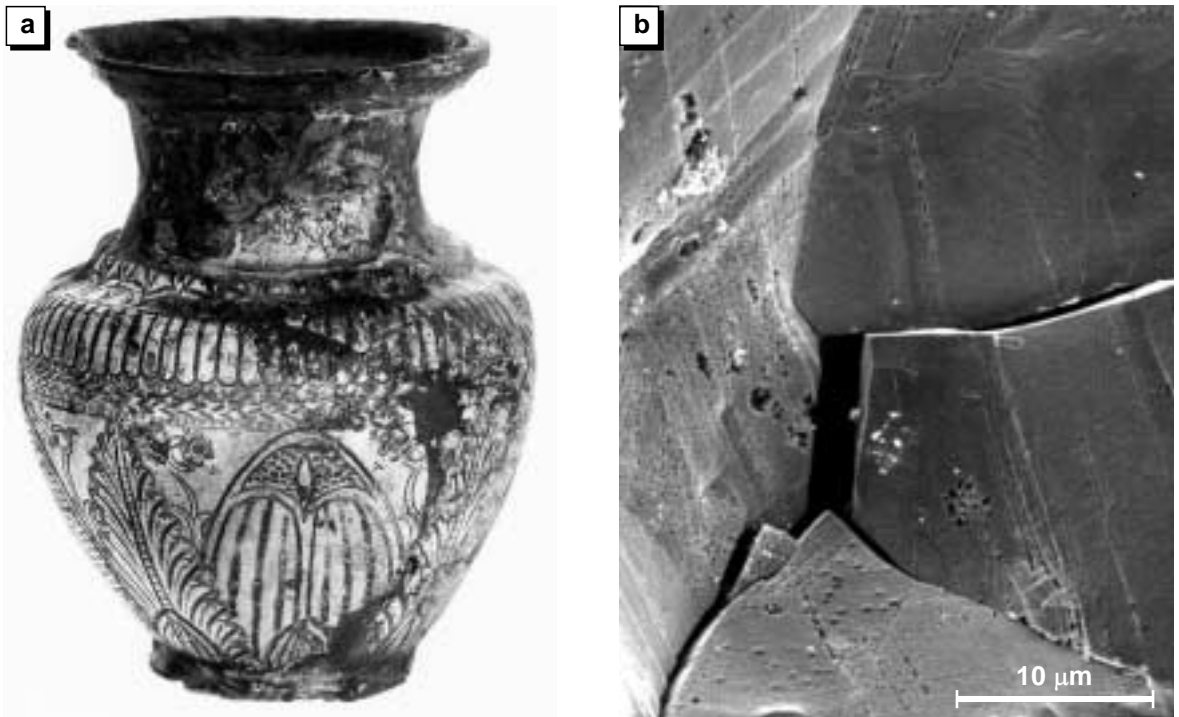
Fig. 8 Brittle grain boundary fracture in a sample from an Egyptian silver vase (Wanhill et al. 1998):
figure 8b is a SEM fractograph

D388-01N
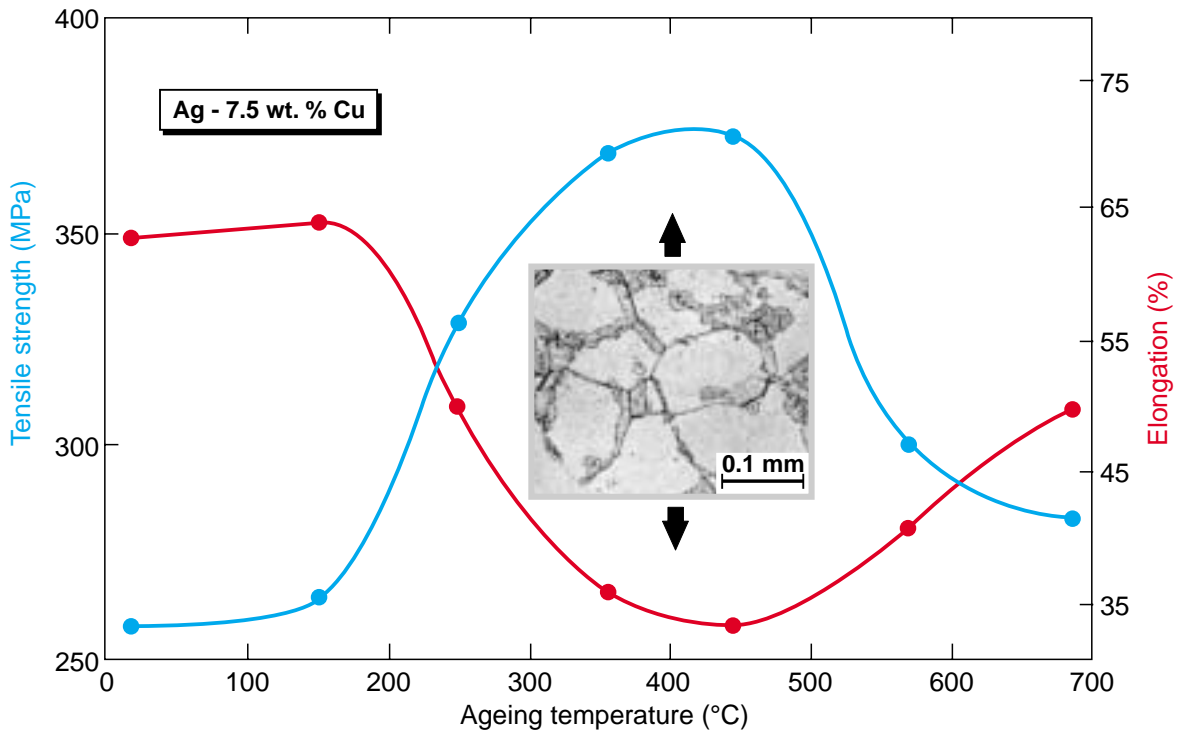
Fig. 9   Effect of 30 minutes ageing on the mechanical properties of 720°C solutionised and
quenched standard silver, Ag-7.5 wt. % Cu (Norbury 1928): the metallograph illustrates the
approximate amount of discontinuous precipitation at the maximum tensile strength and
minimum elongation
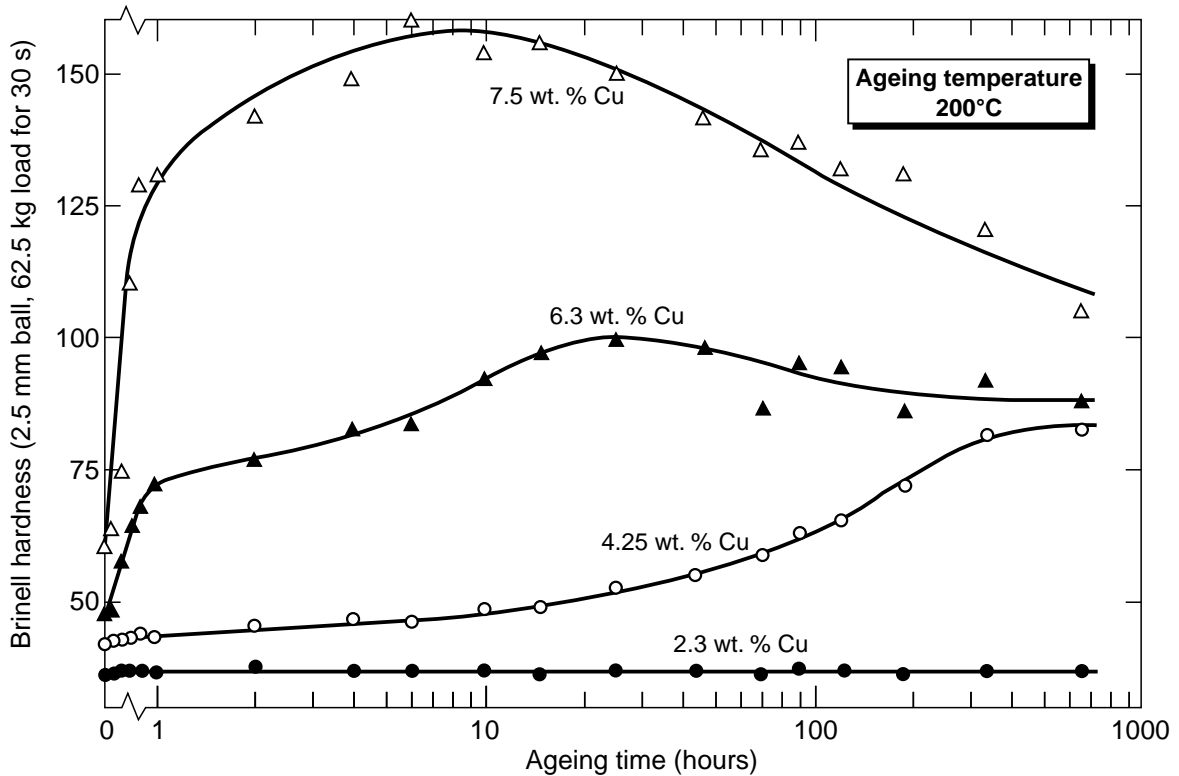
Fig. 10   Effect of 200°C ageing on the hardness of solutionised and quenched silver-copper alloys
(Ageew et al. 1930)

D388-01N
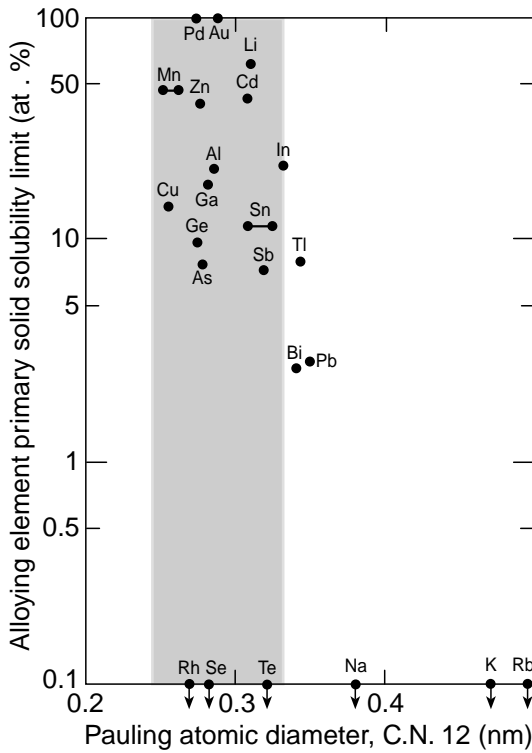
Fig. 11 The size-factor rule for solid solutions in silver. The shaded region shows the range of favourable size-factor, bounded by the limits ±15% of the atomic diameter of silver. Data from table 1
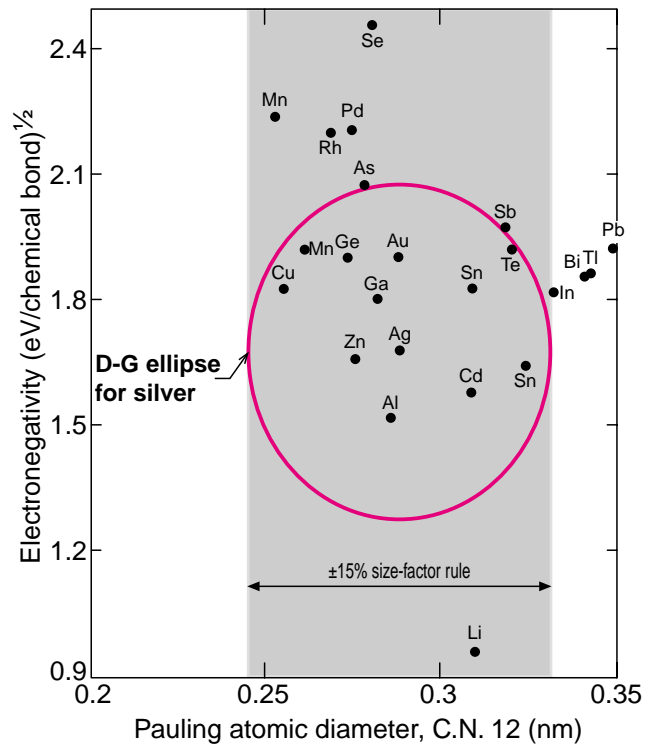
Fig. 12 Darken-Gurry (D-G) map for solid solutions in silver. Solute elements within the ellipse boundary, minor axes ±0.4 (eV)$^{1/2}$, are predicted to have solid solubilities greater than 5-10 at . % . Data from table 1
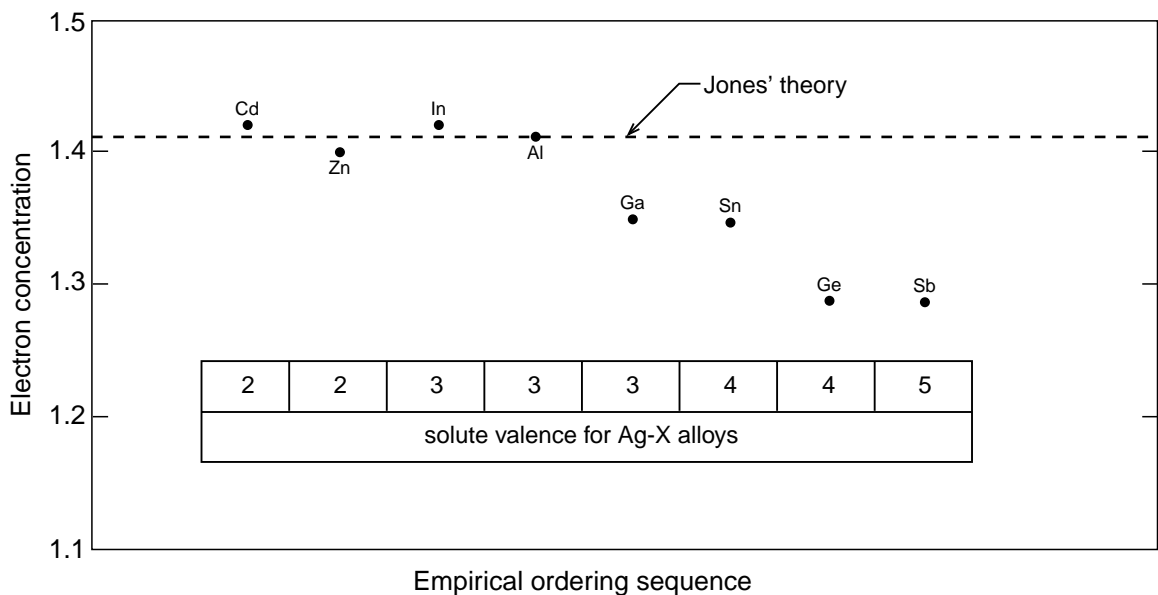
Fig. 13 B-subGroup alloying element primary solid solubility limits in silver, expressed as electron concentrations, [V(100-PSSL)+vPSSL]/100, where PSSL is the primary solid solubility limit in at. % and V and v are the number of valence electrons of the solvent and solute respectively. Data from table 1

D388-01N
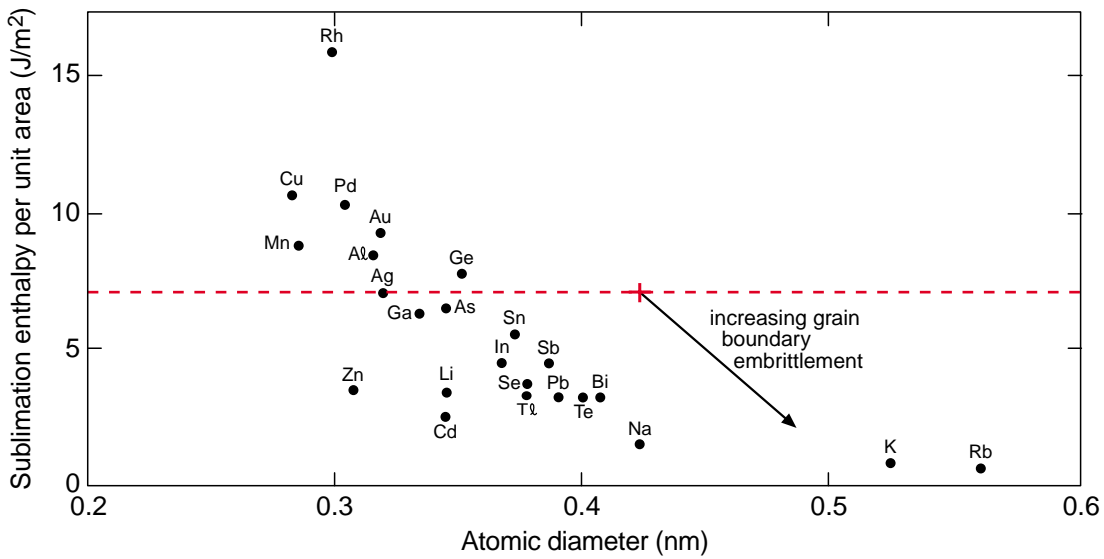
Fig. 14   Embrittlement plot for matrix (Ag) and segregant elements. After Seah (1980a), data from table 1
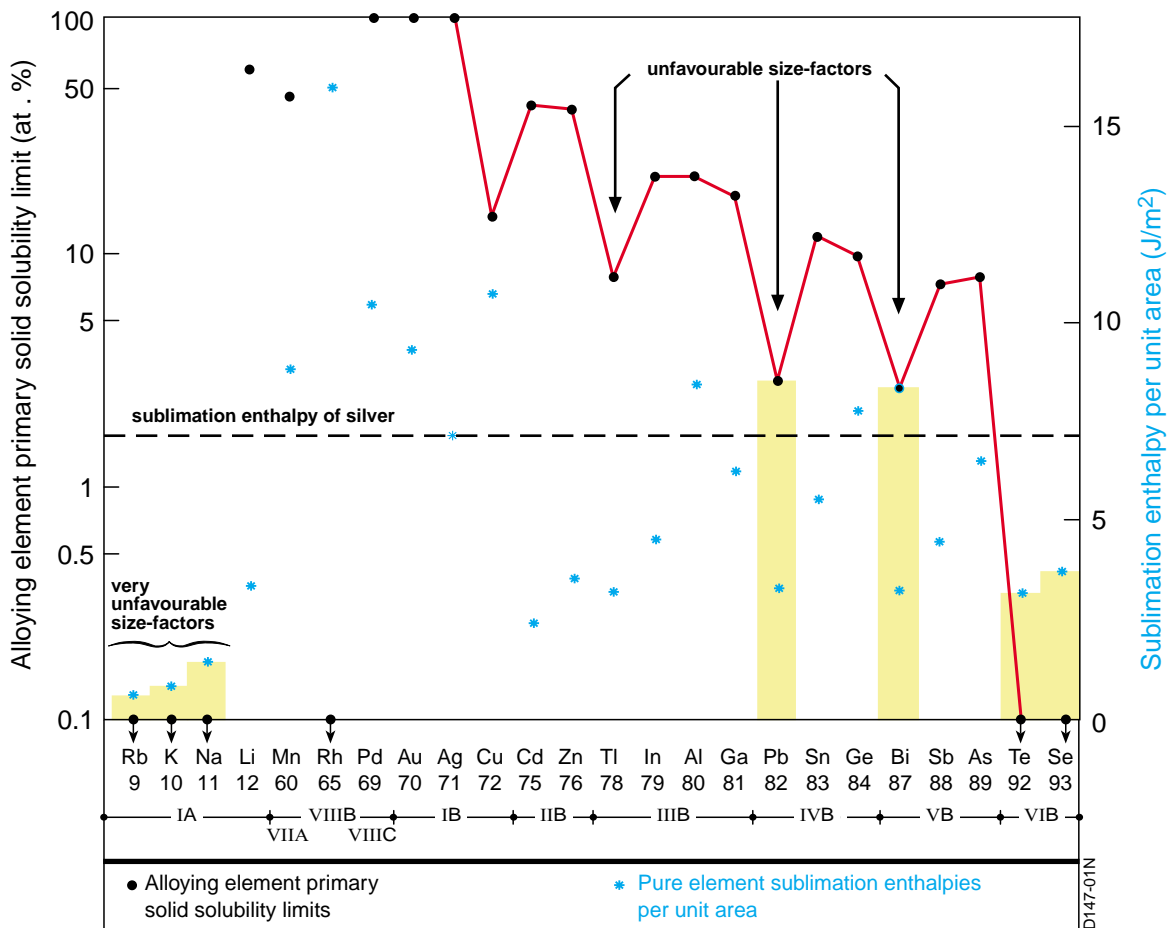
Fig. 15   Correlations between alloying element primary solid solubility limits in silver and the pure element sublimation enthalpies per unit area. The numerical sequence of the elements is the empirical ordering due to Pettifor (1988). The shaded regions denote the matrix and alloying element combinations that would seem most likely to result in segregation-induced grain boundary fracture (see text). Data from table 1

D388-01N
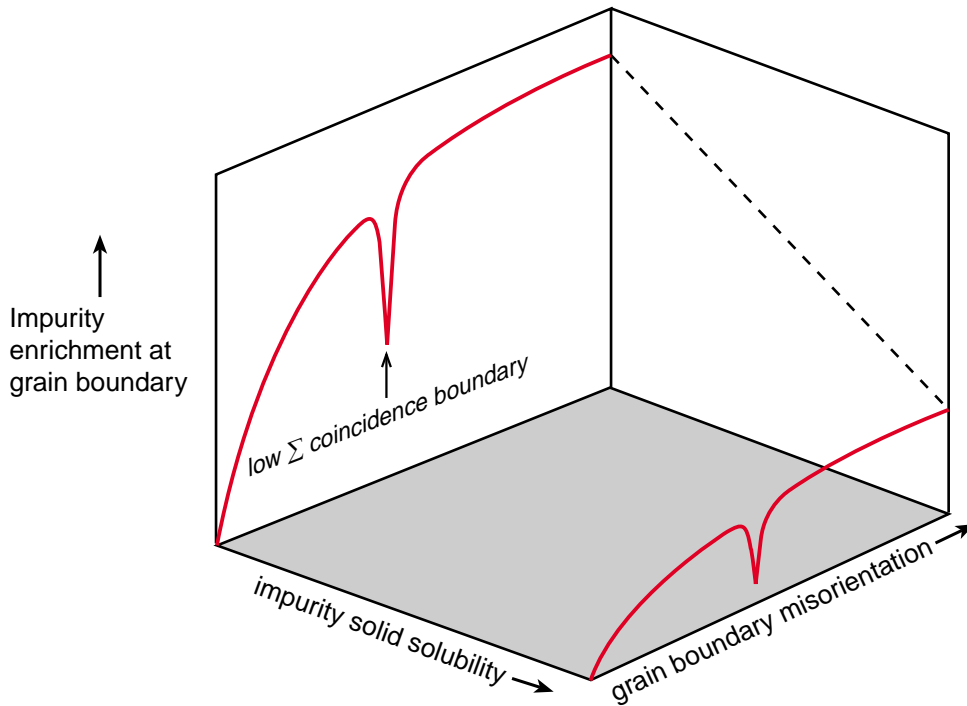
Fig. 16   Schematic grain boundary segregation diagram for grain boundaries with
              misorientations about a specific axis of rotation. After Watanabe et al. (1980)
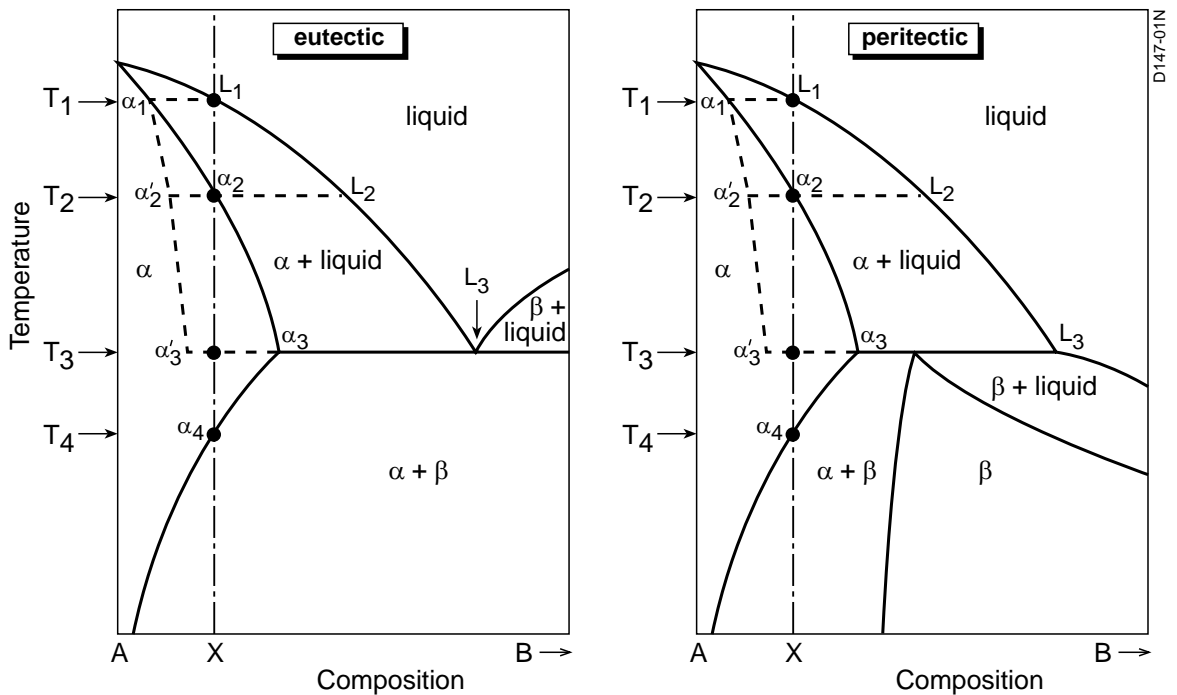
Fig. 17   Schematic binary alloy equilibrium phase diagrams involving eutectic or peritectic
              reactions and illustrating the effect of non-equilibrium cooling on solidification of
              dilute alloys of bulk composition X (see text)

D388-01N
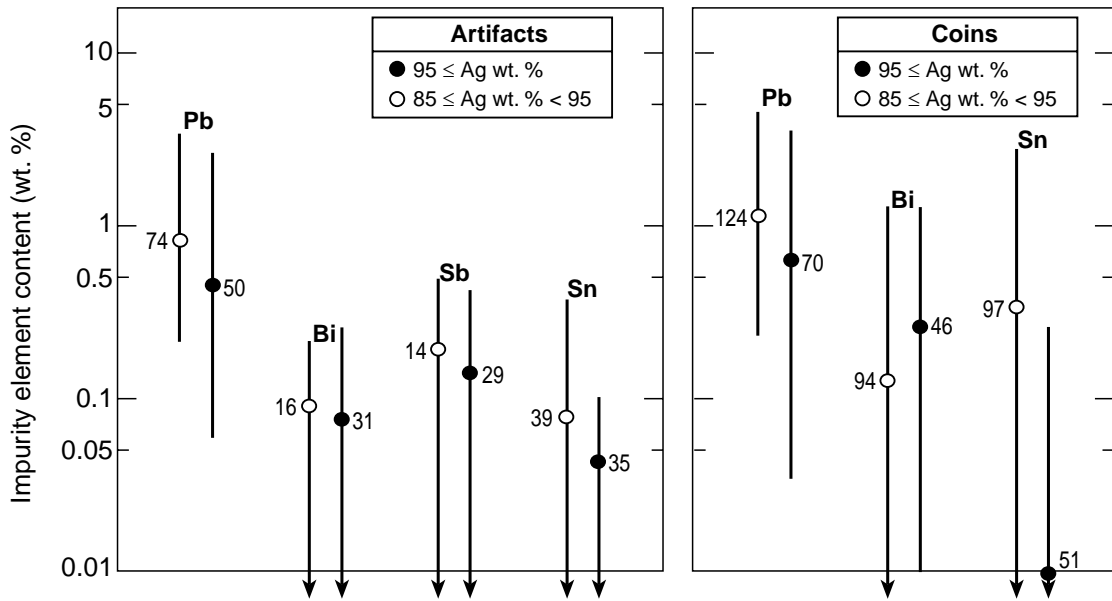
Fig. 18   Actually or potentially embrittling impurity elements in archaeological silver artifacts and coins. Data from Appendix D
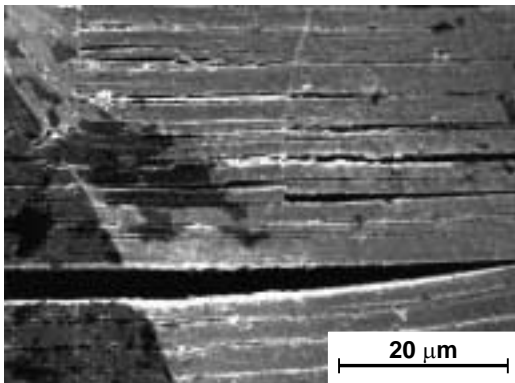
Corrosion along slip lines intersecting grain boundary facets: SEM fractograph (Wanhill *et al.* 1998)
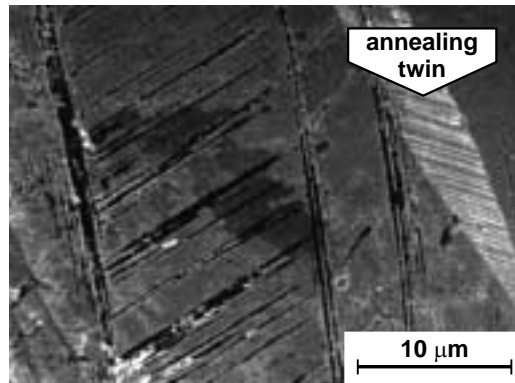
Corrosion along deformation twin boundaries intersecting a grain boundary facet: SEM fractograph (Wanhill *et al.* 1998)
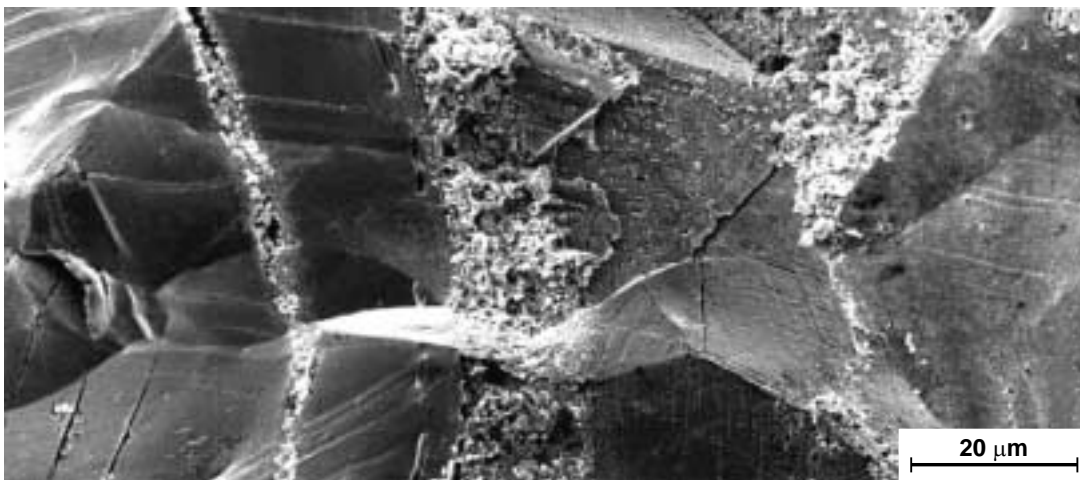
Corrosion along segregation bands intersecting grain boundary facets: SEM fractograph (Wanhill *et al.* 1998)

Fig. 19   Examples of synergistic embrittlement in an Egyptian silver vase

D388-01N

Corrosion along slip lines, possibly also along deformation twin boundaries, and intergranular cracks: metallograph (Thompson and Chatterjee 1954)

Fig. 20   *Probable synergistic embrittlement in an Indian silver coin*
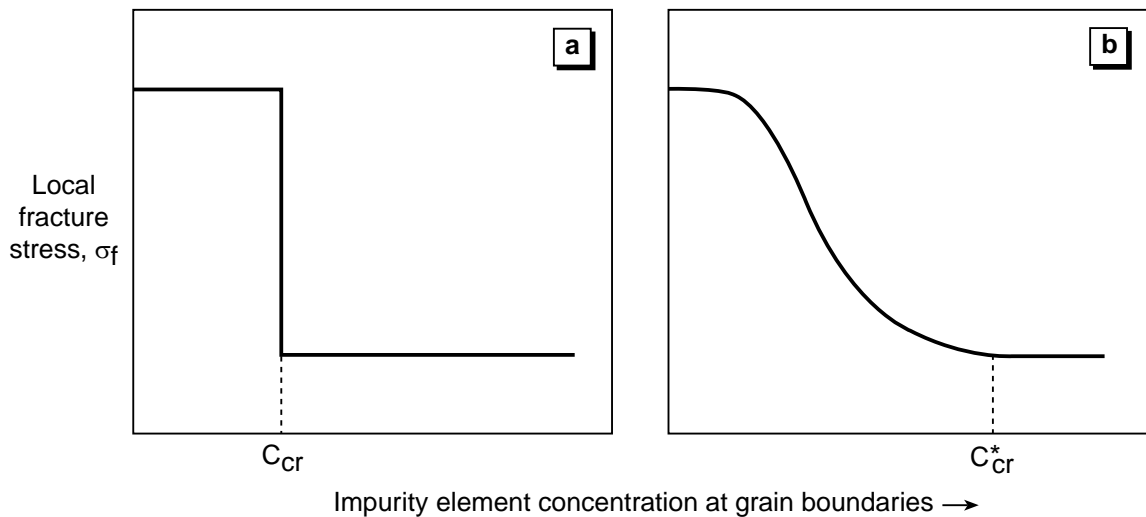
Fig. 21   *Dependence of local fracture stress, σ_f, on impurity element concentration at grain boundaries: (a) "threshold" model behaviour in which fracture stress is abruptly lowered at a critical impurity element concentration, C_{cr}; (b) more realistic behaviour with fracture stress gradually decreasing to a minimum at a critical impurity element concentration, C_{cr}^*. After Thompson and Knott (1993)*

D388-01N
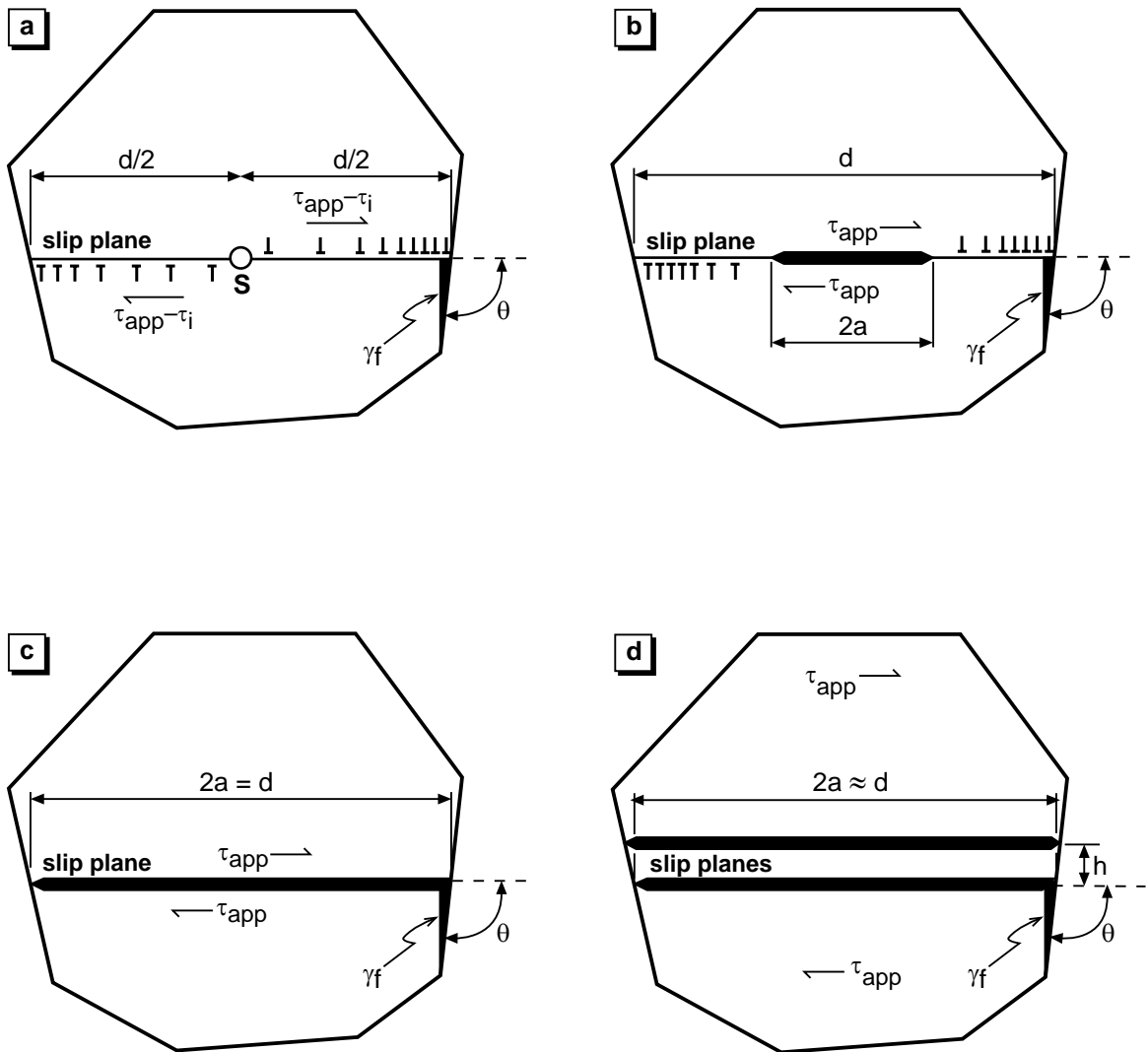
Fig. 22   Models of microcrack initiation at grain boundaries in embrittled archaeological silver.
τ_{app} = applied shear stress; τ_i = lattice friction stress; γ_f = grain boundary fracture energy;
2a = slip plane crack length; d = grain diameter; h = distance between parallel slip plane
cracks; S = dislocation source; ⊥, ⊤ = edge dislocations of opposite sign

D388-01N
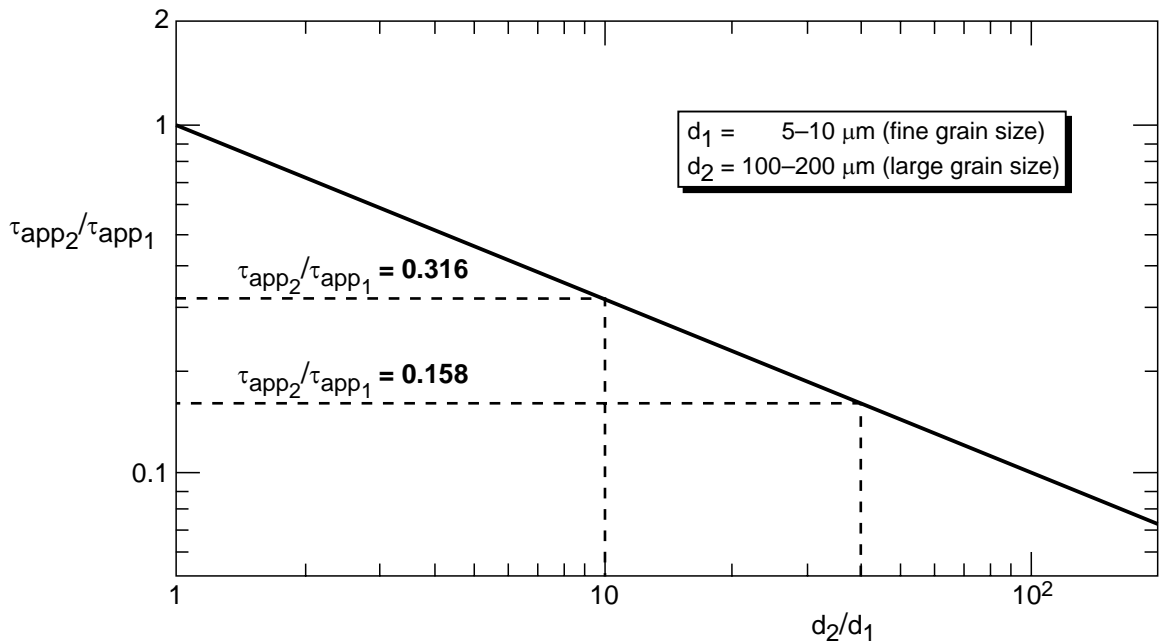
Fig. 23   Dimensionless plot of the applied shear stress, τ_{app}, versus average grain diameter, d, using the proportionality $\tau_{app} : \sqrt{1/d}$
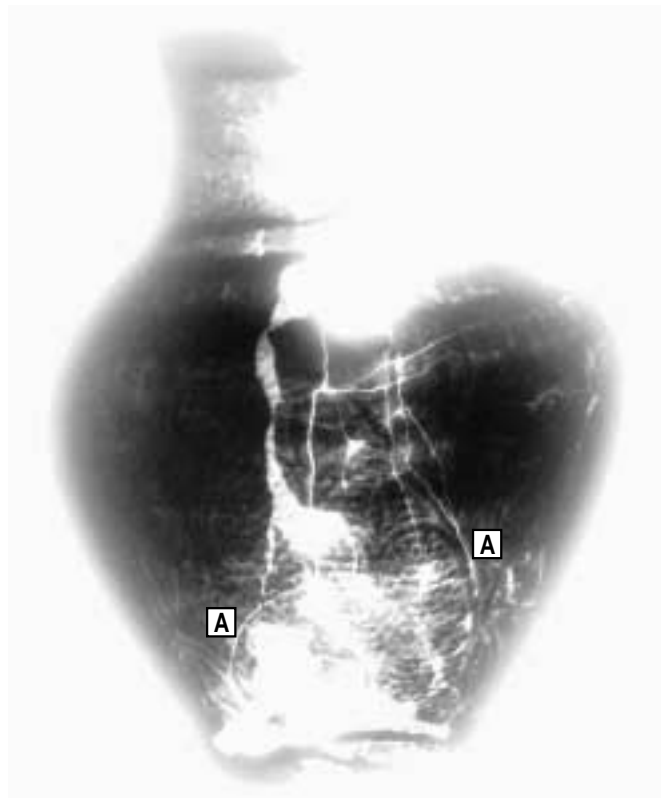
Fig. 24   X-ray image of an Egyptian silver vase (Wanhill et al. 1998). Note the hairline cracks and the brittle "eggshell" crack pattern at the upper centre of the image. The hairline cracks indicated by [A] follow external chased decorating grooves

D388-01N
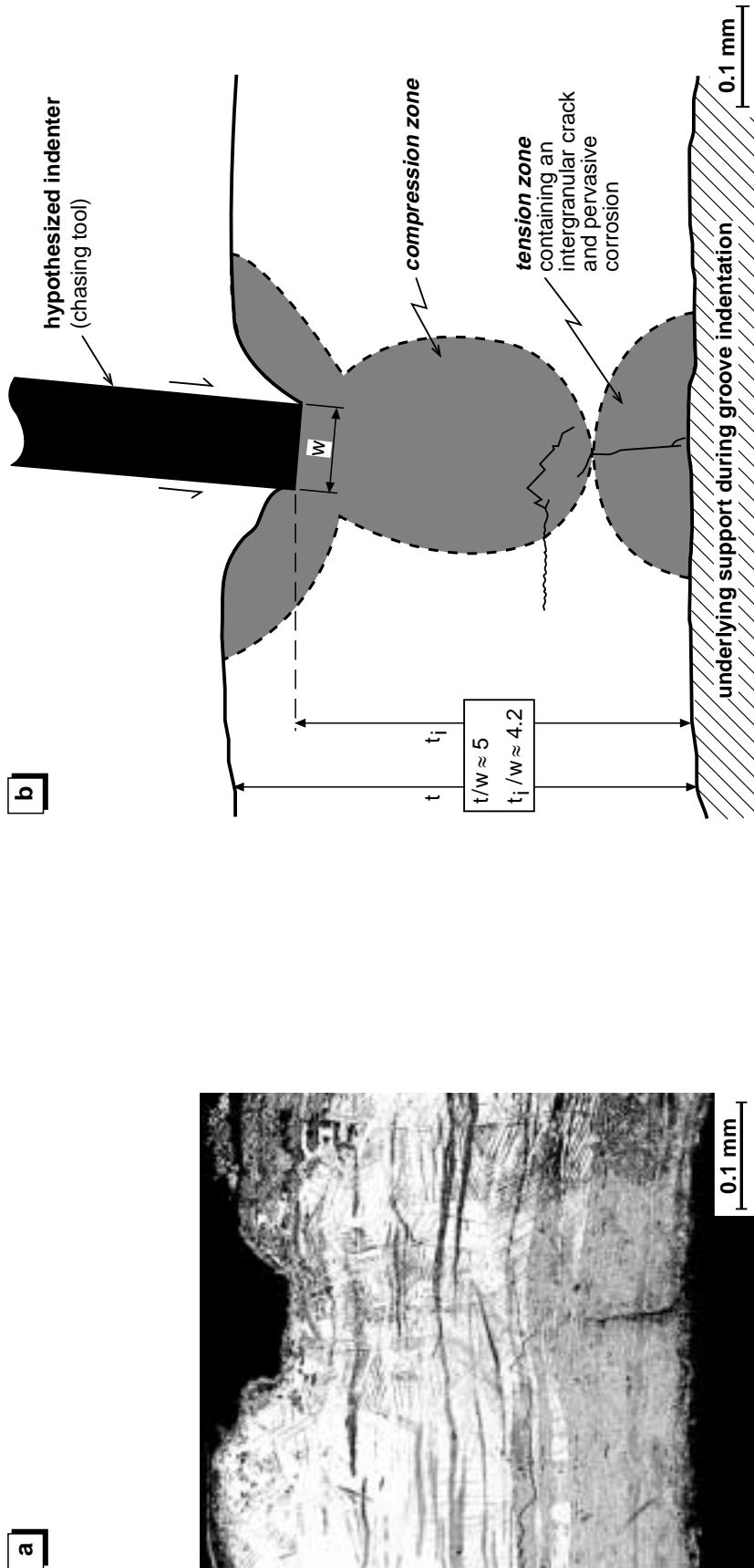
Fig. 25   Through-thickness SEM metallograph (a) and schematic (b) of an external chased decorating groove on an Egyptian silver vase (Wanhill et al. 1998, Wanhill 2000a). w = hypothesized indenter width; t = original thickness; t_i = indented thickness

D388-01N

a

hardness indent boundary

20 μm

b

hardness indent boundary

20 μm
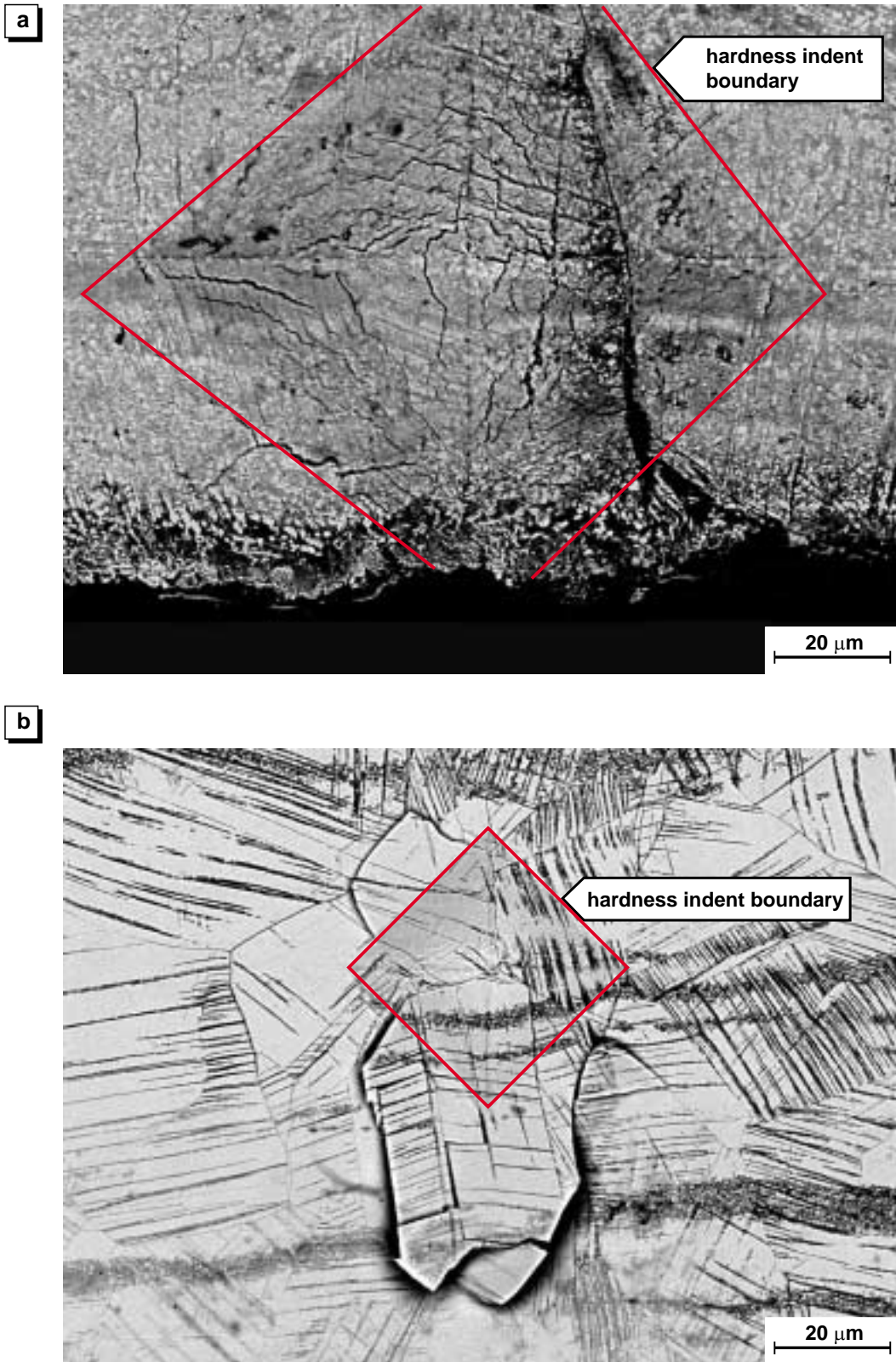
Fig. 26   *Vickers diamond pyramid microhardness indents on (a) an internally corroded area and (b) a microstructurally embrittled area in a metallographic sample from an Egyptian silver vase (Wanhill* et al. *1998). The microhardness values were (a) less than 20 HV and (b) 43 HV. The images are SEM backscattered electron metallographs*

This page is intentionally left blank.

Appendix A   Further information on discontinuous precipitation of copper in silver alloys and archaeological silver

A.1 Introduction

Discontinuous precipitation of copper in silver-copper alloys was first investigated by Fraenkel (1926). Many studies followed, e.g. Norbury (1928), Ageew *et al.* (1930), Barrett *et al.* (1935), Cohen (1937), Jones *et al.* (1942), Gayler and Carrington (1947), Rose (1957), Leo (1967), Predel and Ruge (1968), Scharfenberger *et al.* (1972), Gust *et al.* (1978), Pawlowski (1979a, 1979b). All of these studies involved precipitation experiments (ageing) at elevated temperatures, usually above 200 °C.

Smith (1965) and Werner (1965) kindled archaeometallurgical interest by suggesting discontinuous precipitation of copper might be responsible for microstructurally-induced embrittlement of archaeological silver. This was taken up by Schweizer and Meyers (1978a, 1978b, 1979), who also suggested that the precipitation could occur very slowly even at ambient temperatures, and that its microstructural characteristics might then enable distinguishing between ancient objects and fakes. In the meantime this latter suggestion appears to have been abandoned.

A.2 Discontinuous precipitation and silver embrittlement

The suggestion that discontinuous precipitation of copper could cause microstructurally-induced embrittlement of silver is discussed and discounted in the sub-section of this report on the mechanism of microstructurally-induced embrittlement. In particular, although Smith (1965) and Schweizer and Meyers (1978a, 1979) refer to Norbury (1928), it seems they overlooked his mechanical property data[H]. Figure 9 in the main part of this report shows Norbury's mechanical property data. These demonstrate a *minimum* tensile elongation of about 34 %, which by any standard is still high ductility.

On the other hand, it is reasonable that segregation of copper to grain boundaries, including discontinuous precipitation, is a primary cause of corrosion-induced embrittlement: see the sub-section of this report on the mechanisms of corrosion-induced embrittlement.

[H]   Of the references listed in sub-section A.1, Norbury's paper is the only one to include mechanical properties other than hardness values.

A.3 Some other aspects of copper precipitation in silver

Figure A.1 shows the silver-copper equilibrium phase diagram and data by Gust *et al*. (1978) on the precipitation of copper from silver-rich supersaturated (non-equilibrium) solid solutions. Figure A.2 shows these data in detail, with well-defined boundaries between discontinuous, mixed and continuous precipitation. A noteworthy feature is that the data for 7.5 wt. % copper indicate completely discontinuous precipitation up to about 610 °C, and this agrees very well with Norbury's ageing experiments *50 years earlier*, see figure A.3.

Figure A.4 shows discontinuous precipitate growth rates versus ageing temperatures for silver-copper alloys annealed before ageing. The ordinate and abscissa scales assume Arrhenius-type reaction kinetics and enable straight-line extrapolations of the data to lower temperatures. These extrapolations suggest a maximum growth rate of 10^{-3} μm/year at ambient temperatures. For objects 2000-2500 years old this means maximum precipitate widths of 2-2.5 μm at the grain boundaries. These would be visible by optical metallography, but there are two major caveats:

(1) The extrapolations ask much of the available data. Figure A.4 shows that it is a long way from precipitation at 200 °C to possible precipitation at ambient temperatures.

(2) Elevated temperature tests have shown incubation times before discontinuous precipitation begins (Gust *et al*. 1978). Incubation times could be very long, centuries or even millenia, at ambient temperatures.

In conclusion, it seems fair to state that discontinuous precipitation of copper in silver might occur at ambient temperatures, and some archaeological silver objects appear to suggest this (Schweizer and Meyers 1978a, 1979).
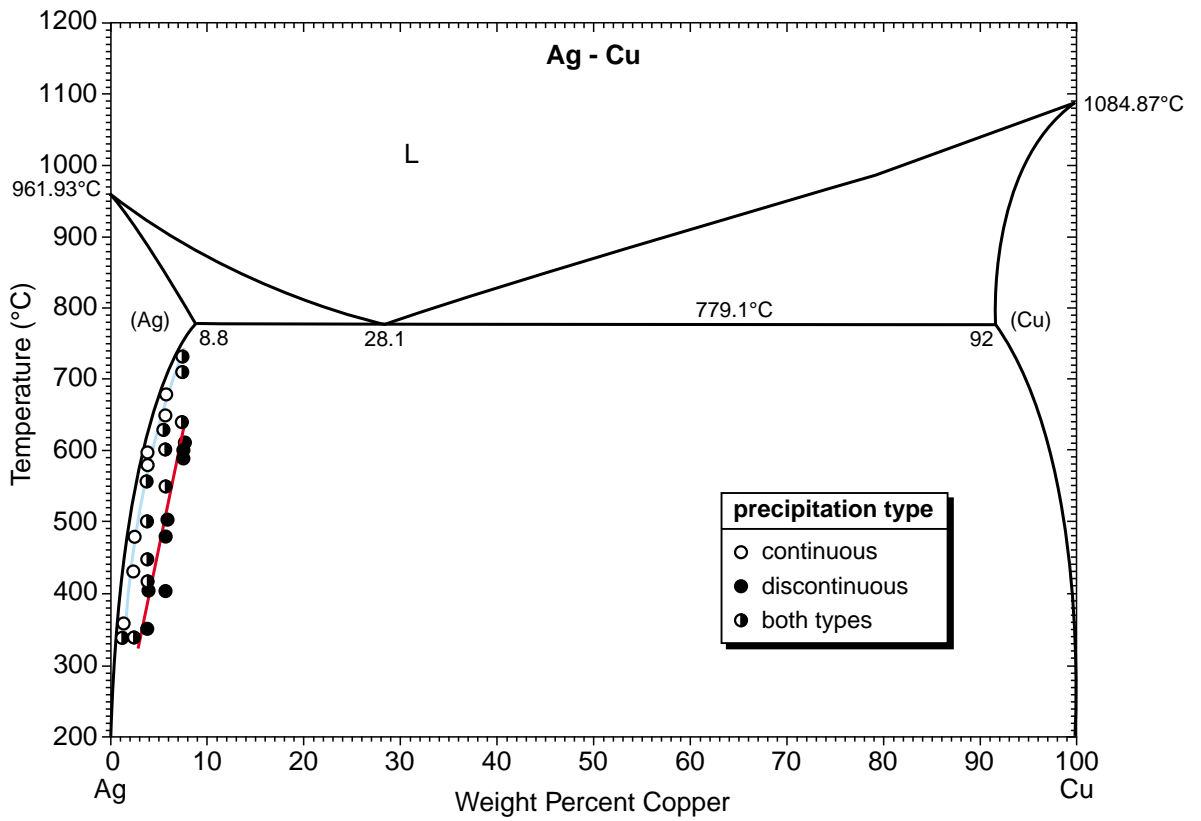
Fig. A.1   Silver-copper phase diagram (courtesy of ASM International). Copper precipitation data from Gust et al. (1978)
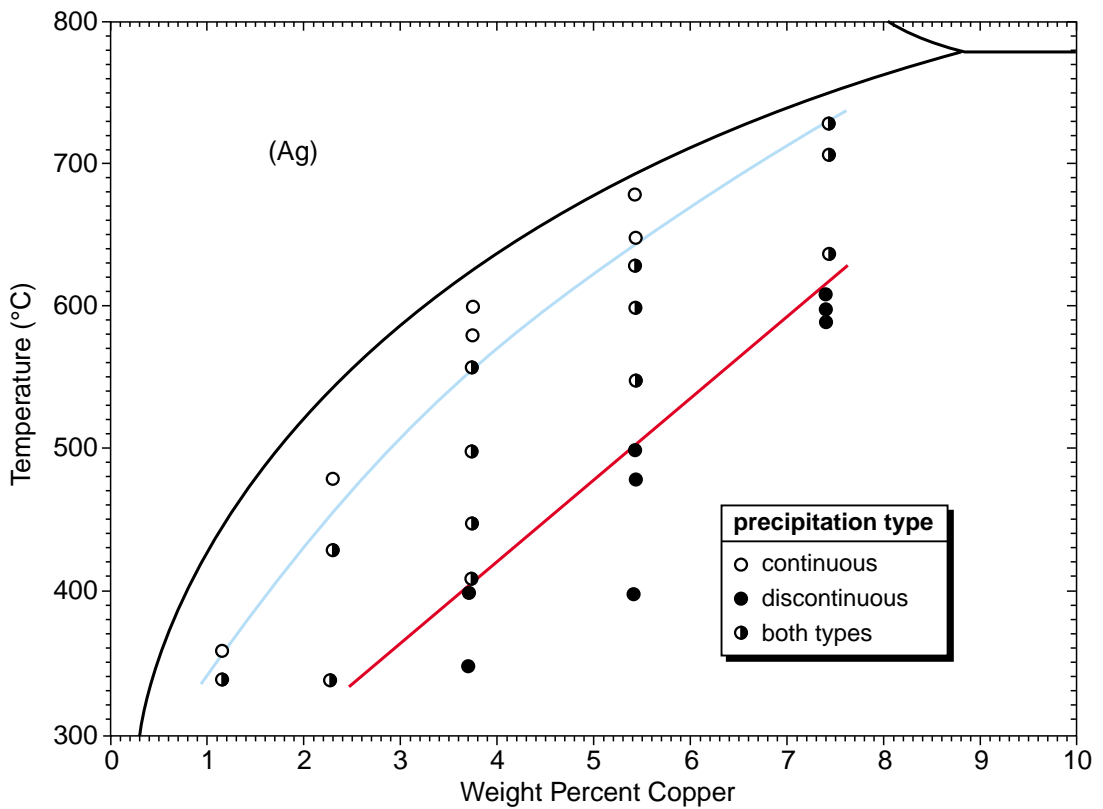
Fig. A.2   Detail of figure A.1 (Gust et al. 1978)

D388-01N
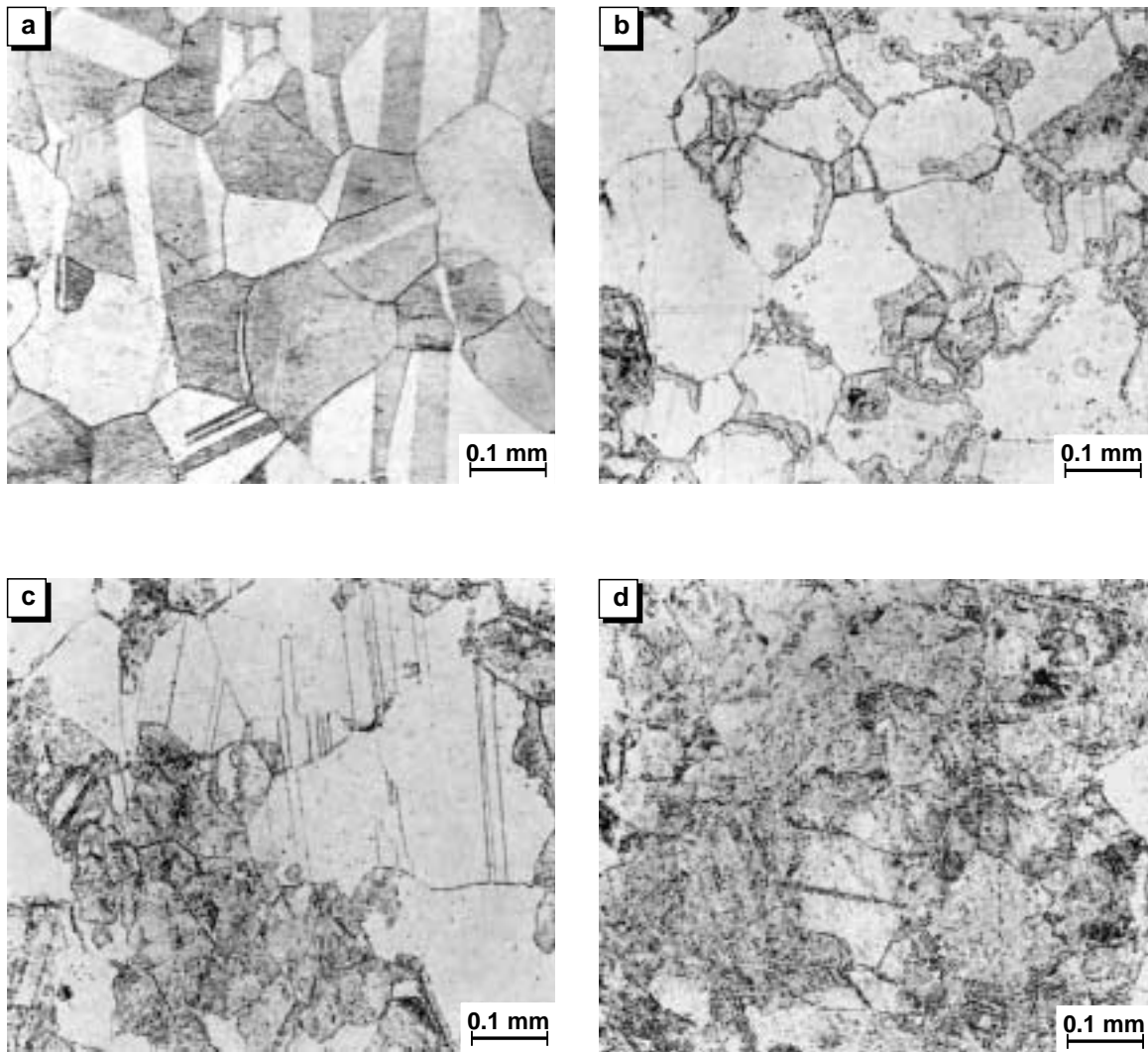
Fig. A.3 Discontinuous precipitation of copper at grain boundaries in 800°C solutionised,
quenched and 30 minutes aged standard silver, Ag-7.5 wt. % Cu (Norbury 1928):
(a)   250°C aged: precipitation beginning at some grain boundaries
(b)   356°C aged: precipitation further advanced
(c   440°C aged: precipitation still further advanced
(d)   570°C aged: precipitation practically complete
(photographs reproduced courtesy of the Institute of Materials, London)

D388-01N
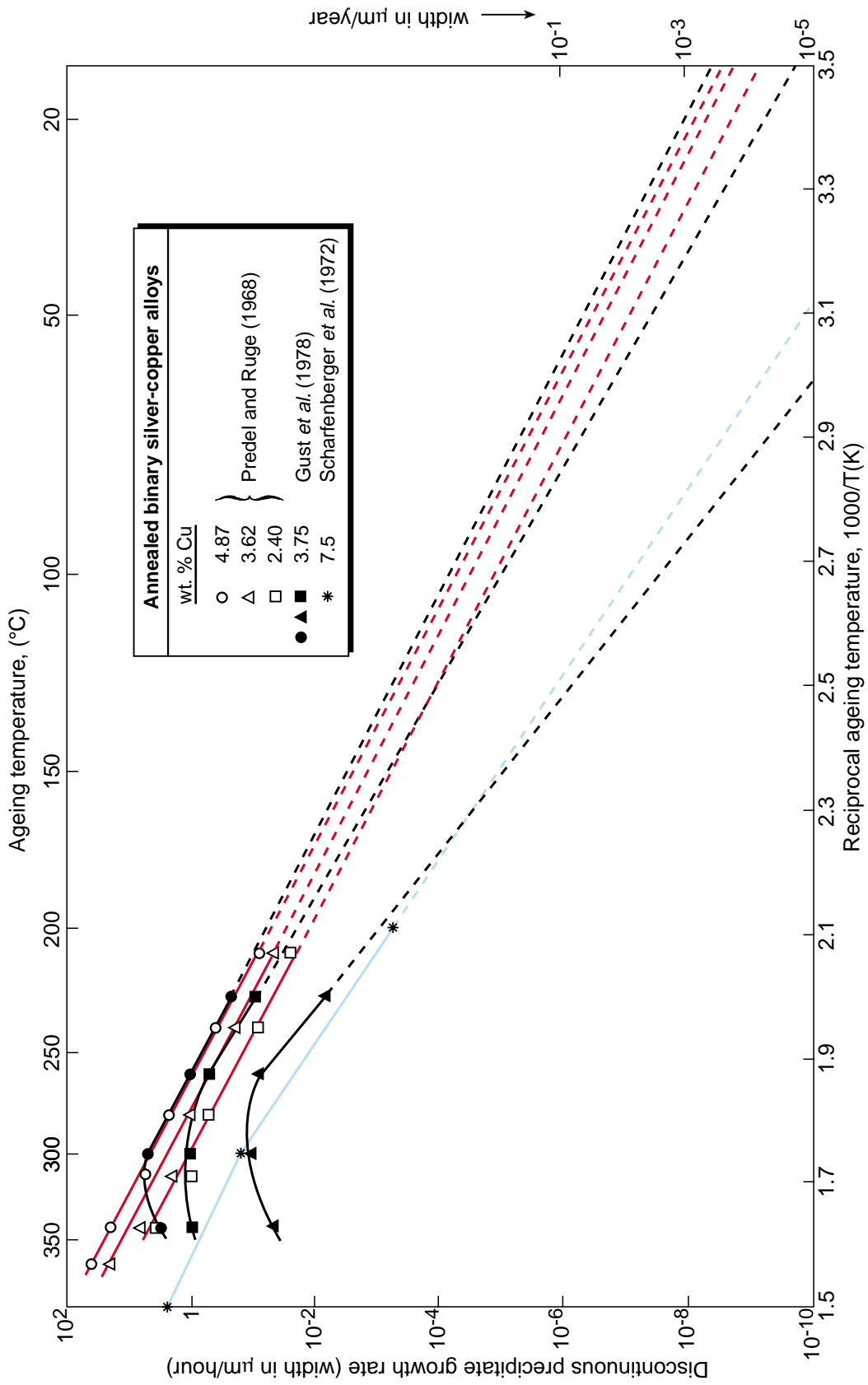
Fig. A.4 Temperature dependence of copper discontinuous precipitation growth rates in binary silver-copper alloys: the extrapolations to low and ambient temperatures assume Arrhenius-type reaction kinetics

Appendix B Further information on corrosion along slip lines

B.1 Nomenclature, definitions and some interplanar angles

fcc   : face centred cubic crystal structure, illustrated here
         by a unit cell of the crystal lattice

SCC   : Stress Corrosion Cracking

σ_n, σ_{n1}, σ_{n2} : local normal stresses, i.e. stresses normal to
         particular planes at particular locations

$\perp$: symbol for an edge dislocation, which is a type of line discontinuity in
         the crystal lattice. The diagram below shows a unit edge dislocation in a
         simple cubic lattice

extra half plane of atoms

dislocation core

dislocation line
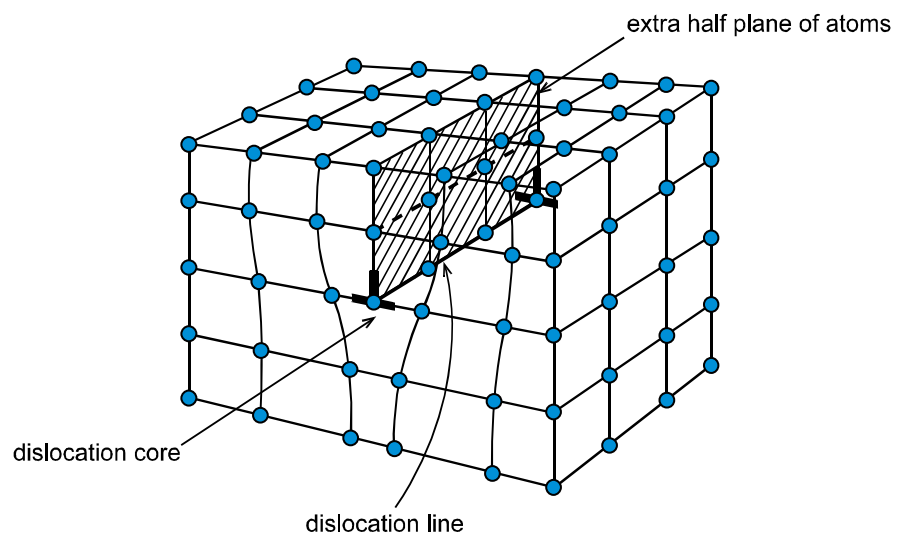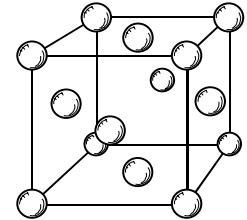
cubic crystal   : each plane and direction is denoted by three indices, hkl. Families of
lattice planes   equivalent planes and directions are placed between braces { } and carets
and directions   < > respectively. Some important planes and directions are illustrated on
         the next page.
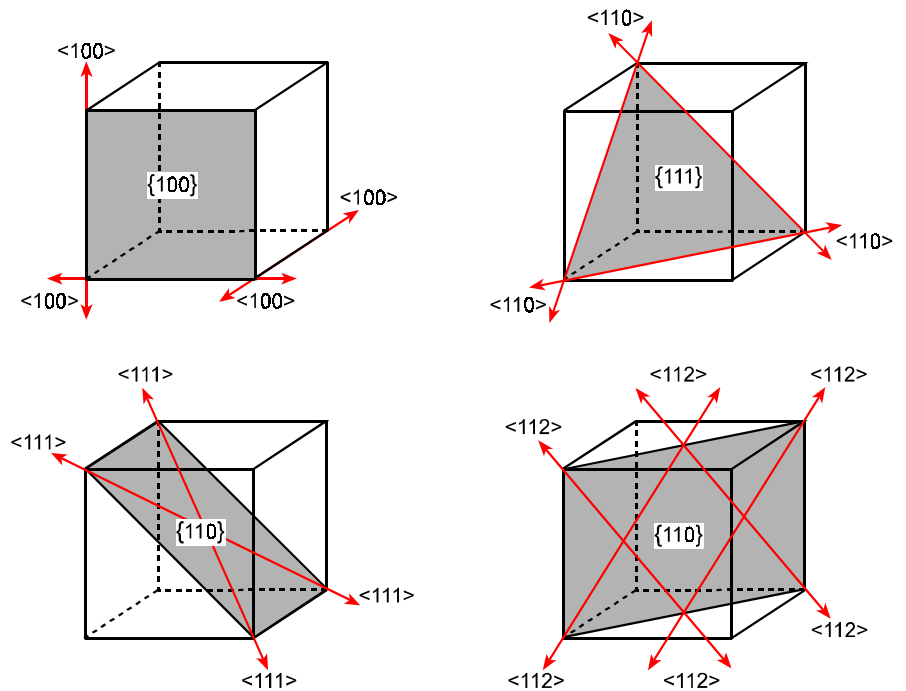
slip ; slip planes and slip directions : slip is the sliding of one part of a crystal across a neighbouring part. Slip is anisotropic, taking place along certain planes and directions in the crystal lattice, the slip planes and slip directions. Slip actually occurs incrementally, by the passage of numerous dislocations along the slip planes. For fcc metals the slip planes are {111} type and the slip directions are <110>

ANGLES BETWEEN SOME LOW-INDEX CRYSTALLOGRAPHIC PLANES FOR THE CUBIC CRYSTAL STRUCTURE					
{HKL}	{hkl}	ANGLES BETWEEN {HKL} AND {hkl} PLANES			
100	100	0°	90°		
	110	45°	90°		
	111	54° 44′			
	112	35° 16′	65° 54′		
110	110	0°	60°	90°	
	111	35° 16′	90°		
	112	30°	54° 44′	73° 13′	90°
111	111	0°	70° 32′		
	112	19° 28′	61° 52′	90°	

B.2 Introduction

Corrosion along slip lines can occur in an archaeological silver object that has not been annealed after (final) mechanical working. The corrosion may eventually lead to cracking. Figure B.1 illustrates slip line corrosion, cracking and the resulting crystallographic fracture observed for an Egyptian silver vase about 2200-2300 years old (Wanhill *et al*. 1998).

Unlike tarnishing, corrosion *in* silver must be slow. Figure B.1a shows the slip lines are marked by tiny pits, which probably represent highly localised corrosion at lattice dislocations. Since dislocations are "frozen in" when plastic deformation, e.g. mechanical working, ceases (Kuhlmann-Wilsdorf 2001), the pits could be many centuries old.

Over the last decade models linking corrosion along slip lines to transgranular stress corrosion cracking (SCC) have been proposed for alloys with the same crystal structure as silver, namely the face centred cubic (fcc) structure (Flanagan *et al*. 1991, 1993; Lichter *et al*. 1996; Magnin 1996, 114-124; Magnin *et al*. 1996; Lichter *et al*. 2001). These models are discussed qualitatively in this Appendix and then related and compared to the corrosion-induced crystallographic fracture in archaeological silver.

B.3 The first stage of cracking: corrosion along slip lines and slip plane dissolution

Several classes of fcc alloys undergo corrosion along slip lines (Scully 1971; Lichter *et al*. 1996; Magnin *et al*. 1996) besides archaeological silver. Corrosion begins as pitting attack of the highly strained crystal lattice at the cores of surface-connected dislocations. The pits develop into slots that can eventually merge to result in slip plane dissolution (Lichter *et al*. 1996, 2001) and crack formation, as is seen in figure B.1b. For fcc metals the slip planes are {111} type, and so the cracks lie on {111} fracture planes.

B.4 The second stage of cracking: transgranular SCC

At this stage the cracking diversifies in the choice of average crystallographic fracture plane and the fracture topography. Single crystal SCC experiments have shown that the average fracture planes are usually {110} in copper alloys (Flanagan *et al*. 1991, 1993; Lichter *et al*. 1996) and {100} in austenitic stainless steels (Magnin 1996, 88), although average {110} fracture also occurs in austenitic stainless steels (Magnin *et al*. 1996).

In more detail the fracture topographies reveal microfaceting. The fracture surfaces for copper alloys show {110} microfacets whose morphologies depend on the average crack growth

direction, see figures B.2a and B.2b. The fracture surfaces for austenitic stainless steels consist partly, and sometimes entirely, of {111} microfacets. This is schematically illustrated in figures B.2c and B.2d.

B.5 Comparison of the fractures due to slip plane dissolution and transgranular SCC

The fracture topography due to slip plane dissolution in archaeological silver, figure B.1c, is less complex than the transgranular SCC fractures illustrated in figure B.2. The silver fracture topography consists of {111} facets and mainly straight ledges. Most of these ledges could be {111} type planes as well. However, figure B.1b shows a large ledge "dog-legging" and normal to a slip plane crack: this indicates another type of plane for the ledge, e.g. {110} or {112}.

B.6 Suggested models of transgranular SCC

The models proposed for transgranular SCC in fcc alloys have been termed "corrosion-assisted cleavage" (Flanagan *et al*. 1991, 1993; Lichter *et al*. 1996), "strain-enhanced dissolution" (Lichter *et al*. 2001), and "corrosion-enhanced plasticity" (Magnin 1996, 114-124; Magnin *et al*. 1996). Figure B.3 gives two-dimensional basic schematics of the models. These are discussed in sub-sections B.6.1 − B.6.3.

B.6.1 The corrosion-assisted cleavage model

This model was developed to explain the transgranular SCC fracture features in single crystals of copper-gold and copper-zinc alloys (Flanagan *et al*. 1991, 1993; Lichter *et al*. 1996). Following the top diagram and the left-hand column in figure B.3, the proposed sequence of events is:

(a) Arrest of a {110} type crack by dislocation blunting, i.e. emission of dislocations on a slip plane intersecting the crack tip.

(b) Pile up of dislocations at an obstacle, specifically a sessile dislocation called a Lomer-Cottrell barrier (Lomer 1951; Cottrell 1952). There is also renucleation of the arrested crack by slip plane dissolution at the crack tip. This changes the stress state at the Lomer-Cottrell barrier by raising the local normal stress, σ_n. The barrier is now the location of an incipient crack.

(c) Failure of the Lomer-Cottrell barrier by {110} type cleavage microcracking.

(d)   Linking of the main crack and microcrack via further slip plane dissolution.

This proposed sequence of events takes place three-dimensionally, with multiple cleavage cracks initiating from many Lomer-Cottrell barriers on a slip plane intersecting the main crack front[G]. The result is suggested to explain microfaceted fracture topographies like those in figures B.2a and B.2b.

B.6.2 The strain-enhanced dissolution model

This model is considered by the authors (Lichter *et al*. 2001) to supersede the corrosion-assisted cleavage model for transgranular SCC in copper-gold and copper-zinc alloys, and also likely to be more generally applicable, e.g. to austenitic stainless steels. Following the middle column in figure B.3, the proposed – here much simplified – sequence of events is:

(a, b) Crack growth by slip plane dissolution, enhanced by the strain associated with the local normal stress, σ_{n1}. The slip plane dissolution continues as long as σ_{n1} exceeds the local normal stress, σ_{n2}, on alternative planes, e.g. {110} or {100} type.

(c)   Crack growth by strain-enhanced directed dissolution on an alternative plane whose local normal stress, σ_{n2}, exceeds σ_{n1} but is not high enough to blunt the crack tip by dislocation emission.

B.6.3 The corrosion-enhanced plasticity model

This model was developed to explain the transgranular SCC fracture features in single crystals of austenitic stainless steels (Magnin 1996, 114-124; Magnin *et al*. 1996). Following the top diagram and the right-hand column in figure B.3, the proposed sequence of events is:

(a, b) Slip occurs at the crack tip, depassivating the metal and allowing slip plane dissolution to begin. This corrosion process causes a stress concentration, vacancy production and adsorption/absorption of hydrogen, all of which reduce the shear stress needed for dislocation movement along the slip plane. The result is corrosion-enhanced localised plasticity whereby more dislocations are emitted from the crack tip. The dislocations pile up against an obstacle, for example a precipitate or prior dislocation tangle. If the obstacle is strong enough, and particularly if the local fracture energy is reduced by hydrogen absorption, then the head of the pile-up becomes the location of an incipient crack.

[H]   The crystallographic and mechanistic details of this model are complex. See Flanagan *et al*. (1991, 1993).

(c)   A microcrack forms at the head of the pile-up by a Stroh-like mechanism (Stroh 1954, 1957). The microcrack nucleates and forms owing to the combined action of the local normal stress, σ_n, and absorbed hydrogen. In general the microcrack forms on a {111} type plane, but sometimes on {100} or {110} type planes.

(d)   Linking of the main crack and microcrack via slip plane decohesion owing to the combined action of the local normal stress, σ_n, and absorbed hydrogen. This is followed by slip at the new crack tip and repetition of the entire sequence of events.

B.7 Comparison of the transgranular SCC models with corrosion-induced crystallographic fracture in archaeological silver

Two main points can be made directly:

(1)   The corrosion-assisted cleavage model is considered superseded by the strain-enhanced dissolution model (Lichter *et al*. 2001).

(2)   Silver corrosion does not result in hydrogen generation, see Pourbaix (1963), and so the corrosion-enhanced plasticity model is not applicable to silver.

There remains the possibility that the strain-enhanced dissolution model could provide further insight into the corrosion-induced crystallographic fracture in archaeological silver. In fact, it does: the model's hypothesis of strain-enhanced directed dissolution explains the large ledge "dog-legging" and normal to the slip plane crack in figure B.1b. The 90° angle between the ledge and slip plane means the ledge is not on a {111} type plane and therefore not due to slip plane dissolution.

The strain-enhanced dissolution model also has a more general implication. It reduces the distinction between corrosion along slip lines, slip plane dissolution and transgranular SCC. In other words, these phenomena are seen to have a common cause, namely the enhancement of corrosion by local strains in the crystal lattice.

B.8 Summary

Corrosion along slip lines, slip plane dissolution, non-slip plane dissolution, and the resulting crystallographic fracture in archaeological silver are slow processes, taking many centuries. These phenomena are explained by the strain-enhanced dissolution model proposed by Lichter *et al*. (2001) to account for both slip plane dissolution and transgranular SCC in fcc alloys. There is a common cause, the enhancement of corrosion by local strains in the crystal lattice.

D388-01N
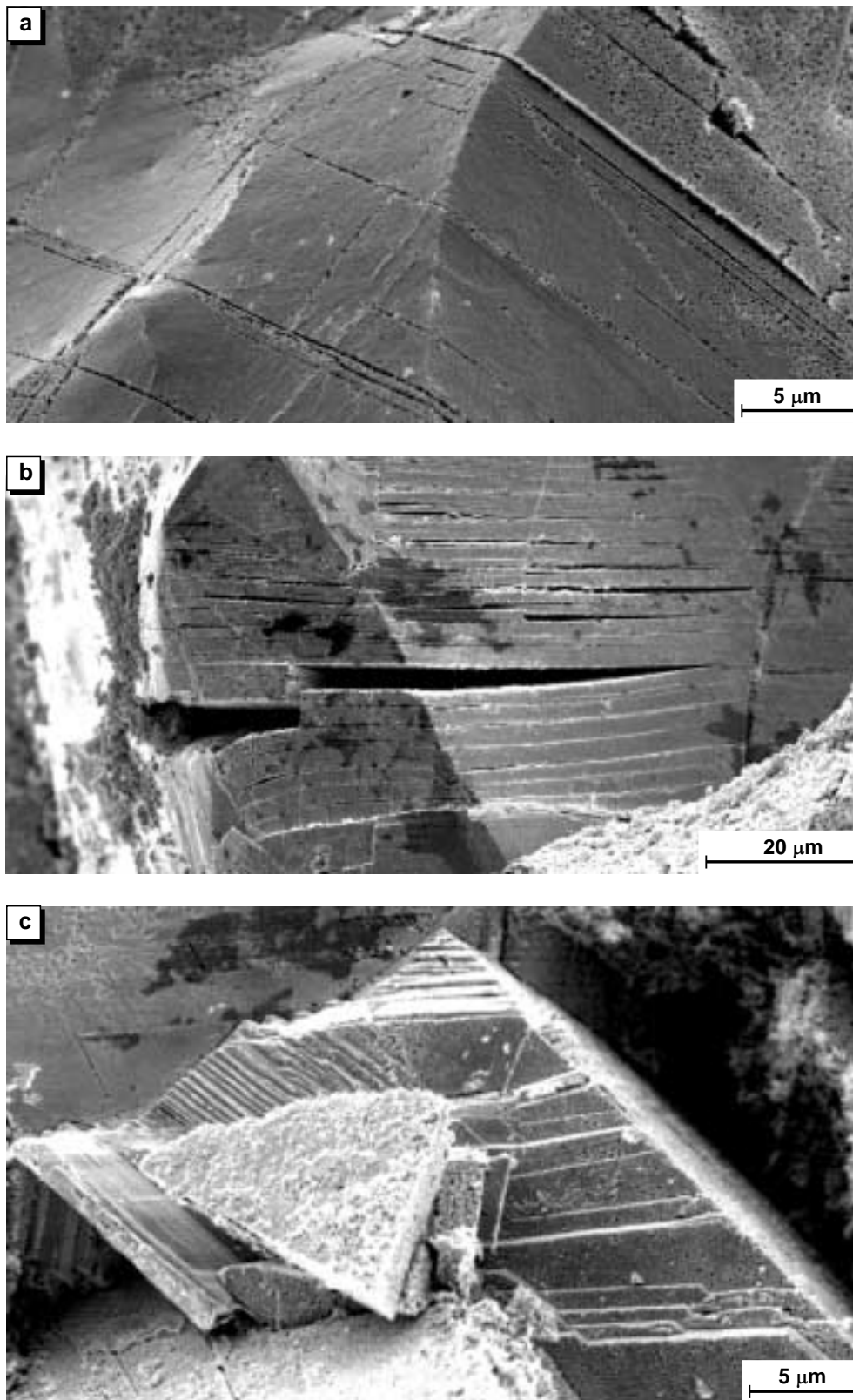
Fig. B.1 Slip line corrosion (a), cracking (b) and fracture topography (c) revealed by synergistic embrittlement of an Egyptian silver vase (Wanhill et al. 1998): SEM fractographs

D388-01N
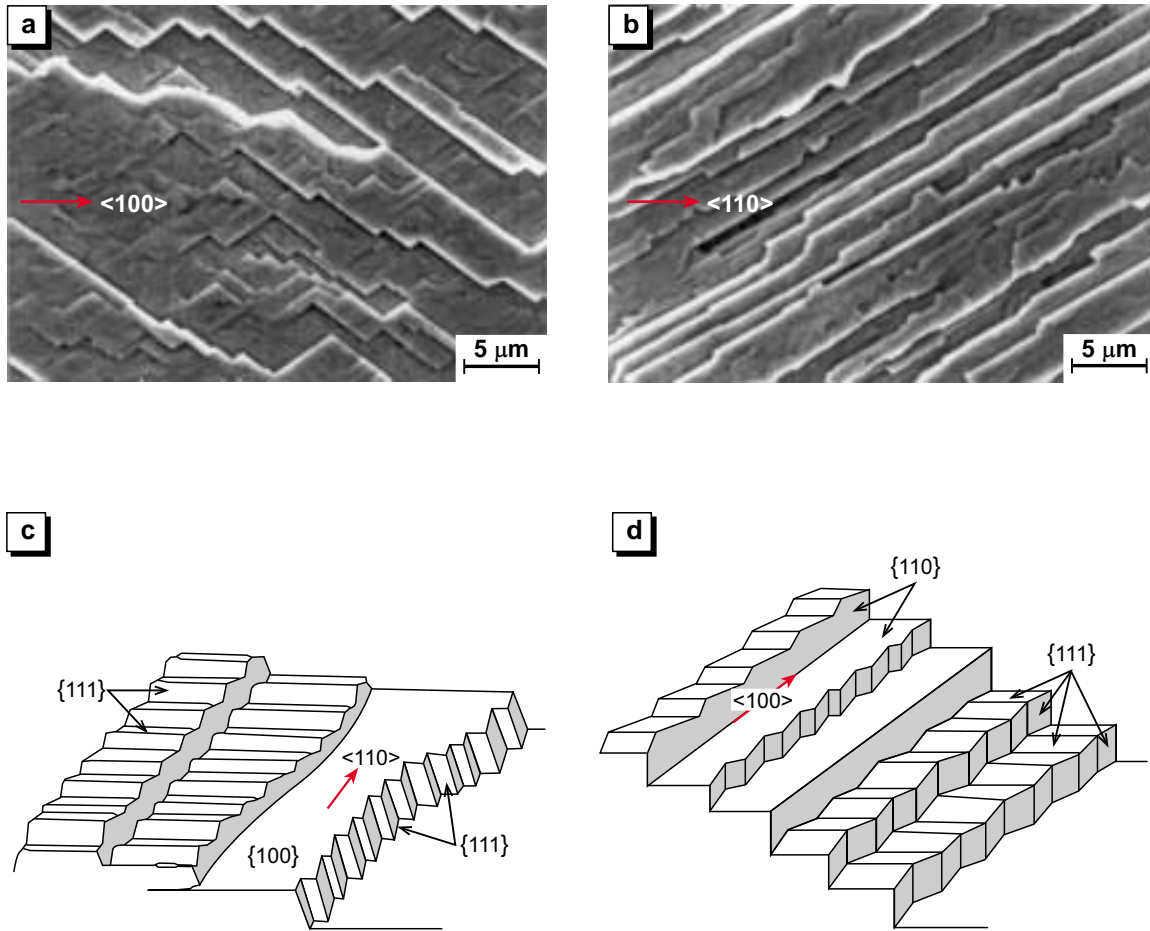
Fig. B.2 Transgranular stress corrosion cracking (SCC) topographies for (a,b) copper alloys
(Flanagan et al. 1993) and (c,d) austenitic stainless steels (Magnin 1996, 88-92;
Magnin et al. 1996). The SEM fractographs are courtesy of B.D. Lichter, Vanderbilt
University, Nashville, Tennessee, U.S.A.

D388-01N

a

slip plane

obstacle to
dislocation glide

"Corrosion-assisted cleavage"   **"Strain-enhanced dissolution"**   **"Corrosion-enhanced plasticity"**

b

{110}

incipient
crack

a

b

incipient
crack

c

σ_n

σ_n

cleavage

b

σ_{n_1}

σ_{n_1}

slip plane
dissolution

c

σ_n

σ_n

decohesion

d

slip plane
dissolution

c $\sigma_{n_2} > \sigma_{n_1}$

σ_{n_2}

σ_{n_2}

strain-enhanced
directed
dissolution

d

σ_n

σ_n

slip plane
decohesion
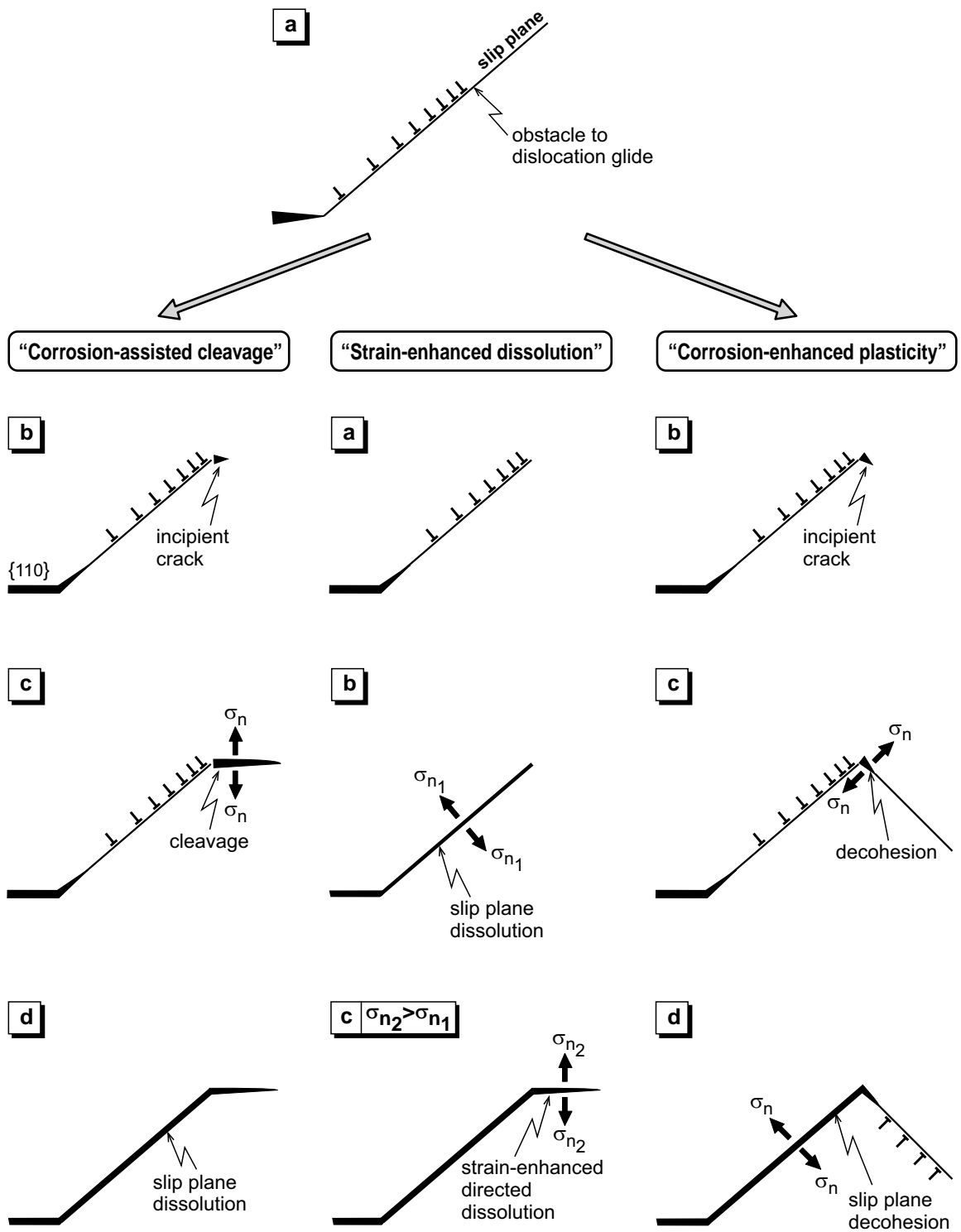
*Fig. B.3   Schematics of models proposed for transgranular SCC in fcc alloys. σ_n = local normal
stress; $\perp$, $\top$ = edge dislocations of opposite sign. See section B.6 for further information*

Appendix C Silver binary alloy equilibrium phase diagrams in support of table 2

C.1 Atomic weights

ELEMENT	SYMBOL	ATOMIC WEIGHT*	ELEMENT	SYMBOL	ATOMIC WEIGHT*
silver	Ag	107.880	antimony	Sb	121.76
arsenic	As	74.91	selenium	Se	78.96
bismuth	Bi	209.00	tin	Sn	118.70
germanium	Ge	72.60	tellurium	Te	127.61
sodium	Na	22.997	thallium	Tl	204.39
lead	Pb	207.21			

* As published in the Journal of the American Chemical Society, April 1950.

C.2 Interconversion of weight and atomic percentages in binary alloy systems

If w_x and a_x represent the weight and atomic percentages of one component having atomic weight x, and if w_y, a_y and y represent the corresponding quantities for the second component, then:

$$w_y = 100 - w_x$$
$$a_y = 100 - a_x$$

The conversion from weight to atomic percentages, or vice versa, may be made by use of the following formulae:

$$a_x = \frac{100}{1 + (x/y)[(100/w_x) - 1]}$$

$$w_x = \frac{100}{1 + (y/x)[(100/a_x) - 1]}$$

D388-01N

C.3   Phase diagrams (courtesy of ASM International)

C.3.1   Alloying elements with zero or very low primary solid solubilities

D388-01N

Ag - Te

Phase diagram with axes: Temperature (°C) on the vertical axis (100 to 1200) and Weight Percent Tellurium on the horizontal axis (0 Ag to 100 Te).

Labels within the diagram:
- L_1
- L_2
- L + G
- G →
- 961.93°C
- 960°C
- 13.8 881°C 34
- 13.3 869°C
- 802°C
- 689°C 44.4
- 37.6
- γ Ag$_2$Te
- β Ag$_2$Te
- β Ag$_{1.9}$Te
- α Ag$_{1.9}$Te
- α Ag$_2$Te
- 37.4 460°C 55.9
- 420°C 59.7
- 42
- 353°C
- 70.3
- 295°C
- 449.57°C
- (Ag)
- (Te) →
- 265
- 178
- α Ag$_5$Te$_3$
- β Ag$_5$Te$_3$
- 145°C

D388-01N
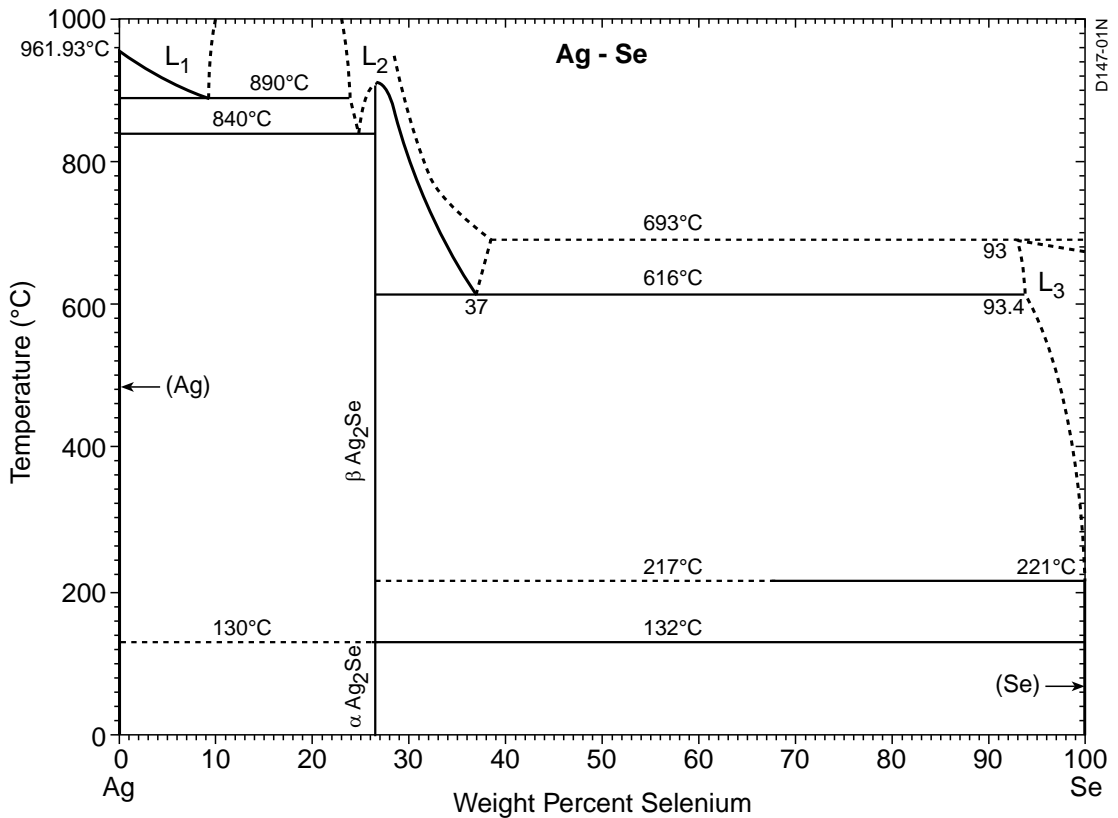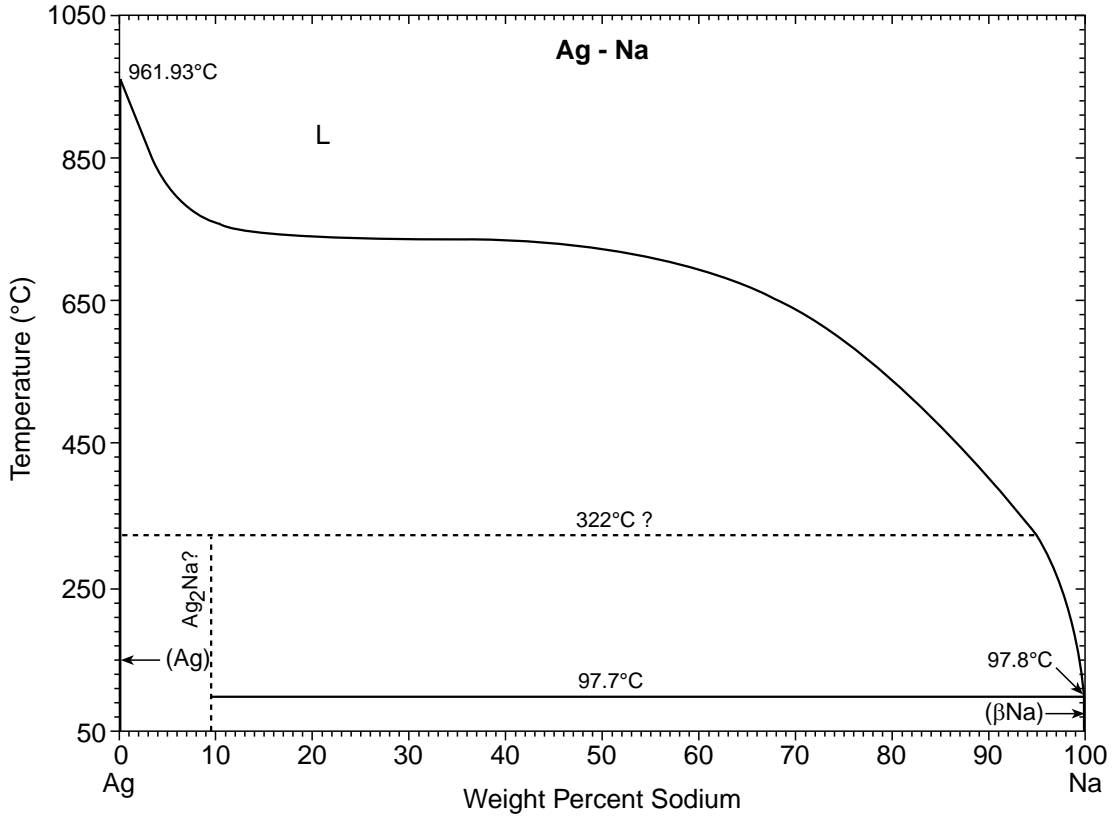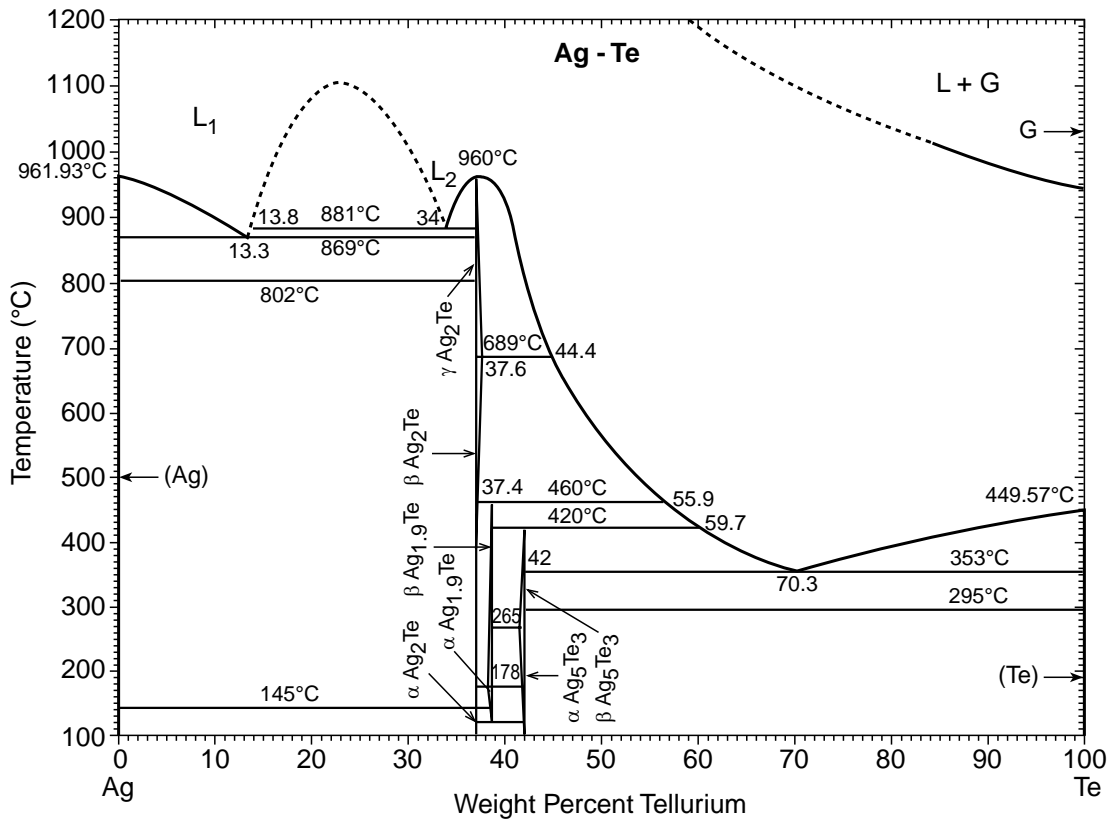
C.3.2 Alloying elements with maximum primary solid solubilities at eutectic or peritectic temperatures

Ag - As

Ag - Ge

D388-01N

Ag - Sb

D147-01N

Ag - Sn

D388-01N
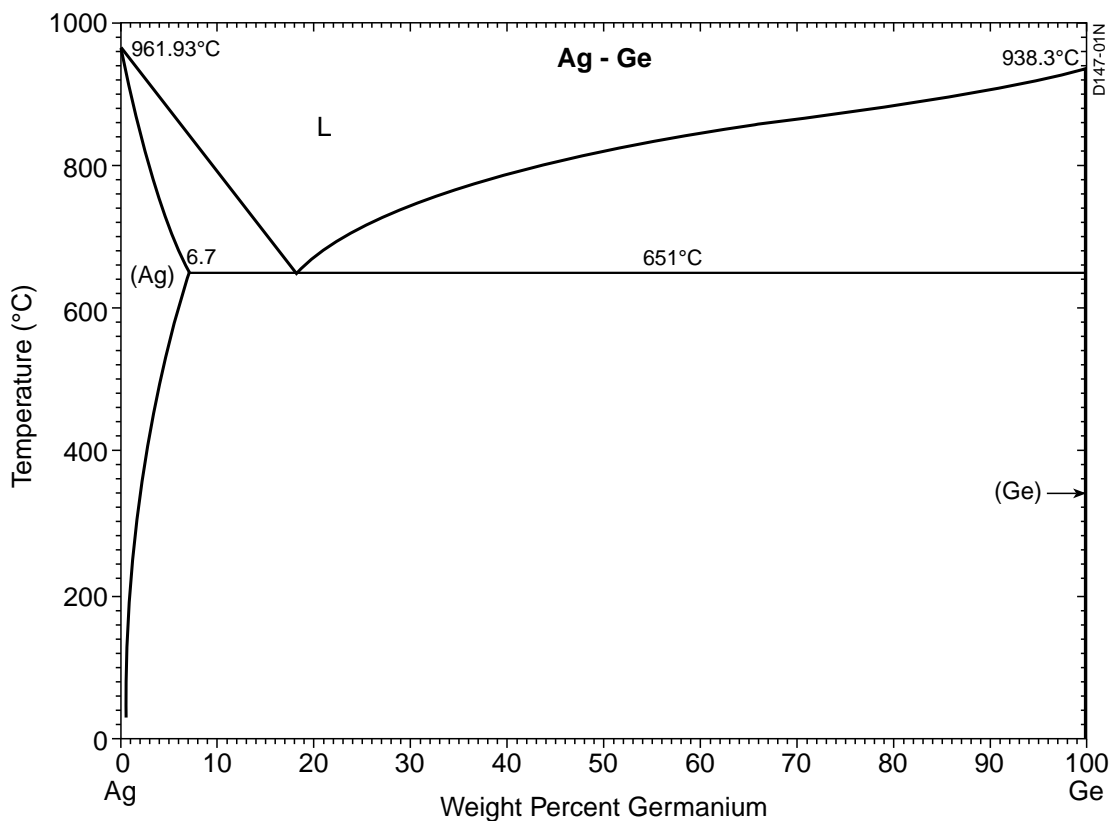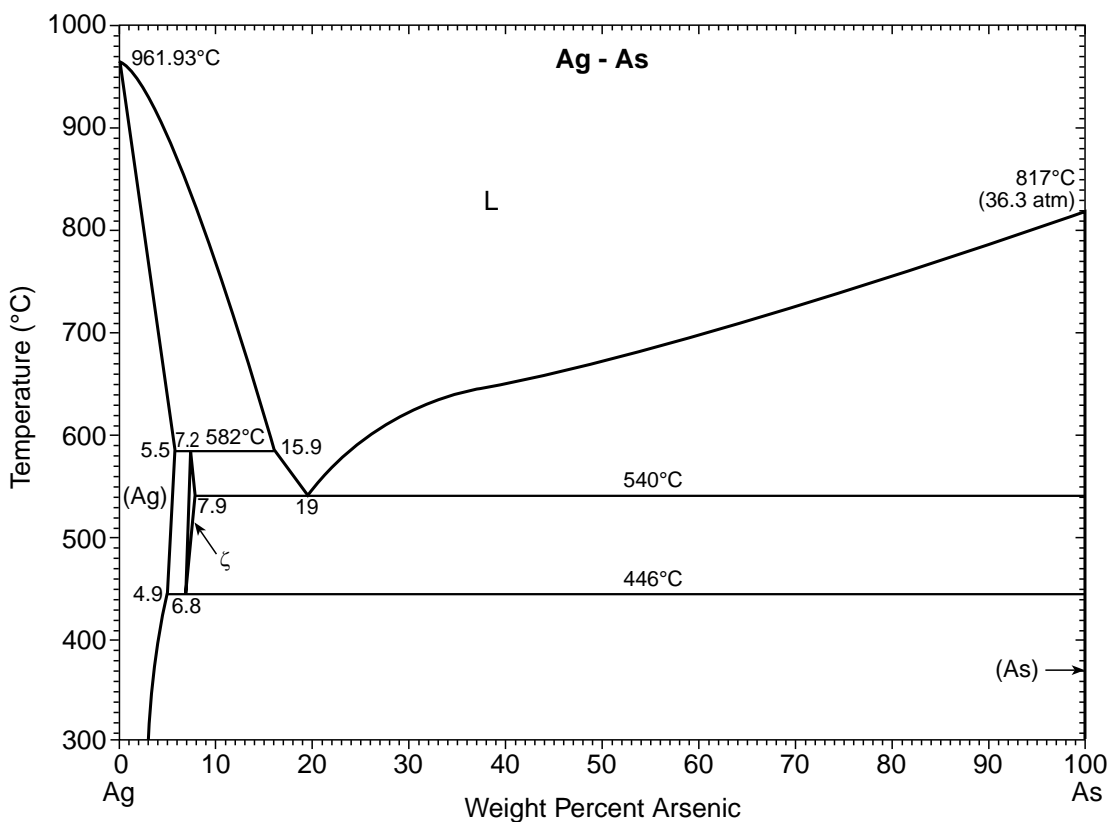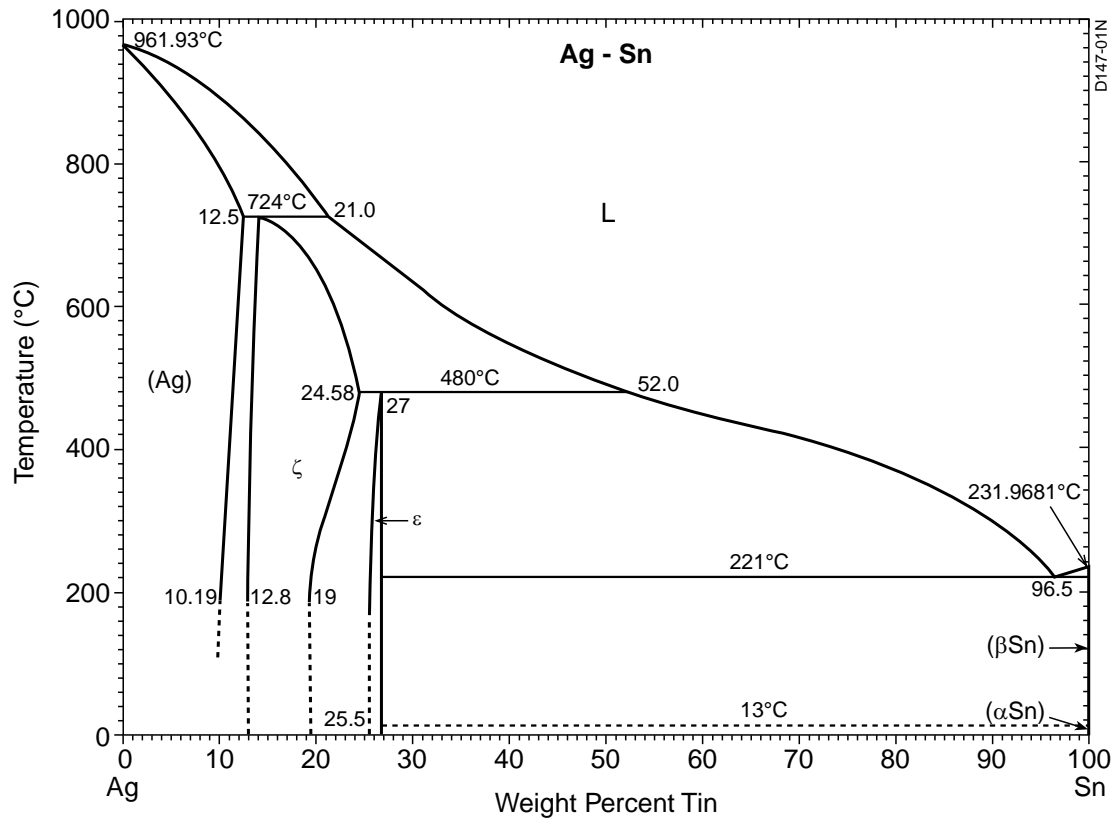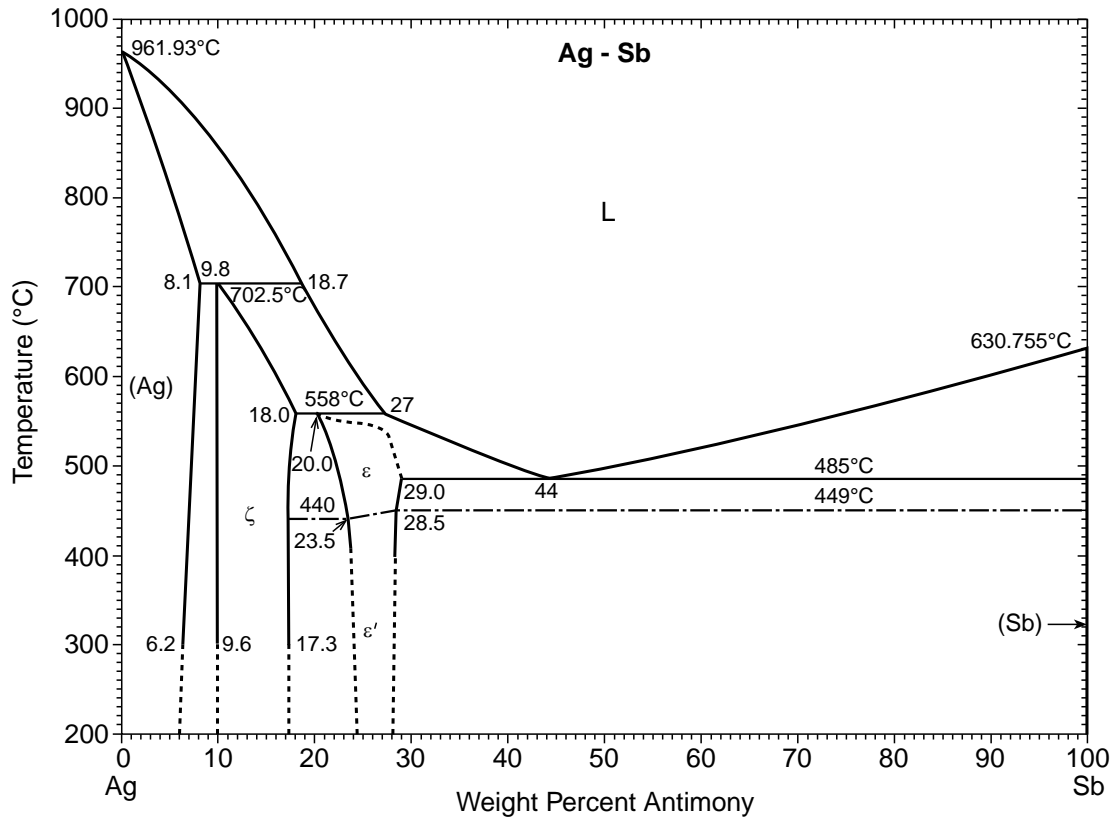
C.3.3 Alloying elements with maximum primary solid solubilities above eutectic temperatures

Ag - Bi

Ag - Pb

Note
See figure 6 of the main report also

D147-01N

D388-01N

Ag - Tl phase diagram

Appendix D   Classification of archaeological silver artifacts and coins in support of figure 18

D.1   Table D.1: artifacts

Table D.1 Classification and weight % of actually and potentially embrittling impurity elements in archaeological silver artifacts

Upper part (Lucas, Gale and Stos‑Gale, Bennett)

85 ≤ Ag wt.% < 95

Pb	Bi	Sb	Sn
0.2			
0.5			
0.2			
0.2	0.19		
1.6	0.18		
0.2			
0.2	0.19		
1.68	<0.01	<0.10	<
1.65	<0.01	0.10	
1.10	<0.01	0.08	
1.15	0.18	0.33	
0.71	0.22	0.21	<0.1
0.90	0.04	0.21	
0.73	0.05	0.22	
0.81	0.07	0.21	
1.18	0.06	0.17	
0.53	0.04	0.15	
1.05	0.08	0.23	
1.04	0.03	0.50	>
0.91	0.07	0.21	

95 ≤ Ag wt.%

Pb	Bi	Sb	Sn		Pb	Bi	Sb	Sn	REFERENCES AND COMMENTS
0.3									Lucas (1928)
0.1	0.19								Gale and Stos-Gale (1981a). One outlier (2.9 wt.% Pb; 1.5 wt.% Bi) excluded
0.5	0.19								
0.2	0.19	<0.10	<		0.42	0.19	<0.10	<	Bennett (1994). All analyses: less than 0.1 wt.% Sn and less than 0.005 wt.% As
0.4	0.15	0.20			0.39	0.15	0.18		
0.5	<0.01	<0.10			0.56	0.15	<0.10		
0.2	<0.01	<0.10			0.50	0.10	<0.10		
0.5	0.06	<0.10			0.43	<0.01	0.11		
0.2	0.05	0.14	<0.1		0.44	0.05	0.35	<0.1	
0.1	<0.01	0.15			0.45	<0.01	<0.10		
0.42	<0.01	0.18			2.70	0.15	0.40		
0.39	0.21	0.10			0.84	<0.01	<0.10		
0.56	<0.01	0.15			0.53	0.04	0.44		
0.50	0.16	0.15			1.17	0.05	0.20		
0.43	0.17	0.13			1.08	0.07	<0.10		
0.44	0.26	0.18			0.46	0.03	0.14	>	
0.45	<0.01	<0.1			0.44	<0.01	0.23		
0.41	0.07	<0.10	>		0.22				
0.22									
0.97									
0.18									
0.16									
0.25									
0.46									

Lower part — Perea and Rovira (1995). One analysis for 85 ≤ Ag wt.% < 95 gave 0.15 wt.% Sb

85 ≤ Ag wt.% < 95

Pb	Sn	Pb	Sn	Pb	Bi	Sb	Sn
0.8	0.385	0.3	0.043	0.6	0.129	2.0	0.073
0.3	0.022	1.0	0.024	1.2	0.013	1.0	0.018
0.4	0.063	0.5		1.7		1.0	0.267
0.7		0.8		0.8	0.19	0.6	
0.6		0.4	0.024	0.7	0.092	1.4	0.018
1.3		0.4	0.052	0.6		0.4	0.006
0.5	0.228	0.2		1.7		1.2	
0.6	0.340	1.9		3.4		0.2	
				2.4			

95 ≤ Ag wt.%

Pb	Sn	Pb	Sn	Sn
0.8	0.003	1.2	0.051	0.014
1.5	0.185	0.7		0.014
0.2	0.012	1.3		0.005
0.4		1.7		0.007
0.3	0.233			0.005
0.4	0.016			0.036
0.5	0.035			
0.3	0.032			

D.2 Table D.2: coins

Table D.2 Classification and weight % of actually and potentially embrittling impurity elements in archaeological silver coins

Caley (1964) — Tylecote (1992) — Cope (1972) — MacDowall (1972) — Gordus (1972) — Metcalf (1972)

85 ≤ Ag wt.% < 95							95 ≤ Ag wt.%						REFERENCES AND COMMENTS
Pb	Bi	Sn	Pb	Sn	Pb	Sn	Pb	Sn	Pb	Sn	Pb	Sn	
0.57	0.0	0.17	0.88	0.08	0.85	0.02	0.46		2.19	0.72	0.06	3.68	Caley (1964)
1.09	0.2	0.02	0.47	0.08	0.63	0.04	0.63		0.85	2.87		0.13	
1.22	0.0	0.04	0.37	0.17	0.39		1.03		0.86	3.05		0.43	
0.39		0.23				0.26							Tylecote (1992)
0.38	0.1		1.05		0.44		0.25						Cope (1972)
0.37	0.1		0.78		1.02								
0.95	0.1		0.34		0.61								
0.5			0.2				0.3		0.2	0.6			MacDowall (1972)
0.6			4.7				0.7		0.7				
1.58		0.05	1.48	0.10	1.10	0.07	0.68		1.10				Gordus (1972)
1.85		0.12	1.63	0.10		0.10	0.42	0.01					
	0.4			0.1			0.8						Metcalf (1972)
	0.9			0.5			0.3						
	1.4			0.7			0.6						
	0.5			0.8			0.1						

McKerrell and Stevenson (1972). One outlier (0.6 wt.% Pb; 8.7 wt.% Bi; 0 wt.% Sn) excluded

85 ≤ Ag wt.% < 95									95 ≤ Ag wt.%									REFERENCES AND COMMENTS
Pb	Bi	Sn	Pb	Bi	Sn	Pb	Bi	Sn	Pb	Bi	Sn	Pb	Bi	Sn	Pb	Bi	Sn	
1.5	0.0	2.9	1.0	0.0	0.5	1.3	0.0	0.5	1.3	0.1	0.8	1.7	0.0	0.0	0.1	0.0	0.0	McKerrell and Stevenson (1972). One outlier (0.6 wt.% Pb; 8.7 wt.% Bi; 0 wt.% Sn) excluded
2.4	0.2	1.7	2.8	0.2	0.0	1.1	0.1	0.2	1.1	0.2	0.9	1.1	0.0		0.7	0.0	0.0	
2.5	0.0	0.2	1.1	0.2	0.5	1.3	0.1	0.6	1.3	0.2	0.0	1.4	0.1	0.4	1.0	0.1		
2.0	0.1	0.0	0.6	0.2	0.5	1.2	0.2	0.2	1.2	0.2	0.3	1.6	0.2	0.2	1.0			
1.1	0.1	0.1	0.8	0.1	0.2	1.4	0.0		1.6	0.1	0.7	1.4	0.3		0.5	1.3	0.0	
1.7	0.1	0.2	1.4	0.2	0.3	1.6	0.2	0.3	1.6	0.0		1.7	0.0		0.6	0.3	0.0	
0.9	0.0	0.1	0.9	0.1		1.3	0.0	0.2	1.2	0.1		1.2	0.3	0.3	0.6	0.4	0.0	
1.4	0.1	0.3	1.6	0.0		0.9	0.0	0.2	1.9	0.0		1.4	0.1		0.9	0.2	0.0	
0.7	0.0	0.3	1.3	0.0	0.2	1.4	0.3	0.5	0.8	0.3	0.3	1.3	0.1		0.6	0.2	0.0	
1.3	0.2	0.5	0.8	0.0		0.7	0.1	0.3	1.4	0.1	0.6	1.3	0.0		0.4	1.0	0.0	
0.9	0.1	0.6	1.3	0.0	0.1	1.2	0.2	0.6	1.3	0.2	0.0	1.9	0.0		0.3	0.7	0.0	
1.2	0.2	0.3	1.2	0.1	1.0	1.0	0.0	0.4	1.4	0.0		1.1	0.0		0.9	0.2	0.0	
0.7	0.0	0.1	1.9	0.0	0.4	1.3	0.3	0.9	1.4	0.0	0.5	0.9	0.2	0.0	0.3	1.3	0.0	
1.0	0.1	0.3	0.9	0.3	0.2	1.3	0.2	0.3	1.8	0.1	0.2	1.2	0.2	0.2	0.2	0.5	0.0	
0.8	0.0	0.0	1.4	0.1	0.3	0.9	0.1		1.4	0.2	0.1	1.0	0.0	0.0				
1.4	0.0	0.3	0.6	0.2	0.6	1.6	0.2		1.4	0.1	0.5	1.0	1.2	0.0				
1.0	0.0	0.0	1.0	0.1	0.2	2.6	0.2	0.3	2.0	0.0		0.9	1.3	0.0				
0.9	0.1	0.3	1.1	0.2	0.4	2.5	0.1		1.3	0.2	0.5	0.7	0.8	0.2				
1.1	0.0				0.5	1.5	0.0		1.4	0.1	0.0							
									1.3	0.0								

Müller and Gentner (1979). Very thorough analyses of Greek coins

85 ≤ Ag wt.% < 95									95 ≤ Ag wt.%									REFERENCES AND COMMENTS
Pb	Bi	Sn	Pb	Bi	Sn	Pb	Bi	Sn	Pb	Bi	Sn	Pb	Bi	Sn	Pb	Bi	Sn	
0.041	0.24	0.006	0.036	0.37	0.002	0.14	0.03	0.005	0.13	0.03	0.001	0.58	0.36	0.002	0.40	0.14	0.007	Müller and Gentner (1979). Very thorough analyses of Greek coins
0.068	0.14	0.004	0.16	0.20	0.014	0.57	0.08	0.003	0.22	0.33	0.002	0.29	0.065	0.004	0.42	0.49	0.003	
0.36	0.083	0.002	0.10	0.074	0.008	1.02	0.10	0.000	0.46	0.30	0.000	0.39	0.11	0.000	0.63	0.14	0.012	
1.27	0.15	0.002	0.46	0.04	0.001	0.26	0.22	0.000	0.066	0.04	0.002	0.22	0.29	0.000	0.44	0.10	0.017	
0.14	0.11	0.000	0.86	0.09	0.003	0.05	0.27	0.002	0.81	0.011	0.067	1.36	0.50	0.000	0.92	0.19	0.002	
0.051	0.14	0.021	0.051	0.18	0.004	0.58	0.31	0.002	1.49	0.12	0.004	0.26	0.20	0.001				

Appendix E   Micromechanical crack models applicable to archaeological silver embrittlement

E.1 Nomenclature and definitions

a	:	half crack length
α	:	lattice parameter (characterizing interatomic distance in a crystal lattice)
b	:	Burgers vector of a dislocation. Its magnitude and direction specify the distance and direction by which atoms on one side of a slip plane have moved with respect to those on the other side, owing to passage of the dislocation
γ_f	:	grain boundary fracture energy, an elusive and much-debated quantity
d	:	grain size (average grain diameter)
δ	:	interplanar spacing between identical planes in a crystal lattice
e	:	the exponential number, approximately 2.718
$\dot{\varepsilon}$	:	strain rate
$F(\theta), G(\theta)$	:	angular functions, see also θ
h	:	perpendicular distance between parallel slip band cracks
k_{II}	:	stress intensity factor of a crack under shear loading parallel to the crack length direction (mode II loading, also called sliding mode)
$k_{II}^*(e)$; $k_{II}(e)$	:	mode II stress intensity factor values required for dislocation emission from the tip of a finite size crack and semi-infinite crack, respectively
$k_{II}(sb)$	:	mode II stress intensity factor for the tip of a slip band
μ	:	shear modulus, an elastic parameter that is constant for isotropic materials
ν	:	Poisson's ratio, an elastic parameter that is constant for isotropic materials
π	:	the well-known transcendental number, approximately 3.142
r_c	:	dislocation core radius, an uncertain quantity
S	:	dislocation source, of which there are several kinds, including cracks, grain boundaries, and dislocations themselves − notably the famous Frank-Read sources (Frank and Read 1950)
σ_f	:	fracture stress (or strength) of a material
σ_y	:	yield stress (or strength) of a material, usually defined as the stress at 0.1 % or 0.2 % offset of the standard stress-strain curve, corresponding to a permanent plastic strain of 0.1 % or 0.2 %
τ_{app}	:	applied shear stress on a slip plane or crack

$\tau_{app}(e)$	:	applied shear stress required for dislocation emission from the tip of a crack
τ_f	:	lattice friction stress (shear stress) opposing dislocation glide along the slip plane; a much debated quantity
τ_i	:	internal shear stress opposing dislocation glide along the slip plane; an indeterminate (variable) quantity
$\tau_{xy}(x)$	:	effective mode II shear stress acting on an edge dislocation gliding along the x-axis
θ	:	angle between a dislocation pile-up and a nucleated crack at the head of the pile-up: see also $F(\theta)$ and $G(\theta)$
x_0 ; x_1	:	distances along the x-axis at which $\tau_{xy}(x) = \tau_f$
$\perp$	:	symbol for an edge dislocation, which is a line discontinuity in the crystal lattice and whose Burgers vector b is perpendicular to the line. The diagram below shows a unit edge dislocation in a simple cubic lattice
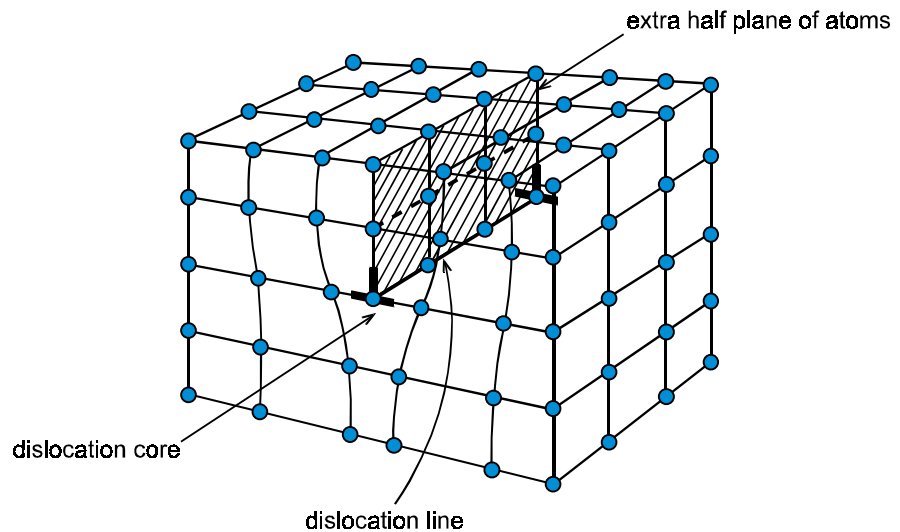
crack stress	:	locally increased stress owing to the presence of a crack
image stress	:	the strain energy of a dislocation decreases when it approaches a free surface, for example a crack tip, because the surface can give way easily to the dislocation's stress field. This means there is a force pulling the dislocation towards the free surface. This force is approximately that expected in an infinite solid between the dislocation and another of opposite sign situated at what would be the position of the dislocation's image on the other side of the free surface. The stress corresponding to this force is called the image stress

slip ; slip planes   :   slip is the sliding of one part of a crystal across a neighbouring part. Slip
and slip directions   is anisotropic, taking place along certain planes and directions in the
                           crystal lattice, the slip planes and slip directions. Slip actually occurs
                           incrementally, by the passage of numerous dislocations along the slip
                           planes

E.2 Introduction

Rigorous analyses of micromechanical crack models require considerable mathematical
expertise and knowledge: see for example the classic papers of Stroh (1954), Bilby *et al.* (1963),
Smith and Barnby (1967) and Rice and Thomson (1974). However, a generic description and
appreciation of the results is less demanding. This is the purpose of this Appendix, which
provides more information on the micromechanical models discussed in the main section of this
report on the effect of grain size on archaeological silver embrittlement.

E.3 The basic assumption of *effectively* infinite crack size

Micromechanical crack models nearly always assume the crack length to be *effectively* infinite,
i.e. the model analyses are independent of crack length. The validity of this assumption was
examined recently by Tanaka and Akiniwa (1999) for cracks under mode II loading, i.e. shear
loading parallel to the crack length direction. Their approach is discussed here.

Consider the situation depicted in figure E.1. Under increasing mode II loading an edge
dislocation (⊥) is emitted from the tip of a sharp crack along the coplanar slip plane (the x-axis).
For a crack of length 2a the effective shear stress $\tau_{xy}(x)$ responsible for the glide force on the
dislocation along the x-axis is given by

$$\tau_{xy}(x) = \underbrace{\frac{\tau_{app}\,(a+x)}{\sqrt{(a+x)^2 - a^2}}}_{crack\ stress} - \underbrace{\frac{\mu b}{2\pi\,(1-\nu)} \bullet \frac{a^2}{[(a+x)^2 - a^2]\,(a+x)}}_{dislocation\ image\ stress} \tag{E1}$$

where τ_{app} is the applied shear stress on the crack; μ is the shear modulus; b is the Burgers
vector of the dislocation; π is the well-known transcendental number, approximately 3.142; and
ν is Poisson's ratio.

From figure E.1 and equation (E1) it is seen that the effective shear stress acting on the
dislocation is the resultant of two opposing stresses, the crack stress and the dislocation image

stress. The crack stress tends to drive the dislocation away from the crack tip, while the image stress attracts the dislocation back to the free surface at the crack tip. Figure E.1 and equation (E1) also show the following three important points:

(1) $\tau_{xy}(x)$ is negative very close to the crack tip, because in this region the absolute (negative) value of the image stress is greater than the crack stress. With increasing distance from the crack tip the value of $\tau_{xy}(x)$ becomes less negative and then positive, reaching a maximum and then decreasing gradually to zero.

(2)   Between x_0 and x_1 the value of $\tau_{xy}(x)$ exceeds the lattice friction stress, τ_f, which always opposes dislocation glide along the slip plane.

(3) $\tau_{xy}(x)$ is increased by a greater crack stress, i.e. the first term in equation (E1). This means that at any distance x from the crack tip the value of $\tau_{xy}(x)$ becomes more positive with increasing applied shear stress, τ_{app}.

These three points provide the conditions under which a dislocation can be emitted from the crack tip. Firstly, a dislocation is attracted back to the crack tip in the region $x \leq x_0$, as is seen from the $\tau_{xy}(x)$ distribution in figure E.1. Thus for dislocation emission to be possible this "barrier" must be overcome. Rice and Thomson (1974) suggested emission is possible when the crack stress, and hence the value of $\tau_{xy}(x)$, becomes high enough that x_0 decreases to the dislocation core radius, r_c.

Secondly, not only must it be possible for a dislocation to be emitted, but it must also be able to move away from the crack tip. This can happen when $\tau_{xy}(x)$ exceeds τ_f, and the dislocation will then glide to the equilibrium position x_1.

In short, the criteria for dislocation emission from the crack tip are $x_0 \leq r_c$ and $\tau_{xy}(x) \geq \tau_f$. These criteria are combined in the following expression:

$$\tau_{xy}(r_c) \geq \tau_f \tag{E2}$$

From equations (E1) and (E2) we can now state the condition for dislocation emission from the crack tip:

$$\tau_f = \frac{\tau_{app}(e)(a+r_c)}{\sqrt{(a+r_c)^2 - a^2}} - \frac{\mu b}{2\pi(1-\nu)} \bullet \frac{a^2}{[(a+r_c)^2 - a^2](a+r_c)} \tag{E3}$$

where $\tau_{app}(e)$ is the applied shear stress required for dislocation emission.

It is now convenient to introduce the *stress intensity factor* (k) concept. The stress intensity factor is a parameter describing the local elastic stresses ahead of a crack in an isotropic and homogeneous material. The stress intensity factor is useful because it incorporates the applied stress *and* crack length. For a mode II loaded crack the general expression for the stress intensity factor is $k_{II} = \tau_{app} \sqrt{\pi a}$.

Specifically, the mode II stress intensity factor corresponding to dislocation emission from the tip of a crack is given by

$$k_{II}^{*}(e) = \tau_{app}(e) \sqrt{\pi a} \tag{E4}$$

where $\tau_{app}(e)$ is obtainable from equation (E3).

Equation (E4) has a twofold significance. First, a dislocation can be emitted from the crack tip when the applied stress intensity factor is larger than $k_{II}^{*}(e)$. Second, this condition combines different applied stresses and crack lengths: long cracks with low applied stresses can have the same stress intensity factors as short cracks with high applied stresses.

Equations (E3) and (E4) enable determining $k_{II}^{*}(e)$ for all crack lengths. However, cracks of effectively infinite length have a constant value of $k_{II}^{*}(e) = k_{II}(e)$. The value of $k_{II}(e)$ is obtained by simplifying equation (E3) using the condition $a \gg r_c$, and substituting this simplification into equation (E4). The result is

$$k_{II}(e) = \left(\tau_f + \frac{\mu b}{4\pi r_c (1-\nu)} \right) \sqrt{2\pi r_c} \tag{E5}$$

The last step in this analysis is to use equations (E3)-(E5) to determine the ratio $k_{II}^{*}(e)/k_{II}(e)$ for different crack lengths: the crack length becomes effectively infinite when this ratio first reaches unity. To calculate $k_{II}^{*}(e)/k_{II}(e)$ we need values for μ, ν, b, r_c and τ_f, together with chosen values of half crack length a (or crack length 2a). The values of μ, ν, b, r_c and τ_f are discussed briefly here, before giving the results of the calculation:

- The shear modulus μ is a constant only for isotropic crystals. Like most metals, silver is anisotropic. For polycrystalline silver $\mu \approx 30$ GPa (Smithells 1967). For the slip planes in silver $\mu \approx 20$ GPa (Hecker *et al.* 1978).

- Poisson's ratio ν for silver has been quoted authoritatively as 0.354 (Rice and Thomson 1974) and 0.367 (Smithells 1967).

- The Burgers vector b for unit dislocations on the slip planes in silver is given by $\alpha/\sqrt{2}$ (Smallman 1963), where the lattice parameter $\alpha = 0.40856$ nm (Barrett 1952, 648). Thus b = 0.289 nm.

- The dislocation core radius r_c is taken to be between 0.3b and 2b (Rice and Thomson 1974; Rice 1992; Tanaka and Akiniwa 1999).

- The lattice friction stress τ_f is a much-debated quantity. A first estimate is obtained from

$$\tau_f = \frac{2\mu}{(1-\nu)} \bullet e^{-\frac{2\pi\delta}{b(1-\nu)}} \qquad \text{(E6)}$$

where δ is the interplanar spacing of the slip planes. For silver the slip planes are of {111} type, i.e. their Miller indices are h=k=l=1. From Barrett (1952, 333, 633, 648) we can derive the value of δ : $\delta = \alpha/\sqrt{h^2 + k^2 + l^2} = 0.40856$ nm$/\sqrt{3} = 0.236$ nm.

Equation (E6) was given by Cottrell (1953, 64), who also discussed its limitations, notably that τ_f estimates are much higher than the yield stresses of the softest single crystals. Substitution of the foregoing values of μ, ν, b and δ in equation (E6) gives τ_f estimates ranging from 19-33 MPa. This range is close to the yield stress of annealed polycrystalline silver (Coxe *et al.* 1979), but more than an order of magnitude higher than the yield stresses of silver single crystals, ranging from about 0.5-1.5 MPa (Andrade and Henderson 1951; Rosi 1954).

It might seem that the possible variations in μ, ν and τ_f values, especially the latter, constitute significant problems for the calculation of $k_{II}^*(e)/k_{II}(e)$. However, it turns out that the $k_{II}^*(e)/k_{II}(e)$ ratios are insensitive to variations in μ and ν and large variations in τ_f. This is demonstrated in figure E.2, which plots $k_{II}^*(e)/k_{II}(e)$ versus different crack lengths expressed as the ratio a/r_c.

The main result from figure E.2 is that $k_{II}^*(e)/k_{II}(e)$ reaches unity at $a/r_c \sim 10^3$, in other words a maximum crack length $2a \sim 1$ μm. This means that mode II loaded cracks more than 1 μm in total length may be considered effectively infinite in size for the purpose of micromechanical crack modelling. It also means that the model analyses can be applied to archaeological silver,

even if fine-grained: a reasonable small grain size range for archaeological silver is d =5-10 μm, which readily enables cracks within grains to exceed 1 μm.

E.4 Micromechanical crack models

Figure E.3 shows the four models of microcrack initiation at grain boundaries in embrittled archaeological silver that are summarised in the main part of this report. These models are discussed in more detail in sub-sections E.4.2 – E.4.4, but first it is convenient to consider the basic interactions of shear mode cracks and dislocations with grain boundaries, in sub-section E.4.1.

E.4.1 Shear mode crack/dislocation/grain boundary interactions, figure E.4

Cracks can form along slip planes in metals. Usually this occurs during the early stages of fatigue failure. However, archaeological silver is a special case, whereby slip bands can be partially or wholly converted into cracks by preferential corrosion (Wanhill *et al.* 1998; Wanhill 2000a, 2001), see also the main part of this report.

In polycrystalline metals slip band cracks are hindered or arrested by grain boundaries. This phenomenon, which has great practical importance, has been analysed using dislocation theory (Taira *et al.* 1978; Tanaka *et al.* 1986) albeit with the simplification that dislocation-free zones at the crack tips and grain boundaries were neglected (Tanaka and Akiniwa 1999).

Consider the two basic situations depicted in figure E.4. These represent slip band cracks under mode II loading that are contained within a grain. Figure E.4a shows a crack whose length 2a is less than the grain diameter d, together with edge dislocations along the coplanar slip plane. The dislocations ahead of each crack tip are of opposite sign ($\perp$ as opposed to   ), corresponding to the opposing directions of the applied shear stress τ_{app}, and are shown *piled up* against the grain boundaries. Figure E.4b shows a crack that has grown right across the grain, i.e. 2a = d.

Analysis of these two basic situations assumes the material to be isotropic and homogeneous and makes use of the fact that the local elastic stresses ahead of a slip band or crack depend in the same way on the distance from the tip of the slip band or crack (Tanaka *et al.* 1986). These assumptions and condition enable use of the stress intensity factor (k) concept to describe these situations. From Tanaka *et al.* (1986) we can derive the following expressions:

| 2a < d (Fig. E.4a) | $k_{II}(sb) = \tau_{app}\ \sqrt{\pi d/2}\left(1 - \dfrac{2\tau_i}{\pi\tau_{app}} \bullet \cos^{-1}\left(\dfrac{a}{d/2}\right)\right)$ | (E7) |

| 2a = d (Fig. E.4b) | $k_{II} = \tau_{app}\ \sqrt{\pi a}\ =\ \tau_{app}\ \sqrt{\pi d/2}$ | (E8) |

where $k_{II}(sb)$ and k_{II} are the respective mode II stress intensity factors for the partially cracked slip band in figure E.4a and the fully cracked slip band in figure E.4b; τ_{app}, π, a and d are as defined earlier; and τ_i is the internal shear stress opposing dislocation glide along the slip plane and away from the crack tips. τ_i is a "catch-all" for various obstacles to dislocation glide, see Cottrell (1953, 103-104, 111-112), and in the present case represents mostly the *back stress* caused by dislocations piling up at the grain boundaries, figure E.4a[G].

The main result from equations (E7) and (E8) is that the stress intensity factors $k_{II}(sb)$ and k_{II} show a direct dependence on the grain size, expressed as the square root of half the grain diameter, $\sqrt{d/2}$. In other words, $k_{II}(sb)$ and k_{II} increase with increasing grain size.

E.4.2 Shear mode dislocation/grain boundary crack interaction, figure E.3a

This is the classic dislocation pile-up model of microcrack initiation. In the present context it is applicable to corrosion-induced and microstructurally-induced embrittlement of archaeological silver whereby corrosion or impurity element segregation have reduced the grain boundary fracture energy, γ_f.

Figure E.3a depicts two situations for an *uncracked* slip band subjected to an applied shear stress:

(1) The left-hand side of figure E.3a represents what generally occurs in polycrystalline metals. Under an applied shear stress, τ_{app}, dislocations are emitted from a source, S. The dislocations glide along the slip plane and pile up against a grain boundary, resulting in a stress concentration at the head of the pile-up. An increase in the applied shear stress causes more dislocations to be emitted and pile up. Eventually the stress concentration at the head of the pile-up becomes high enough to activate a dislocation source, and hence slip, in the neighbouring grain (not shown in figure E.3a). In this way slip can spread from grain to grain in a polycrystalline metal.

[H] τ_i is often taken to be τ_f, the lattice friction stress. This adds unnecessary imprecision to τ_f, which is really only a component of τ_i.

(2)   The right-hand side of figure E.3a shows what can occur when a metal has relatively weak grain boundaries[G], as is possible for archaeological silver (Wanhill *et al.* 1998; Wanhill 2000a, 2001). Under the same applied shear stress, τ_{app}, dislocations are emitted from the source, S, and *at first* pile up against a weak grain boundary. However, with increasing applied shear stress the stress concentration at the head of the pile-up causes microcrack initiation along the grain boundary.

Stroh (1954, 1957) and Smith and Barnby (1967) analysed situation (2) with the trivial difference, *from an analytical viewpoint*, that the microcrack need not initiate along a grain boundary. Similarly, Smith and Barnby combined situations (1) and (2), i.e. they analysed the total configuration depicted in figure E.3a without requiring the microcrack to initiate along a grain boundary. Using this analysis we obtain the following criteria for initiation of a grain boundary microcrack:

complete analysis	$\tau_{app} - \tau_i \geq \sqrt{\dfrac{2\pi\mu\gamma_f}{(1-\nu)\,d}} \bullet \dfrac{1}{\sqrt{F(\theta)}}$	(E9a)
analysis neglecting effect of local stresses due to the dislocation pile-up	$\tau_{app} - \tau_i \geq \sqrt{\dfrac{2\pi\mu\gamma_f}{(1-\nu)\,d}} \bullet \dfrac{1}{\sqrt{G(\theta)}}$	(E9b)

where τ_{app}, τ_i, π, μ and d are as defined earlier; γ_f is the grain boundary fracture energy; and $F(\theta)$ and $G(\theta)$ are angular functions given by

$$F(\theta) = \frac{1}{4}(5 + 2\cos\theta - 3\cos^2\theta) \tag{E10a}$$

$$G(\theta) = \frac{9}{4}(\sin^2\theta \cos^2\frac{\theta}{2}) \tag{E10b}$$

There are two main results obtainable from equations (E9) and (E10). The more important result is that the effective shear stress, τ_{app}-τ_i, required for grain boundary microcrack initiation depends inversely on the grain size, which is expressed as the inverse square root of the grain diameter, $\sqrt{1/d}$, in equations (E9). In other words, microcrack initiation becomes easier with increasing grain size.

[H] The strength of grain boundaries in metals is somewhat controversial, see Cottrell (1989). Be that as it may, archaeological silver can have grain boundaries seriously weakened by corrosion (corrosion-induced embrittlement) and impurity element segregation (microstructurally-induced embrittlement), as discussed in the main part of this report.

The second main result concerns F(θ) and G(θ). Figure E.5 depicts the inverse square roots of these functions, as in equations (E9), for a wide range of θ. From the complete analysis F(θ) shows the criterion for microcrack initiation is nearly independent of the angle between the slip plane and grain boundary for $0 < \theta < 90°$. However, from the analysis neglecting local shear stresses due to the dislocation pile-up the function G(θ) provides only a narrow range of θ favourable to microcrack initiation.

This difference between F(θ) and G(θ) demonstrates the need to account for local shear stresses. Although this might seem obvious, with hindsight, it is emphasized here because Stroh's analyses (Stroh 1954, 1957) did not include local shear stresses, and his results – notably the narrow range of θ favourable to microcrack initiation – are often quoted without further appraisal.

E.4.3 Shear mode crack/dislocation/grain boundary crack interactions, figures E.3b and E.3c

Figures E.3b and E.3c depict two situations derived from those in figures E.3a and E.4, whereby partly or wholly cracked slip bands result in microcrack initiation at relatively weak grain boundaries. As discussed in the main part of this report, for archaeological silver these situations represent either:

(1)   Corrosion-induced embrittlement, with the slip band cracks and grain boundary weakness caused by preferential corrosion.

(2)   Synergistic embrittlement, where the slip band cracks are caused by preferential corrosion and the grain boundary weakness is due to impurity element segregation, i.e. microstructurally-induced embrittlement.

With the knowledge that a slip band crack under mode II loading is equivalent to a pile-up of edge dislocations, except that over the length of a slip band crack the applied shear stress, τ_{app}, is not opposed by an internal shear stress, τ_i, we can substitute equations (E7) and (E8)[G] into equation (E9a) to obtain the following criteria for initiation of a grain boundary microcrack:

[H] As before, see sub-section E.4.1, the material is assumed to be isotropic and homogeneous.

$$2a < d \text{ (Fig. E.3b)} \qquad \tau_{app} \geq \sqrt{\frac{2\pi\mu\gamma_f}{(1-\nu)\,d}} \bullet \frac{1}{\left(1 - \frac{2\tau_i}{\pi\tau_{app}} \bullet \cos^{-1}\left(\frac{a}{d/2}\right)\right)} \bullet \frac{1}{\sqrt{F(\theta)}} \qquad \text{(E11)}$$

$$2a = d \text{ (Fig. E.3c)} \qquad \tau_{app} \geq \sqrt{\frac{2\pi\mu\gamma_f}{(1-\nu)\,d}} \bullet \frac{1}{\sqrt{F(\theta)}} \qquad \text{(E12)}$$

where all the parameters are as defined previously.

The main result from equations (E11)[G] and (E12) is that the applied shear stress, τ_{app}, required for grain boundary microcrack initiation depends inversely on the grain diameter, d, in the first square root expression. This indicates that microcrack initiation becomes easier with increasing grain size.

E.4.4 Multiple shear mode cracks/grain boundary crack interaction, figure E.3d

Figure E.3d depicts a situation similar to that in figure E.3c, but for two or more slip band cracks separated by a distance h. An example is given in figure 19 in the main part of this report. For this situation we modify equation (E8) with an approximation derived from Tada *et al.* (1973):

$$k_{II} = \tau_{app}\sqrt{\pi a}\left(\sqrt{\frac{3h}{2\pi a}} \bullet \left(\frac{2a}{h} + 0.2865\right)\right) \qquad \text{(E13a)}$$

$$= \tau_{app}\sqrt{\pi d/2}\left(\sqrt{\frac{3h}{\pi d}} \bullet \left(\frac{d}{h} + 0.2865\right)\right) \qquad \text{(E13b)}$$

where τ_{app}, π, a and d are as defined earlier. We can then substitute equation (E13b) into equation (E9a) to obtain the following criterion for initiation of a grain boundary microcrack:

[H] Equation (E11) contains a minor complication. On the right-hand side the second (middle) expression is a compensating factor, whereby the applied shear stress, τ_{app}, required for grain boundary microcrack initiation is *increased* by an increase in grain diameter, d. However, this compensating factor reflects only the transition from a total slip band crack, $2a = d$, to a dislocation pile-up of total length d, and a concomitant change in the required shear stress from τ_{app} to τ_{app}-τ_i, compare equations (E9a) and (E11). In both cases there is the basic dependence of the required shear stress on the inverse square root of the grain diameter, $\sqrt{1/d}$.

2a = d multiple slip plane cracks (Fig. E.3d)	$\tau_{app} \geq \sqrt{\dfrac{2\pi\mu\gamma_f}{(1-\nu)\,d}} \bullet \dfrac{1}{\left(\sqrt{\dfrac{3h}{\pi d}} \bullet \left(\dfrac{d}{h} + 0.2865\right)\right)} \bullet \dfrac{1}{\sqrt{F(\theta)}}$ (E14)

The main result from equation (E14) is the same as that from equations (E11) and (E12), namely the applied shear stress, τ_{app}, required for grain boundary microcrack initiation depends inversely on the grain diameter, d, in the first square root expression. This indicates that microcrack initiation becomes easier with increasing grain size.

E.5 Summary

For crack lengths beyond about 1 μm equations (E9)-(E12) and (E14) provide *first approximation* analytical descriptions of shear mode crack/dislocation/grain boundary crack interactions in embrittled archaeological silver, whereby the angular function $F(\theta)$ should be used instead of $G(\theta)$ for equations (E9), (E11), (E12) and (E14).

These analytical descriptions have limitations. They neglect features such as grain boundary ledges, which are powerful concentrators of stress and strain (Li 1961; Das and Marcinkowski 1971), and dislocation-free zones near crack tips and grain boundaries (Ohr 1985; Tanaka *et al*. 1986). Also, they cannot be fully quantified, since the values of internal shear stress, τ_i, and grain boundary fracture energy, γ_f, are variable or unknown.

On the other hand, grain boundary ledges are produced by dislocation pile-ups (Das and Marcinkowski 1971, 1972; Murr 1975); dislocation-free zones near crack tips are highly localised and *generically* neglectable, see Ohr (1985) and Tanaka and Akiniwa (1999); and for the main part of this report it is sufficient to show the general analytical result that microcrack initiation in embrittled archaeological silver becomes easier with increasing grain size.

D388-01N
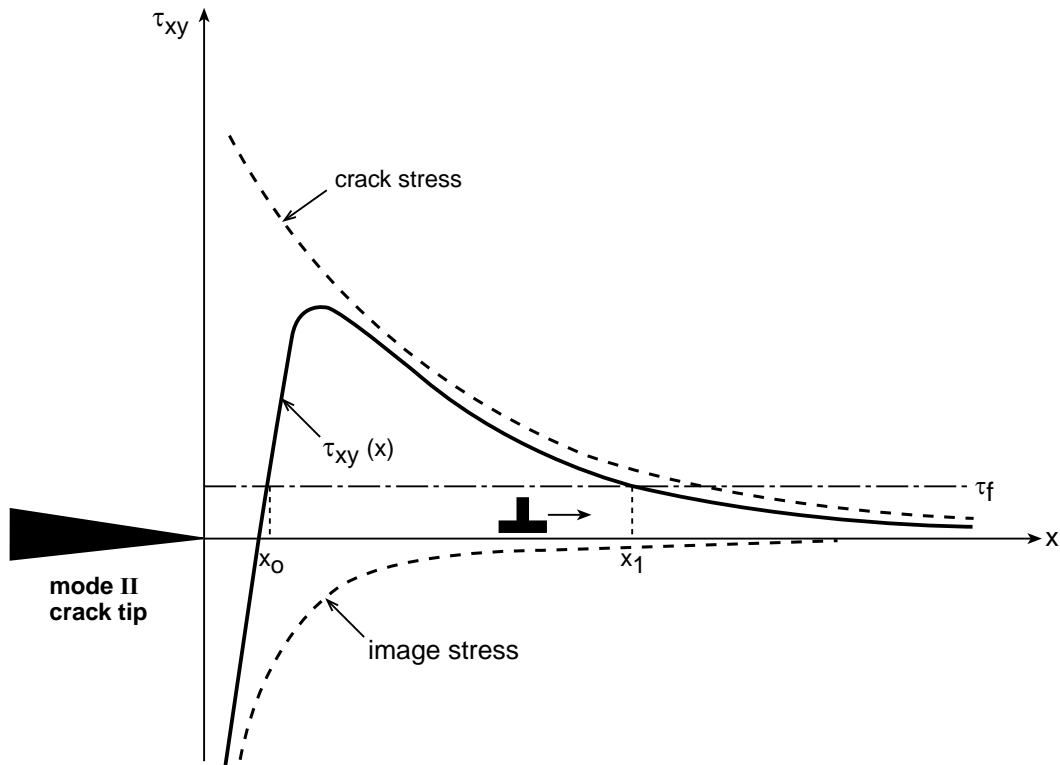
Fig. E.1 Schematic of the stress on an edge dislocation emitted from the tip of a sharp mode II
crack along the coplanar slip plane. The effective shear stress, τ_{xy} (x), is obtained by
adding the shear stress due to the crack and the dislocation image stress. The dislocation
can glide in the x-direction if τ_{xy} (x) is greater than the lattice friction stress, τ_f.
This schematic is a modification of one given by Ohr (1985)
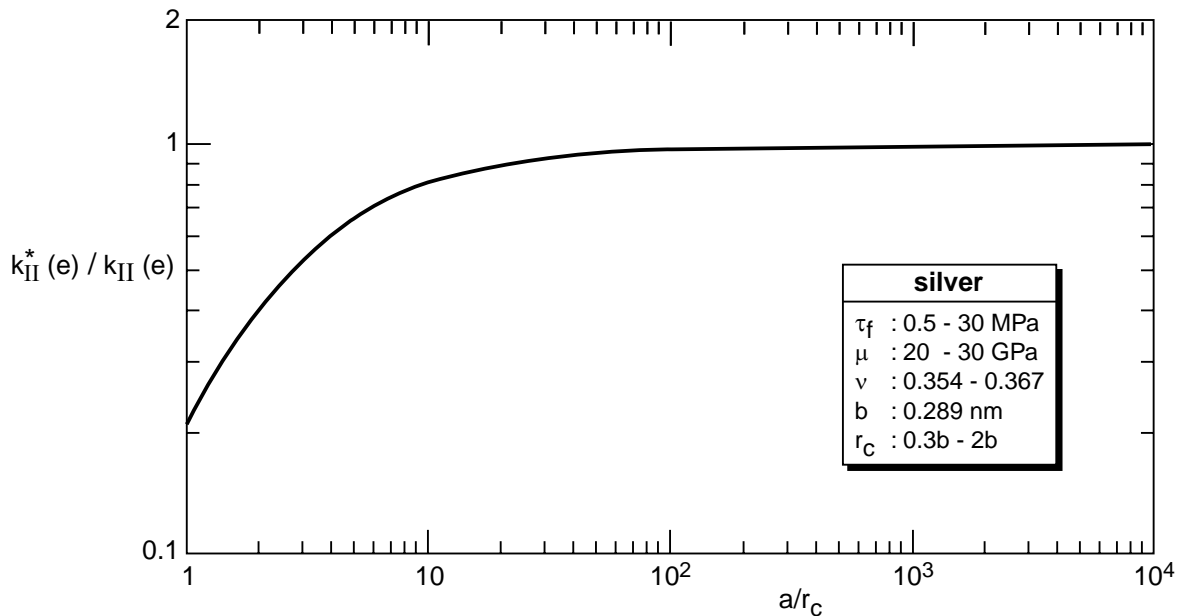
Fig. E.2 Dimensionless plot of the mode II stress intensity factors required for emission of edge
dislocations from the tips of finite length cracks
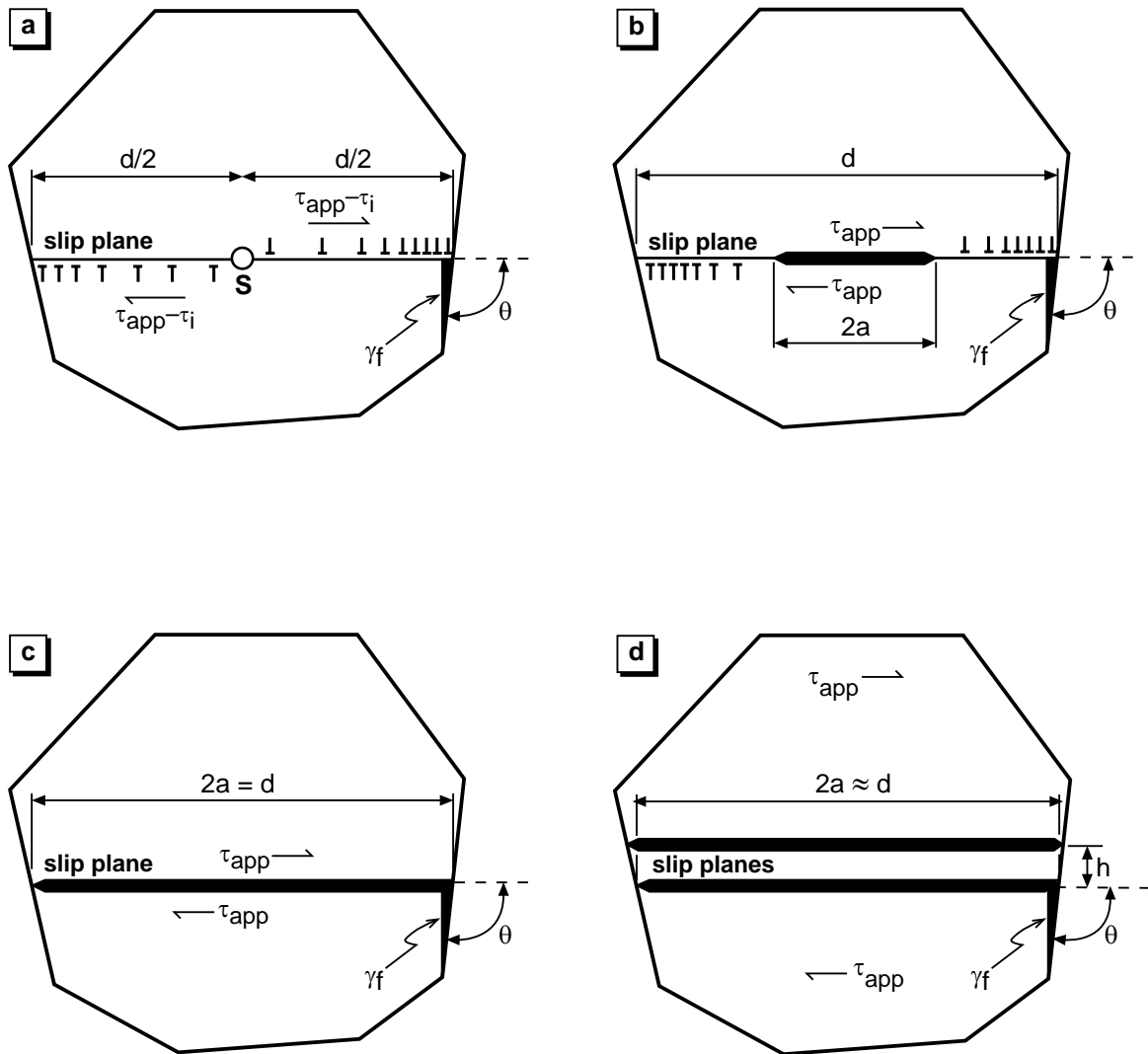
D388-01N

Fig. E.3 Models of microcrack initiation at grain boundaries in embrittled archaeological silver. τ_{app} = applied shear stress; τ_i = lattice friction stress; γ_f = grain boundary fracture energy; 2a = slip plane crack length; d = grain diameter; h = distance between parallel slip plane cracks; S = dislocation source; ⊥,⊤ = edge dislocations of opposite sign

D388-01N

a

b

d

slip plane τ_{app} τ_{app} 2a

2a = d

slip plane τ_{app} τ_{app}
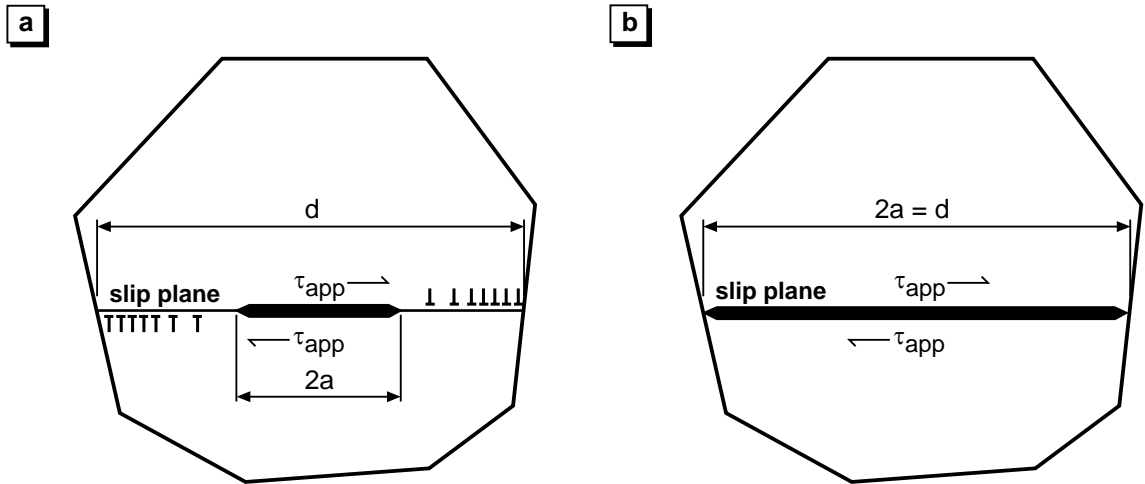
Fig. E.4   Schematics of grains containing slip band cracks under mode II shear loading by an applied shear stress, τ_{app}: (a) crack length 2a less than the grain diameter, d; (b) crack length 2a is equal to the grain diameter, d.

$\dfrac{1}{\sqrt{F(\theta)}}, \dfrac{1}{\sqrt{G(\theta)}}$

$\dfrac{1}{\sqrt{G(\theta)}}$

$\dfrac{1}{\sqrt{F(\theta)}}$

2

1

0   90   180

θ (degrees)
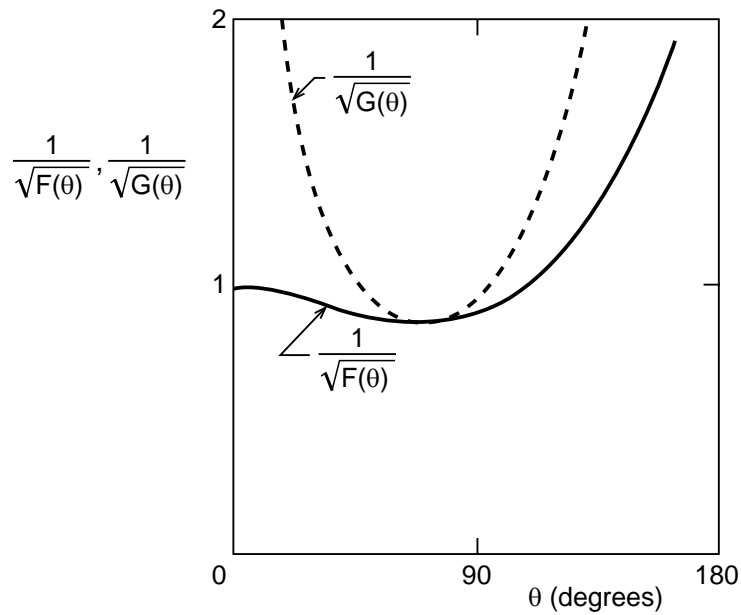
Fig. E.5   Inverse square roots of the angular functions F(θ) and G(θ) derived by Smith and Barnby (1967). F(θ) is for a complete analysis of microcrack initiation ahead of an edge dislocation pile-up, see figure E.3a. G(θ) is for the same analysis but neglecting local shear stresses due to the pile-up